Electronic and Optical Properties of InAs Nanocrystals

Theerapong Puangmali

BSc (Hons), MSc (Distinction)

School of Electronic and Electrical Engineering

Faculty of Engineering

The University of Leeds

Submitted in accordance with the requirements for the degree of Doctor of Philosophy.

The candidate confirms that the work submitted is his own and that appropriate credit has been given where reference has been made to the work of others.

December 2010

"Gravitation cannot be held responsible for people falling in love."

Albert Einstein
Physicist (1879 - 1955)

Abstract

An atomistic pseudopotential method is used to investigate the electronic and optical properties of spherical InAs nanocrystals. Our calculated interband (valence-to-conduction) absorption spectra reproduce the features observed experimentally both qualitatively and quantitatively. The results relative to intraband (valence-to-valence and conduction-to-conduction) absorption successfully reproduce the recently measured photoinduced absorption spectra, which had so far been addressed only qualitatively. They exclude the hypothesis of a thermal activation process between dot-interior delocalised hole states to explain the temperature dependence observed experimentally. Furthermore, based on the agreement of our data with the experimental valence intersublevel transitions and the almost complete overlap of the latter with STM measurements, we question the simplistic attribution of the observed STM peaks obtained for negative bias.

Motivated by the excellent agreement of our calculated results with the STM, PLE and PIA spectra, we therefore extend our knowledge to a detailed theoretical investigation of the electronic structure and optical properties of InAs nanocrystals at the transition from spheres to rods. We predict that despite the qualitative similarity of both intra- and inter-band optical spectra, for NCs with $R > 15$ Å even slight elongations should result in shifts of the order of hundreds of meV in the spacings between STM peaks measured

in the positive bias regime, in the position of the intra-band absorption peaks associated with transitions in the conduction band and in the separation between the first and the fifth peak in PLE experiments. Our results suggest that, based on the spectroscopic data, it should be possible to discriminate between spherical and elongated NCs with aspect ratios of length over diameter as small as 1.2. Indeed our results suggest that many nominally spherical experimental samples contained a large fraction of slightly elongated structures.

Additionally, the atomistic pseudopotential approach is also applied to a study of the electronic and optical properties of InAs quantum rods as a function of increasing length-to-diameter ratio. We show that, as the aspect ratio increases, energy levels cross in both conduction and valence bands, reflecting their different dependence on confinement along a specific direction. Unlike in CdSe and InP quantum rods, however, the position of the crossover between highest occupied molecular orbitals with different symmetries is found to be size-dependent and the value of the aspect ratio at the crossing to increase with the rod diameter. We find that the level crossings at the top of the valence band are crucial to explain the evolution with elongation of all optical properties in these systems. Their transformation from 0- to quasi-1-dimensional structures is characterised by a common monotonic behaviour of band gap, Stokes shift, degree of linear polarisation and radiative lifetime, closely linked to the variation with aspect ratio of the electronic structure of the nanocrystal valence band edge. This characteristic feature was not observed in elongated CdSe structures, whose optical properties exhibited instead a distinctive non-monotonic evolution with length, with a turning point associated with a crossover at the top of the valence band, similar to that found here between states with σ and π symmetries.

Acknowledgements

I would like to express my gratitude to many people who have encouraged and assisted me throughout the course of this work. Firstly, I thank my supervisors Marco Califano and Paul Harrison for introducing me to this fascinating field of research and for their strong support through many hours of enlightening meetings and discussions. Thanks are due also to the Royal Thai Government for funding my studies.

We are grateful to Alex Zunger for insightful discussions and for granting us permission to use the NanoPSE (Nanoscience Problem Solving Environment for atomistic electronic structure of semiconductor nanostructures) computational package developed at the National Renewable Energy Lab. (Golden, CO, U.S.) for all the calculations performed in this thesis. We would like to thank Peter Graf for kindly providing the code used for the NC passivation and for his precious help and advice in the passivation procedure.

I am indebted to the staffs and students of the Institute of Microwaves and Photonics. In particular, to Pirot Moontragoon for his advice during my initial PhD study, to my collaborators Alex Valavanis, Leon Lever and Craig Evans for their valuable contributions to the initial support of my study and to Margaret Quirke and Louise Redmonds for countless hours of administrative support. I also thank my colleagues past and present for many useful discussions.

No word could express the depth of love that I had for my little girl, Nattaporn Kamonthip, and her fantastic family. Your great support and sincere encouragement are always well-kept in a corner of my memories.

These acknowledgements would be incomplete without mentioning my friends and family. I'm forever grateful to you for coping with me through my monologues. Your support has been the keystone of my work.

Theerapong Puangmali, December 2010

Contents

List of Figures

List of Tables

List of abbreviations

CB	Conduction Band
CBM	Conduction Band Maxima
CI	Configuration Interaction
CISL	Conduction Inter-sublevel
DCM	Direct Carrier Multiplication
DOS	Density of States
EPM	Empirical Pseudopotential Method
FLE	Fluorescence Line Narrowing
FSM	Folded Spectrum Method
HRTEM	High Resolution Transmission Electron Microscope
ISL	Inter-sublevel
LDA	Local Density Approximation
LEDs	Light Emitting Diodes
MBE	Molecular Beam Epitaxy
MOVPE	Metalorganic Vapour Phase Epitaxy
NC	Nanocrystal
PIA	Photoinduced Absorption
PL	Photoluminescence
PLE	Photoluminescence Excitation

QD	Quantum Dot
QR	Quantum Rod
QWR	Quantum Wire
SEPM	Semiempirical Pseudopotential Method
SLDA	Spherically Local Density Approximation
SP	Single Particle
STM	Scanning Tunnelling Microscopic
TB	Tight-binding
TEM	Transmission Electron Microscopy
VB	Valence Band
VBM	Valence Band Maxima
VISL	Valence Inter-sublevel

List of principal symbols

Fundamental constants

$c = 3.00{\times}10^{8}\,\mathrm{m/s}$	Speed of light in vacuum
$e = 1.60{\times}10^{-19}\,\mathrm{C}$	Elementary charge
$\varepsilon_0 = 8.85{\times}10^{-12}\,\mathrm{F/m}$	Vacuum permittivity
$\hbar = 1.05{\times}10^{-34}\,\mathrm{J\,s}$	Reduced Planck constant
$k_B = 1.38{\times}10^{-23}\,\mathrm{J/K}$	Boltzmann constant
$m_e = 9.11{\times}10^{-31}\,\mathrm{kg}$	Rest mass of free electron

Symbols

a	Lattice constant
a_0	Exciton Bohr radius
a_1	Anion with one dangling bond
a_2	Anion with two dangling bonds
$\mathring{A}$	Angstrom
b	The width of Gaussian potential
B_1, B_2, B_3	The first three strongest bright excitons in the tight-binding method
c_1	Cation with one dangling bond
c_2	Cation with two dangling bonds

d_0	Ideal length of bulk In-As bond
D	Diameter
e_i	Electron states (i increases from 1 starting from CBM upward)
E_{fast}	Fast, high-energy, allowed state
E_g	Energy gap
$E_{\mathrm{gap}}^{\mathrm{bulk}}$	Energy gap of bulk semiconductor
$\{E_n\}$	Eigenvalue
E_{nonres}	Non-resonance Stokes shift
E_{res}	Resonance Stokes shift
E_{slow}	Slow, redshifted, forbidden state
E_1, E_3, E_5	The first, third, fifth strong peak from the absorption spectra
h_i	Hole states (i increases from 1 starting from VBM downward)
(h_i,e_m)	a specific exciton derived mainly from the single-particle levels h_i and e_m
$\hat{H}$	Hamiltonian
$I_{\parallel}$	The intensity of light polarised parallel to the long axis
$I_{\perp}$	The intensity of light polarised perpendicular to the long axis
J	Coulomb integral
K	Exchange integral
l_{cut}	Cutoff length
L	Length
M	Dipole matrix elements
M_ν	Mass of nuclei
n	the refractive index of the medium surrounding the nanocrystal
n_0	The electron density
N	The total number of atoms in the system
N_c, N_v	The number of valence and conduction states included in the expansion of the exciton wave functions
N_{dot}	The total number of cations and anions in a quantum dot
q	Thomas-Fermi wavevector

r_{cut}	Cutoff radius
$\mathrm{r}_{\alpha,j}$	The basis vector for atom j in unit cell n
$\mathbf{r}_\mu$	Position of electron
R	Effective radius of nanocrystals
$S(\mathbf{G})$	Structure factor
$\hat{T}$	Kinetic Energy
v	Ligand potential
$v_\alpha(\mathbf{r})$	Atomically screened potentials
$V(G)$	Reciprocal space functional form of the pseudopotential
$V(\mathbf{r})$	The total screened pseudopotential of the crystal
$\hat{V}_{nl}$	Non-local pseudopotentials or a negative part of pseudopotentials
$V_{\text{ps}}^{\text{SEPM}}(\mathbf{r})$	Microscopic pseudopotential of the system (dot plus surrounding material)
w	Amplitude of the Gaussian potential
Z_μ	Atomic number
$1\mathrm{S}_e$, $1\mathrm{P}_e$	The two lowest states in the conduction band
1_{VB}, 2_{VB}	The two highest states in the valence band
$\|1h\rangle$, $\|2h\rangle$, $\|3h\rangle$	The ground, first and second excited hole states, respectively
α	Amplitude of the Gaussian potential
β	Degree of linear polarisation
$\|\chi_n\rangle$	Core wave function
ϵ_{ref}	An arbitrary reference energy in the folded spectrum method
ϵ_{c}	Energy levels in conduction band
ϵ_{v}	Energy levels in valence band
ϵ^{-1}	The inverse dielectric function
$\epsilon^{-1}(k)$	Fourier transform of the inverse dielectric function
$\epsilon_{\text{el}}^{-1}$	An electric (high-frequency) contribution of dielectric constant
$\epsilon_{\text{ion}}^{-1}$	An ionic (low-frequency) contribution of dielectric constant
ϵ_0^{dot}	The low frequency dielectric constant of the dot
ϵ_∞	The high frequency dielectric constant of the dot

η	The distance along the ideal bond (in atomic unit)
Γ	The experimental line broadening
ω_{LO}	The bulk LO-phonon frequency
$\|\phi\rangle$	A node-free pseudo-wave function
$\Phi_{\mathrm{v,c}}$	A set of single-substitution Slater determinant
$\|\psi\rangle$	Wave function
ψ_{v}	The occupied valence states
ψ_{c}	The unoccupied conduction states
ρ_∞	The solution of $\sinh(q\rho_\infty)/(q\rho_\infty) = \epsilon_\infty^{\mathrm{dot}}$
ρ	Aspect ratio of a nanorod
ρ_{c}	The aspect ratio of a nanorod that the energy level crossing occurs
τ	The thermally averaged lifetime
$\uparrow, \downarrow$	Spin variables (up and down)
ξ	The quality of a passivation (the quality factor)

List of Publications

The following journal[1] and conference[2] papers were published by the author during the course of the present work.

Journal papers

1. **Puangmali, T**, Califano, M, Harrison, P, "Interband and intraband optical transitions in InAs nanocrystal quantum dots: A pseudopotential approach", *Physical Review B (Condensed Matter and Materials Physics)*, **78**, 2008. (3.475)

2. **Puangmali, T**, Califano, M, Harrison, P, "The effect of small elongations on the electronic and optical signatures in InAs nanocrystal quantum dots", *Journal of Physics: Condensed Matter*, **21**, 2009. (1.964)

3. **Puangmali, T**, Califano, M, Harrison, P, "Monotonic evolution of the optical properties in the transition from three- to quasi-two-dimensional quantum confinement in InAs nanorods", *Journal of Physical Chemistry C*, **21**, 2010. (4.224)

Conference publications

1. ⊛**Puangmali, T**, Califano, M, Harrison, P, "Interband and intraband optical transitions in InAs nanocrystal quantum dots: A pseudopotential approach", *One*

[1]The number in the parentheses presents the ISI impact factor of the journal in 2009.
[2]Poster and oral presentations are, respectively, marked with ⊛ and ★.

Day Quantum Dot Meeting, Department of Physics, Imperial College London, UK, 11 January 2007. (**Poster**)

2. ⊛**Puangmali, T**, Califano, M, Harrison, P, "The effect of small elongations on the electronic and optical signatures in InAs nanocrystal quantum dots", *Workshop : Theory, Modelling and Computational Methods for Semiconductor Material and Nanostructures*, University of Manchester, UK, 31 January-1 February 2008. (**Poster**)

3. ⊛**Puangmali, T**, Califano, M, Harrison, P, "The theoretical investigation of the electronic structure and optical properties of InAs nanocrystals at the transition from spheres to rods.", *UK Semiconductor Physics*, Department of Electronic and Electrical Engineering, University of Sheffield, UK, 2-3 July 2008. (**Poster**)

4. ⊛**Puangmali, T**, Califano, M, Harrison, P, "A pseudopotential study of discrimination between spherical and slightly elongated NCs in InAs experimental samples", *One Day Quantum Dot Meeting*, Department of Physics and Astronomy, University of Sheffield, UK, 13 January 2009. (**Poster**)

5. ★**Puangmali, T**, Califano, M, Harrison, P, "Monotonic evolution of the optical properties in the transition from three- to quasi-two-dimensional quantum confinement in InAs nanorods", *The* 2^{nd} *Workshop on Theory, Modelling and Computational Methods for Semiconductor Material and Nanostructures*, St William's College, York, UK, 13-15 January 2010. (**Oral**)

6. ⊛**Puangmali, T**, Califano, M, Harrison, P, "Influence of elongations on the electronic and optical properties in InAs semiconductor nanostructures", *The* 6^{th} *International Conference on Quantum Dots*, East Midlands Conference Centre, Nottingham, UK, 26-30 April 2010. (**Poster**)

7. ★**Puangmali, T**, Califano, M, Harrison, P, "Electronic structure transformation from a quantum dot to a nanorod system : a pseudopotential approach", *UK Semiconductors 2010*, The Endcliffe village, University of Sheffield, UK, 7-8 July 2010. (**Oral**)

8. ★**Puangmali, T**, Califano, M, Harrison, P, "Pseudopotential study of electronic and optical properties of InAs semiconductor nanostructures : Quantum dots and Nanorods", *The* 10^{th} *International Conference on Numerical Simulation of Optoelectronic Devices*, Georgia Institute of Technology, Atlanta, Georgia, United States, 6-9 September 2010. (**Oral**)

To my adorable family

Chapter 1

Introduction

1.1 Semiconductor quantum dots

In the last decades, it has already been shown that the reduction in dimensionality produced by confining electrons (or holes) to a thin semiconductor layer (quantum wells) leads to a dramatic change in their behaviour. This principle can be developed by further reducing the dimensionality of the electron's environment from a two-dimensional quantum well to a one-dimensional quantum wire and eventually to a zero-dimensional quantum dot. In quantum dots, the electron is confined in all three-dimensions, thus reducing the degrees of freedom to zero. With the remarkable progress in nanotechnology, this structure has been made in the nanometer scale where the laws of quantum mechanics rule and a range of new physical effect are manifested. On the one hand, fundamental laws of quantum mechanics can be tested. On the other hand, a large volume of possible applications are rapidly emerging.

QDs have been produced in several different ways in a broad range of semiconductor material systems. Their properties and possible applications are largely dependent on the method they have been obtained, which can therefore be used as a criterion for classification of different types of quantum dots, as illustrated in Fig. 1.1:

- **Electrostatic quantum dots**

  The electrostatic quantum dots can be produced by restricting the two dimensional electron gas in a semiconductor heterostructure laterally by electrostatic gates, or vertically by etching techniques. The confining potential of electrons is generated by the electrostatic field and their properties can be controlled by changing the applied potential at gates, the choice of the geometry of gates or by external magnetic field. They have been suggested as implementations of qubits for quantum information processing.

- **Self-assembled quantum dots**

  They nucleate spontaneously under certain conditions during molecular beam epitaxy (MBE) and metalorganic vapour phase epitaxy (MOVPE). Due to the mismatch of the lattice constant of different materials during the growth process, the resulting strain produces strained islands on top of a two-dimensional wetting-layer. The islands can be subsequently buried to form the quantum dot. This growth mode is known as Stranski-Krastanov growth. On the one hand, there are several limitations of this method including the cost of fabrication and the lack of control over positioning of individual dots. On the other hand, this fabrication method has potential for applications in quantum cryptography and quantum computation.

- **Colloidal nanocrystals**

  Like traditional chemical processes, colloidal semiconductor nanocrystals are synthesised from precursor compounds dissolved in solutions. The synthesis of colloidal quantum dots is based on a three-component system composed of: precursors, organic surfactants, and solvents. When heating a reaction medium to a sufficiently high temperature, the precursors chemically transform into monomers. Once the monomers reach a high enough supersaturation level, the nanocrystal

growth starts with a nucleation process. Their size and shape can be controlled by the duration, temperature and ligand molecules used in the synthesis. These quantum dots can contain as few as 100 to 100,000 atoms. Due to their scalability and the low-cost fabrication, colloidal quantum dots are promising for a large volume of commercial applications.

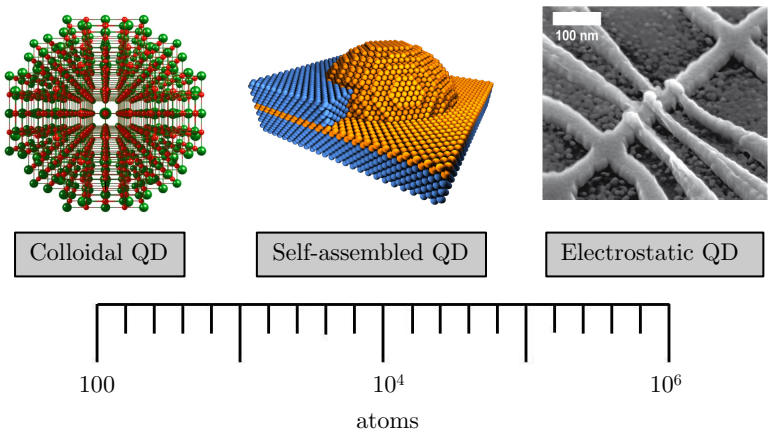

FIGURE 1.1: Different types of quantum dots. Colloidal nanocrystals are solution-grown, nanometre-sized, inorganic particles that are stabilised by a layer of surfactants attached to their surface. Self-assembled quantum dots are typically between 5 and 50 nm in size. They nucleate spontaneously when a material is grown on a substrate to which it is not lattice matched. The resulting strain produces coherently strained islands on top of a two-dimensional wetting-layer. Electrostatic quantum dots can be fabricated by restricting the two dimensional electron gas in a semiconductor heterostructure laterally by electrostatic gates, or vertically by etching techniques.

1.2 Colloidal semiconductor nanocrystals

Among the variations in the fabrication processes [10], colloidal semiconductor NCs, sometimes referred to as "*artificial atoms*", represent a very promising system as their popularity deriving from their size tunable optical properties that enable their applications in very different fields [11] such as optoelectronics, as well as biology (as organic molecule markers), and also from the possibility of achieving a very high degree of size monodispersity (less than 5%) in their synthesis [12–14]. Additionally, due to their

chemical flexibility, they can easily be ordered in 3D superlattices, linked to form quantum dot molecules, prepared as closed-packed films or incorporated with high densities into sol gel, glass or polymers.

Nowadays, intense efforts are made in growing colloidal NCs with engineered shapes, for instance, nearly spherical dots [12, 13], elongated nanorods [14], tetrapods [15], semiconductor heteroparticles [16–19]. This is due to the fact that the combination of shape- and size-dependent physical properties and ease of fabrication and processing makes colloidal NCs promising building blocks for materials with designed functions [10]. To implement these shape-selected nanocrystals for the future applications, it is crucial to obtain the exact knowledge of wave functions of excitons, the excitonic fine structure, the radiative lifetime, the density of states as well as interactions with other elementary excitations. In the following section, we will give an overview about physics of semiconductor NCs so as to make the contents of the thesis as self-contained as possible. The inclusion of a simple view of the physics and the associated terminologies is given below so that when the specific calculations or applications are discussed, the basic ideas will be in context.

1.3 Brief review of physics of semiconductor NCs

1.3.1 Quantum size effect

As the size of solids decreases many physical phenomena become more pronounced [20]. One of the key phenomena is quantum mechanical effects, where the electronic and optical properties of solids are altered with great reductions in particle size. Such a quantum effect does not come into play by substantial reduction from macro to micro dimensions. Quantum effects, however, become prominent once the dimensions of solids

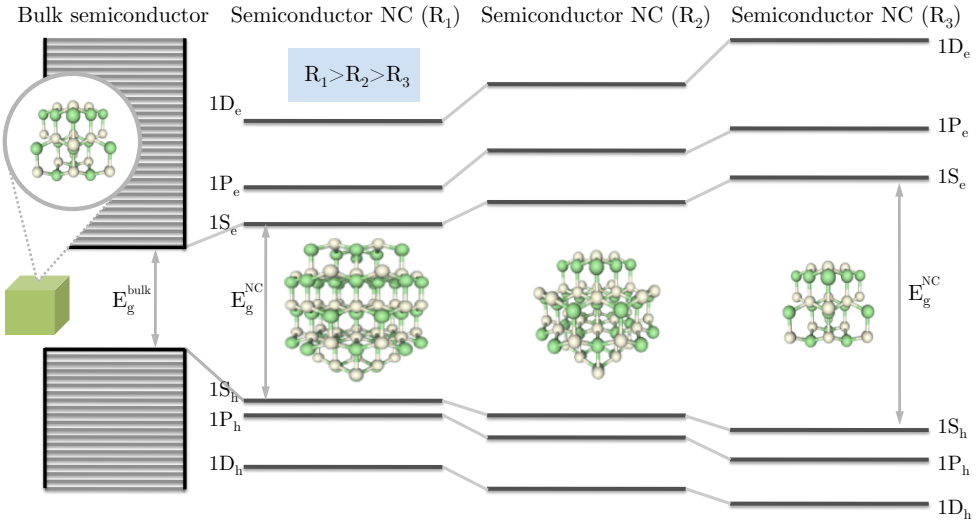

FIGURE 1.2: A schematic illustrating *quantum size effect*. In a bulk semiconductor, both conduction and valence energy bands are continuous and they are separated by a fixed energy gap, E_g, while discrete atomic-like states are found in low-dimensional confinement NCs and the energy gap is size-dependent (increase with decreasing dimensions).

reach nanometre scale. It is typically at distances of 100 nanometers or less. Generally, in bulk semiconductors a natural length scale of electronic excitations is considered by the Bohr exciton radius, a_x, defined by the strength of the electron-hole $(e-h)$ Coulomb interaction. In semiconductor NCs whose sizes are comparable to or smaller than the Bohr exciton radius (a_x) the spatial extent of the $e-h$ pair state is defined by the dimensions of the nanoparticle, i.e., the size of the NC exciton. As a result, electronic energies are directly dependent on degree of spatial confinement of NC sizes. This is known as "*quantum size effect*" [20–25]. As a result of this effect, one can continuously tune the NC energy gap (E_g) by more than 1 eV [4, 9] with a reduction of NC sizes, as illustrated in Fig. 1.2.

1.3.2 Quantisation and energy level spacing

As the dimensions in NCs are reduced, another pronounced feature is the development of discrete, well-separate energy states [26–28], replacing the continuous energy bands of a bulk material, as schematically shown in Fig. 1.2. Both conduction and valence band give rise to an independent series of quantised states in the absence of band mixing effect. To illustrate, in spherically quantum dots, we can classify these states in accordance to the angular momentum (l) of the envelope wave functions, describing carrier motion in the low-dimensional confinement potential [29]. Typically, the three lowest energy states in semiconductor nanostructures are labelled as 1S, 1P, and 1D, according to the hierarchy of states in the series of states of the same symmetry and the angular momentum (S for $l = 0$, P for $l = 1$, and D for $l = 2$). The lowest state in either conduction or valence bands, however, is not necessary to be 1S. It has been recently reported that there are level crossings at the top of the valence band due to the change of aspect ratio in InAs elongated structures [30, 31] and the valence band maximum is found to be $p - like$ symmetry. These energy level crossings are very crucial to explain the optical properties in these semiconductor nanostructures.

1.3.3 Coulomb and exchange interaction

A consequential effect of the confinement of carriers in very small length scales is a strong enhancement of Coulomb interactions [32, 33]. The Coulomb interaction energy between two electrons confined in a semiconductor nanocrystal can be smaller than the quantisation energy, meaning that a quantum mechanical description of the Coulomb effects is important. Two characteristic Coulomb energies are the biexciton binding energy (ϵ_{xx}), which provides a measure of the strength of exciton-exciton interaction, and the exciton binding energy (ϵ_x), which is a measure of $e - h$ interaction strength.

It is found in bulk materials that these energies are inversely proportional to the natural exciton and biexciton radii [22]. In II-VI semiconductors the exciton and biexciton binding energies are on the order of tens of meVs and a few meVs, respectively. For instance, in bulk CdSe, ϵ_x=16meV [34], while ϵ_{xx}=4.5meV [35]. In semiconductor nanocrystals, Coulomb interaction energies rapidly increase with decreasing NC dimensions. For spherical quantum dot the Coulomb energies scale approximately as R^{-1} where R is the NC radius [36, 37]. Additionally, due to the reduced dielectric screening the interaction energies are greatly enhanced with decreasing NC sizes. As a result of these factors, the Coulomb interaction energy in semiconductor nanostructures can be enhanced as large as 100 meV while the biexciton binding energy can be up to more than tens of meV [38–40].

In addition to the confinement-enhanced Coulomb interaction, the physics of excitons in NCs is also governed by the *electron-hole exchange interaction*. This effect leads to a size-dependent splitting between the absorbing and emitting states [41, 42]. As the exchange interaction is proportional to the electron-hole charge density overlap this splitting is predicted to scale inversely with the radius of NCs. In InP and CdSe quantum dots, the electron-hole exchange interaction is proportional to R^{-2} [43]. The same scaling law is also predicted in InAs semiconductor NCs [6].

1.3.4 Direct carrier multiplication

Carrier multiplication (also called direct carrier multiplication : DCM) was first observed in bulk semiconductors in the 1950s. It is the direct photogeneration of multiexcitons by single photons [44–49]. The mechanism of carrier multiplication is schematically illustrated in Fig. 1.3. It is an Auger-like process whereby a high-energy carrier with excess energy $\Delta \geq E_g$ relaxes to its band edge by energy transfer to a valence electron

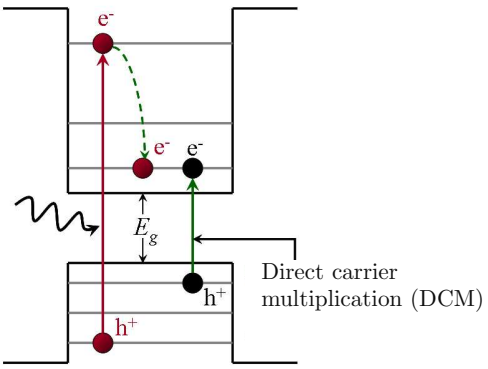

FIGURE 1.3: A schematic of direct carrier multiplication (DCM) in neutral quantum dot that could lead to enhanced solar photon conversion efficiency in quantum dot photovoltaic cells. It involves the generation of multiple electron-hole pairs from the absorption of a single photon.

which is excited across the gap. If the first carrier is generated by the absorption of a photon with energy $\Delta \geq 2E_g$, the result of this process is the creation of two electron-hole pairs (excitons) from a single absorbed photon. In fact, it is plausible to create more than two electron-hole pair. It has been recently found that a single absorbed photon can create as many as seven excitons in PbSe semiconductor nanocrystals [47, 48].

Compared with the DCM in bulk semiconductors, the rate of exciton multiplication in semiconductor nanocrystals is greatly enhanced. This is due to carrier confinement and the increased electron-hole Coulomb interaction. In addition, crystal momentum needs not be conserved because momentum is not a good quantum number for three-dimensionally-confined carriers [41, 50]. With the highly multiexciton generation, the NCs are expected to provide increased power conversion efficiency in the form of increased solar cell photocurrent, which is subsequently discussed in the following section.

1.4 Applications of semiconductor NCs

The size-controlled tunability of NC optical properties combined with chemical flexibility provided by colloidal methods make colloidal NCs promising materials for a wide variety of applications [11] in various optical technologies and electronic devices. To build a picture of their practical realisation, in the following we will give a practical point of view of semiconductor colloidal nanocrystals as active optical materials in photonic structures and electronic devices.

1.4.1 Photovoltaic cells

Colloidal NCs are promising candidate for high efficiency photovoltaic cells. Recently, A. Nozik [51] was the first to propose that in semiconductor NCs, direct carrier multiplication (DCM) effects could be greatly enhanced [46] compared to bulk materials. More specifically, due to the large confinement, the Coulomb interaction between electron and hole is stronger in NCs compared to bulk materials and has indeed been proved to enhance DCM. Furthermore, as in quantum dots there is no momentum conservation, i.e., the wave vector momentum is not a good quantum number in 0-D system. As a result, the DCM threshold energy, the minimum excess energy an electron must have to initiate DCM, E_{th} is equal to E_g. In bulk solids, instead, due to both energy and momentum conservation constraints, $E_{th} = E_g + \delta E$ where δE varies from $\sim$0.1eV for InAs, $\sim$0.2eV or $\sim$0.3eV for GaAs, to $\sim$1eV for InP.

Recently, semiempirical pseudopotential method [52, 53] was applied to investigate the energy dependence of DCM rates and of the rates of selected competing process in neutral and negatively charged CdSe NCs. For excess energy just a few meV above the energy gap E_g (the DCM threshold), it was found that DCM is much more efficient in

quantum dots than in bulk materials, with rates of the order of $10^{10}s^{-1}$. In conventional bulk solids, comparable rates are obtained only for excess energies about 1eV above E_g. The only problem with the use of CdSe NCs in photovoltaic devices is their wide band gap, that makes them not ideal for use invisible part of the solar spectrum. Better suited candidates for that energy range would be materials with smaller band gap such as InAs, InP or PbSe. Bulk PbSe has a narrow direct band gap of 0.28eV at room temperature and size quantisation effects are strongly pronounced in PbSe NCs. Recent experimental studies showed band-edge excitonic transitions with energies between 0.5 and 1.1eV, suggesting that PbSe NCs can also be used for optoelectronic devices in the IR spectral regime and in telecommunication applications.

Indeed high DCM efficiency was recently found experimentally in spherical PbSe NCs [47, 48] by Klimov's group in Los Alamos, USA. For photovoltaic cells based on PbSe NC of a single size they estimate a 10% increase in conversion efficiency compared to the maximum theoretical conversion limit. In PbSe [46], electron and holes have very similar effective masses; therefore, the energy of the incident photon is equally divided between the photogenrated carriers. It follows that the onset of DCM is at a photon energy three times the NC band gap E_g, as the carriers need to have an excess energy of at least E_g to initiate DCM, and an energy of at least E_g is needed to generate and electron-hole pair in the ground state. However, in NCs made of materials that have substantially different carrier effective masses and where therefore the photon energy would be distribute less "democratically" between them. This threshold could be minimise to $2E_g$. Schaller and Klimov speculated the possibility to achieve a further 27% [46] increase in relative power conversion efficiency (that would bring its absolute value to 60.3%) via this minimisation of the (photon) DCM threshold.

1.4.2 Quantum dot lasers

Semiconductor lasers [54–57] have become prevalent and widely used in many fields ranging from medical diagnosis, information storage and processing to telecommunications. The use of semiconductor NCs in quantum dot lasers has a number of advantages over the conventional quantum well lasers. The lasing threshold is, in principle, dramatically reduced due to the enhancement in the density of states in the structure where the quantum confinement is in three dimensions. Additionally, the well-separated atomic-like states in the semiconductor NCs are size-dependent; therefore, for NCs in the strong confinement regime the electronic states are much greater than the available thermal energy. This leads to a reduction of thermal population of the lowest electronic states, resulting a lasing threshold that is temperature-insensitive. Besides, an emission wavelength of very small semiconductor NCs is a pronounced function of size leading to the advantage of wavelength tunability over a wide energy range simply by changing the size of the NCs. Consequently, the output colours of the lasers can be easily controlled by manipulation of NC size.

1.4.3 Light-emitting diodes

Colloidal nanocrystal is a promising candidate and uniquely suited for light-emitting devices due to their tunable luminescence properties. Compared with epitaxially grown quantum dots, colloidal can be synthesised as highly monodisperse colloids and solution deposited over large areas into densely packed, solid-state multilayers, which have shown promise as efficient optical gain media. It has been recently demonstrated [58] that colloidal NCs can be integrated to bright, monochrome LEDs with uniform pixel emission of saturated colour and high peak luminance. The nanocrystal-based LEDs show the brightness that is comparable with the best-organic-based LEDs. Besides, they also

improve the environmental stability of metal-oxide charge transport layers [58]. The stable operation under a high carrier-injection rate enable evolution of the QD-LEDs to device designs that will be needed to demonstrate electrically pumped colloidal QD lasers. Such devices would be able to take full advantages of the tunability and the ease of fabrication and processing of colloidal QDs to provide simple, tunable, coherent light sources.

1.4.4 Fluorescent biological imaging probes

Colloidal NCs also have the high potential to become a new class of fluorescent probes for biological and biomedical applications [59–69], especially cellular imaging [60, 61, 67, 68]. Semiconductor NCs, as fluorescent probe, have a number of advantages over conventional organic dyes. They exhibit excellent photostability leading to continuous illumination of the samples. In addition, due to quantum size effect, their emission spectra are narrow and symmetrical. This allows closer spacing of different probes without the substantial spectral overlap. Besides NCs can display broad absorption spectra; consequently, using NCs as fluorescence probe is capable of exciting all colours of NCs simultaneously with an appropriate single excitation light source.

Nonetheless, the feasibility of using NCs as fluorescence probes in biological preparations has been questioned. NCs should not be toxic or interfere with cellular function provided that they are used in vivo. It is also vital to establish ways for using NCs to specifically interact with the target biomolecule and to reduce nonspecific binding. Furthermore, the fluorescent signal is quenched if the semiconductor NCs are not perfectly coated leading to inappropriate coats for NCs.

Recently, Wu *et al.* [1] have shown that they are able to use nanoparticles to label surface, cytoskeletal and nuclear proteins in fixed cells and tissue sections. Labelling was

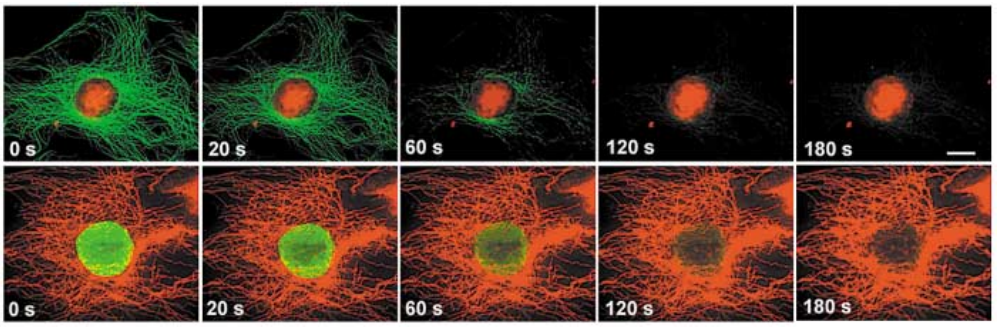

FIGURE 1.4: The top row shows microtubules and nuclear antigens labelled with the conventional fluorescent dye Alexa 488 (bright green) and QDs (red), respectively. The bottom row illustrates the reverse combination (red for QDs and green for the fluorescent dye Alexa 488). To illustrate the stability of QD labelling, continuous illumination for three minutes caused QDs remained stable whereas the Alexa signal fades completely. (digitally copied from [1])

highly specific, and was brighter and more stable than using other fluorescent markers. Moreover, they can simultaneously use two NCs of different emission spectra and manage to detect two different targets with a single excitation wavelength. A concrete example of the use of NCs in biological imaging is illustrated in Fig.1.4, showing the more stability of QD labelling.

1.4.5 Quantum information processing

Quantum information is physical information in quantum mechanics that is held in the "state" of a quantum system. Entanglement together with quantum coherence have played as physical bases for quantum information processing. This scheme uses quantum bits or qubits (two-states quantum system) to provide secure communication and more efficient computation [70]. Currently, its extension to solid-state systems remains a demanding experimental goal even though quantum control of entanglement has been realised in isolated atomic systems. Quantum information processing based on solid-state system can provide the stronger coupling of solid-state qubits to their environment. In addition, it also leads to the prospect of scalable fabrication. Therefore, learning how

to control quantum systems in the strong-coupling system is a key challenge of quantum information processing.

Semiconductor quantum dot is one of the most attractive candidates for a solid-state qubit. By using switchable voltages that are applied to electrostatic gates, they allow controlled coupling of one or more electrons. Recently it has been found that spin in semiconductor quantum dots is probably a promising holder of quantum information [70] due to the long spin relaxation in the order of tens of milliseconds. Additionally, the two-electron spin qubit in semiconductor NC also provides the implementation of quantum computation schemes with a number of practical advantages. The local electrostatic gate control can lead to all operations for protecting, measuring and preparing entangled electron spins. Considerable techniques has been developed, leading to fascinating prospects for practical realisations of a wide variety of ideas from quantum information science in low-dimensional structures.

Aside from aforementioned applications, there are wide varieties of practical realisations [11] of semiconductor NCs in photonic and electric devices, including spintronic [71–82], quantum emitter antennas [83] as well as thermopower devices [84]. Despite the extensive investigations conducted over the past decades, the theoretical investigation at determining the ideal characteristic of a NC for such applications, especially in quantum-dot based photovoltaic cells, has not been fully exploited. The goal of this thesis is to provide an accurate description of the electronic and optical properties in InAs colloidal NCs of selected shapes so as to be a driving force for the state-of-the-art applications discussed in this section. The outline of the thesis is provided in the following section.

1.5 Thesis outline

In Chapter 2 the theoretical framework used in this thesis will be presented. An atomistic pseudopotential method is used to investigate electronic and optical properties of InAs semiconductor nanostructures. In Chapter 3, starting from a simple system of spherical quantum dot, our calculated interband absorption spectra reproduce the features observed experimentally both qualitatively and quantitatively. The results relative to intraband valence-to- valence and conduction-to-conduction absorption successfully reproduce the recently measured photoinduced absorption spectra, which had so far been addressed only qualitatively. They exclude the hypothesis of a thermal activation process between dot-interior-delocalized hole states to explain the temperature dependence observed experimentally. Furthermore, our study shows the excellent agreement of our data with the experimental valence intersublevel transitions and the almost complete overlap of the latter with scanning tunneling microscopic STM measurements. In Chapter 4, we move to a study of slightly elongated dots to provide an unambiguity on both the size and shape of the NCs in the experimental samples. We predict that despite the qualitative similarity of both intra- and inter- band optical spectra, for NCs with R$\geq$15 Å even slight elongations should result in shifts of the order of hundreds of meV in the spacings between STM peaks measured in the positive bias regime. Our results suggest that many nominally spherical experimental samples contained a large fraction of slightly elongated structures. In Chapter 5, we study a more complicated structure, nanorod. We show that, as the aspect ratio increases, energy levels cross in both conduction and valence bands, reflecting their different dependence on confinement along a specific direction. Unlike in CdSe and InP quantum rods, however, the position of the crossover between highest occupied molecular orbitals with different symmetries is found to be size-dependent and the value of the aspect ratio at the crossing to increase

with the rod diameter. We find that the level crossings at the top of the valence band are crucial to explain the evolution with elongation of all optical properties in these systems. Their transformation from zero- to quasi-one-dimensional structures is characterised by a common monotonic behaviour of band gap, Stokes shift, degree of linear polarisation, and radiative lifetime, closely linked to the variation with aspect ratio of the electronic structure of the nanocrystal valence band edge. Finally, a summary of the work presented, along with the conclusion and suggestions for possible future direction of the research in this exciting area are given in Chapter 6.

Chapter 2

Theoretical Framework

The theoretical framework used in the thesis will be presented in this Chapter. Our present calculation for the electronic and optical properties in nanocrystal structures is based on the atomistic pseudopotential method. Initially the discussion will start with an overview of this approach. Then the construction of semiconductor nanocrystals with different shapes and sizes will be presented. The following section will focus on the details of surface passivation followed by a section of pseudopotentials and their construction. A method used to solve the single-particle problem will subsequently be explained, along with the way to take into account the many-body effects. Last but not least, we will describe the calculation of the optical properties and their importance including the absorption and emission spectrum, Stokes shift, degree of linear polarisation and the radiative lifetime.

2.1 Approximate methods

Currently, optical properties of nanostructures containing a few hundreds of atoms can be calculated from atomistic first principles such as time-dependent density functional theory, quantum Monte Carlo, etc. Extensions of these methodologies to the many-body

problem, however, are unlikely to be able to address the aforementioned size regime. To obtain many insights of strong confinement system, first-principles *ab initio* methods have been steadily developed.

The **k**·**p** model [85–87] has become one of the most widely used bandstructure models for describing not only 3-dimensional semiconductors, but also lower dimensional systems such as quantum wells, wires, and dots. This method gives a more accurate description of the electronic structure near the top of the valence band and the bottom of the conduction band without having to resort to numerical methods. Basically, in the **k**·**p** method one can start with the known form of the bandstructure problem at the bandedges and the perturbation theory is used to describe the bands away from the high symmetry points. Since for the central cell functions, we only expand around the high symmetry points in terms of known functions, the problem is considerably simplified, often leading to analytical results.

To explain in more details of the **k**·**p** method, the Bloach's theorem [85, 87] has been recalled. The wave function in a periodic material can be written as the product $\psi_{n\mathbf{k}}(\mathbf{R}) = u_{n\mathbf{k}}(\mathbf{R})e^{i\mathbf{k}\cdot\mathbf{R}}$, where $u_{n\mathbf{k}}(\mathbf{R})$ is a periodic function, $\mathbf{k}$ is called the wave vector and n is a discrete index. It is a good approximation to assume that $u_{n\mathbf{k}}$ is constant over a small region of $\mathbf{k}$-space. The description of electrons in a crystal has to be via Schrödinger equation

$$\left(\frac{\hat{\mathbf{p}}^2}{2m_0} + V_{\text{per}}(\mathbf{R})\right)\psi_{n\mathbf{k}}(\mathbf{R}) = \varepsilon_n(\mathbf{k})\psi_{n\mathbf{k}}(\mathbf{R}) \tag{2.1}$$

where m_0 is the mass of free electrons and $\hat{\mathbf{p}} = -i\hbar\nabla$ is the momentum operator. After substituting $\psi_{n\mathbf{k}}(\mathbf{R}) = u_{n\mathbf{k}}(\mathbf{R})e^{i\mathbf{k}\cdot\mathbf{R}}$ into Eq. 2.1, the derivatives of $\hat{\mathbf{p}}$ acting on the plane wave simply give $\hbar\mathbf{k}$ and the wave then cancel out. This leaves an equation for

the periodic part $u_{n\mathbf{k}}(\mathbf{R})$ alone :

$$\left\{ \left(\frac{\hat{\mathbf{p}}^2}{2m_0} + V_{\text{per}}(\mathbf{R}) \right) + \left(\frac{\hbar}{m_0}\mathbf{k}\cdot\hat{\mathbf{p}} + \frac{\hbar^2\mathbf{k}^2}{2m_0} \right) \right\} u_{n\mathbf{k}}(\mathbf{R}) = \varepsilon_n(\mathbf{k}) u_{n\mathbf{k}}(\mathbf{R}). \tag{2.2}$$

Having solved Eq. 2.2 at $\mathbf{k} = 0$, one knows the set of wave functions $u_{n\mathbf{0}}(\mathbf{R})$ and the energy $\varepsilon_n(\mathbf{0})$. Quantum theory tells us that these form a complete set of functions. These functions can therefore be used as a basis explaining the solution of some other values of $\mathbf{k}$. Alternatively, we can use perturbation theory, as we are mainly concerned with small values of $|\mathbf{k}|$. The terms that depend on $\mathbf{k}$ in Eq. 2.2 are therefore viewed as a perturbation away from from the solution at $\mathbf{k} = 0$. In Eq. 2.2 one is simply the change in energy of a free electron, while the other contains the operator $\mathbf{k}\cdot\mathbf{p}$, which gives the name of the method. It has been found that the $\mathbf{k}\cdot\mathbf{p}$ method is simpler and considerably more accurate if one is interested only in phenomena near the bandedges. It is also capable of handling macroscopic system; nonetheless, this approach fails to deal with nanostructures [88, 89], where atomistic effect become more and more important.

Another widely used theoretical method is the tight binding method (TBM) [5, 85–87, 90]. It is an empirical technique in which experimental inputs are used to fit the bandstructure. TBM uses atomic functions as a basis set for the Bloch functions. The periodic part of the Bloch function is represented by some combination of the atomic orbitals centred at the lattice points. If $\phi_n(\mathbf{r} - \mathbf{R})$ represents such an orbital centred at $\mathbf{R}$, we could write a Bloch function of the form:

$$\psi_{\mathbf{k}}(\mathbf{r}) = \sum_{\mathbf{R}_n} \phi_n(\mathbf{r} - \mathbf{R}) e^{i\mathbf{k}\cdot\mathbf{R}} \tag{2.3}$$

In Eq. 2.3 the periodic part of the Bloch function is expanded in terms of the atomic-like orbitals of the atoms of the unit cell (index n in the summation). The elements making up all the semiconductors of interest have the valence electrons described by

s- or *p*-type atomic orbitals. The core electrons are usually not of interest. As the atoms of the elements making up the semiconductors are brought together to form the crystal, the electronic states are perturbed by the presence of neighbouring atoms and discrete states broaden to form bands. While the original atomic functions describing the valence electrons are, of course, no longer eigenstates of the problem, they can be used as a good approximate set of basis states to describe the crystalline electrons. This is the motivation for the tight binding method.

In semiconductors there are two atoms per basis and for each atom we need to include at least the outer shell s, p_x, p_y, p_z functions. It is possible to improve the technique by adding additional atomic levels. Since there are two atoms per basis in a semiconductor, we require eight functions to describe the central cell part of the Bloch functions. We choose a state of the form

$$\Psi_{\mathbf{k},\mathbf{r}}(\mathbf{r}) = \sum_{\mathbf{R}_i} \sum_{m=1}^{4} \sum_{j=1}^{2} C_{mj}(\mathbf{k}) \phi_{mj}(\mathbf{r} - \mathbf{r}_j - \mathbf{R}_i) e^{i\mathbf{k}\cdot\mathbf{R}_i} \tag{2.4}$$

where the sum $\mathbf{R}_i$ is over unit cells, m are the different atomic functions ϕ_{mj} being used in the basis, and j are the atoms in each unit cell.

In zinc blende crystals the sp^3 basis is used and there will be eight basis functions, i.e., an s and three p orbitals, p_x, p_y and p_z for each of the two atoms within the Wigner-Seitz cell. This approximation assumes that there is spin degeneracy in the bandstructure of the crystal. If the effects of the breaking of spin degeneracy are being considered, one would need a basis which includes the spin-up and spin-down variants of each orbital. This results in a requirement of a sixteen function basis for zinc blende semiconductors. Then the Schrödinger equation is solved in the form of a secular determinant [86]. It has been found that empirical tight binding models can currently address millions of atoms;

however, they lack detailed information about atomistic feature of the wave functions [88, 89], which constitute the essence of the many-body problem.

With the recent development of the *semiempirical pseudopotential method* (SEPM) [43, 88], a detailed description of the carrier wave functions on the atomic scale can be addressed and this approach can also be used in conjunction with configuration interaction to obtain excitations in semiconductor nanostructures. The brief details of this method will be discussed in the following section.

2.2 Overview of atomistic pseudopotential method

The semiempirical pseudopotential calculation of semiconductor nanostructures is composed of a series of different steps as illustrated in Fig. 2.1. There are three main

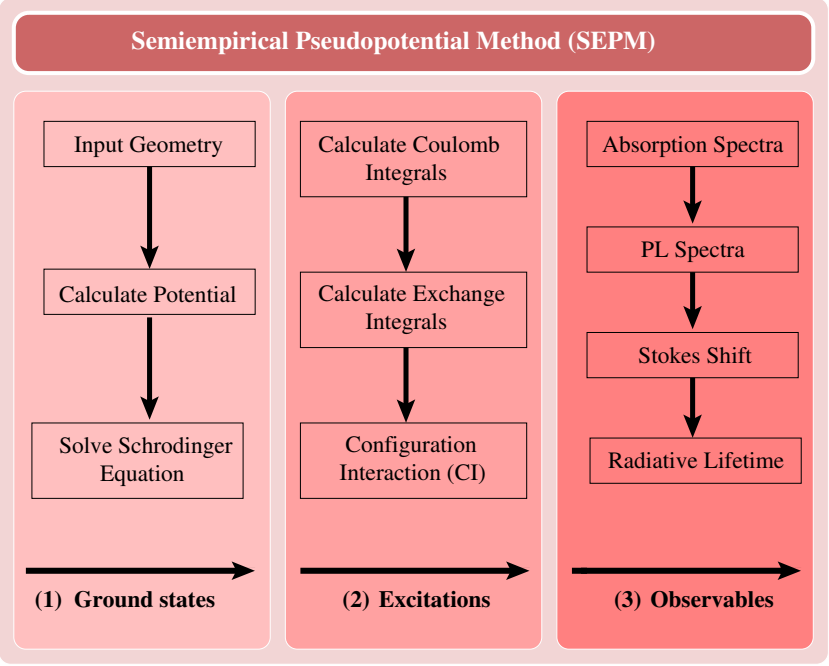

FIGURE 2.1: Flowchart of the semiempirical pseudopotential method (SEPM) used to calculate the electronic structure of nanostructures and their optical properties, i.e., absorption and emission spectra, radiative lifetime and Stokes shift.

steps in our calculation of the optical properties of semiconductor nanocrystals: (i) the solution of the single-particle Schrödinger equation; (ii) the calculation of many-body effects; (iii) the calculations of the optical properties. First, the input geometries are determined from geometrical considerations and experimental data. The potential of the system is then calculated using a superposition of screened atomic potentials which are fitted to the experimental band structure and local density approximation (LDA) wave functions. After pseudopotentials are constructed, a basis set for the single-particle Schrödinger equation is defined and solved using the folded spectrum method (FSM). Based on this approach we are able to calculate eigenstates near the bandedges (CBM or VBM). After we obtain the single-particle energies and wave functions we then calculate the electronic excitations of the quantum dots. To accomplish this task we first calculate the Coulomb and exchange integrals and follow with the configuration interaction (CI) method. Finally we calculate optical properties of the system, for example, the absorption and emission spectra. In what follows, we will describe in more details behind each step of the atomistic pseudopotential approach.

2.3 Construction of semiconductor nanocrystals

The first step in the calculation of the optical properties of semiconductor nanocrystals is the construction of the atomistic structure of the NC. Here, we consider As-centred InAs spherical (quantum dots, QDs) and elongated (quantum rods, QRs) NCs with the zinc-blende structure (lattice constant a=6.0584 Å), constructed by adding successive atomic layers up to a specific cutoff radius r_{cut} (and cutoff length l_{cut} along the z (001) direction for elongated structures).

To change the aspect ratio of the rod, we start from a spherical dot with the desired diameter and insert a cylindrical segment along the (001) direction. This procedure

leaves some of the atoms on the NC surface with unsatisfied (dangling) bonds. Surface atoms with only one bond are systematically removed and the dangling bond at the surface of the quantum dots are passivated by pseudo-hydrogen atoms so as to get rid of the surface states. The details of passivation process will be explained in Sec. 2.4. Fig. 2.2 illustrates unpassivated nanostructures whose surface atoms with only one bond (i.e., three dangling bonds) are systematically removed. The effective radius of a dot (R) is defined in terms of the total number of In and As atoms in the dot (N_{dot}) as $R = a(\gamma N_{dot})^{\frac{1}{3}}$, where $\gamma = 3/(32\pi)$ for the zinc-blende crystal structure. The effective radius of a rod is assumed to be equal to that of the dot with the same value of $r_{\rm cut}$ and the aspect ratio (ρ) is defined in term of the ratio of length to diameter (L/D). Because the number of atoms increases quickly with increasing diameter and aspect ratio, as shown in Table 2.1, our calculation for rods with the aspect ratio more than 4.0 is highly impractical due to the prohibitively large number of atoms involved. In the following chapters we will consider the quantum dots and nanorods with $15\text{Å} \leq R \leq 30\text{Å}$ and $1.0 \leq \rho \leq 4.0$.

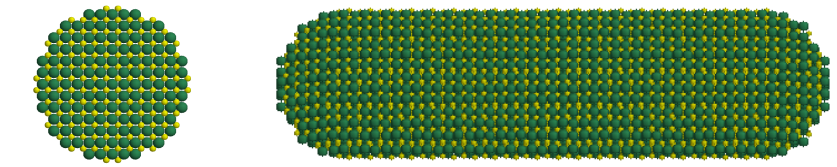

FIGURE 2.2: Unpassivated InAs quantum dot and quantum rod with $R = 20$ Å and the aspect ratio=1.0 and 4.0, respectively. Yellow (green) atoms represent In (As) atoms.

TABLE 2.1: Total number of In and As atoms vs the size of quantum dots and quantum rods. The largest structure calculated here is the quantum rod with the aspect ratio=4.0 and $R = 20$ Å.

radius (Å)	length (Å)	ratio (ρ)	atom number (N_{dot})
20	40	1.0	1,207
24	48	1.0	2,115
30	60	1.0	4,073
20	60	1.5	2,137
20	92	2.3	3,543
20	160	4.0	6,747

2.4 Surface passivation

After the surface atoms with only one bond are systematically removed, the atoms at the surface are not fully bound, i.e., some of whose coordinating atoms have been removed. These are the surface atoms we must passivate. For each such atom, we count how many dangling bond it has. If an atom has more than two dangling bonds, we remove it to prevent overly rough surface. Removal of an atom can result in a neighbour of that atom having more than two dangling bonds, so we repeat the process until there are no such atoms left. If an atom has one or two dangling bonds, we add the appropriate passivant atom c_1, c_2, a_1 and a_2. Note that c_1 and c_2 (a_1 and a_2) are passivants for cations (anions) with one and two dangling bonds, respectively. Therefore, for example, as shown in Fig. 2.3 the In-centred dot requires passivants c_1, c_2 and a_1 because the atoms that lie on the surface are cations with either one and two dangling bonds, and anions with one dangling bond. The same passivation process can be applied to the As-centred dot shown in Fig. 2.3

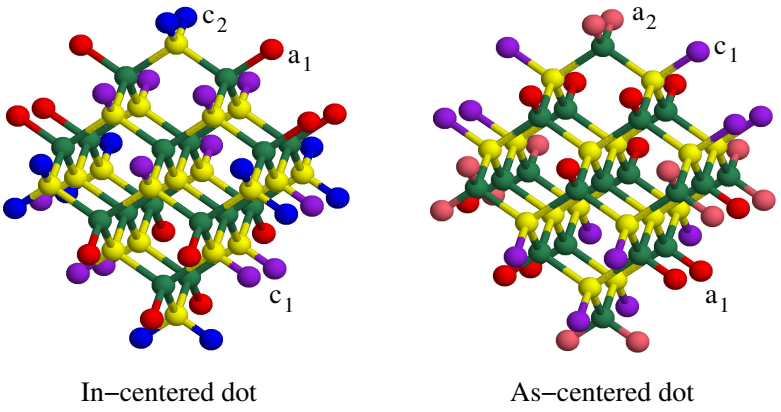

FIGURE 2.3: The surface passivation of zinc-blende InAs quantum dot with D =12 Å (In≡yellow, As≡green, c_1 ≡purple, c_2 ≡blue, a_1 ≡red and a_2 ≡pink). Left : dot 1 is cation centred dot and requires passivants c_1, c_2 and a_1. Right : Dot 2 is anion centred dot and requires passivants c_1, a_1 and a_2.

In our calculation, the dangling bonds at the NC surface (maximum two per atom) are passivated by pseudo-hydrogen atoms, located at a distance ηd_0 $(0 < \eta < 1)$ from the centre of the passivated atom along the direction of the ideal bulk In-As bond of length d_0. The ligand potentials have a Gaussian form

$$v(r) = \alpha e^{-(|r-R_{\rm p}|/\sigma)^2}, \tag{2.5}$$

where $R_{\rm p} = R_{\rm p}(\eta)$ is the location of the passivants, α and σ represent, respectively, the amplitude and width of the Gaussian potential. As our electronic structure calculations are performed in reciprocal space, we use the Fourier transform of Eq. (2.5):

$$v(q) = a e^{iq\cdot R_{\rm p}} e^{-(b|q|)^2} \tag{2.6}$$

where $a \equiv \alpha\pi^{1.5}\sigma^3$ and $b \equiv \sigma/2$. This 12-parameter set (represented by a, b and η for anions and cations with one and two dangling bonds) is optimised on flat (001- 110- 111-oriented slabs) and curved (dots) test structures, using an automated method [91], based on the global optimisation algorithm DIRECT [92]. The quality of a passivation

TABLE 2.2: Four sets of InAs passivant parameters used in this calculation. a is the weight (amplitudes), b is the width of the Gaussian potential, and η is the distance along the ideal bond (the values are in atomic units). c_i and a_i refer, respectively, to cations and anions with $i = 1, 2$ dangling bonds. ξ is the quality of a passivation. Some regularities can be concluded from this table: (i) the optimal anion passivants are typically closer to the atoms they passivate than are the cation passivants, (ii) the amplitudes of anions with two dangling bonds (a_{a_i}) are typically low. This means that they are especially close to the anions they passivate. Both conclusions for InAs quantum dots are similar to the optimal passivants for CdSe [93] and InP [94]. Nonetheless, depending on the material properties and the bulk pseudopotentials that describes the material, this regularity is not expected a priority.

Passivant parameters	set 1	set 2	set 3	set 4
a_{c_1}	1.68	1.97	1.89	1.05
a_{c_2}	1.68	1.97	1.89	1.05
a_{a_1}	-1.05	-1.44	-1.05	-1.05
a_{a_2}	-1.05	-1.05	-1.05	-1.05
b_{c_1}	0.18	0.18	0.18	0.80
b_{c_2}	0.80	0.59	0.80	0.80
b_{a_1}	0.80	0.58	0.64	0.80
b_{a_2}	0.80	0.78	0.80	0.80
η_{c_1}	0.55	0.57	0.55	0.55
η_{c_2}	0.85	0.71	0.85	0.55
η_{a_1}	0.25	0.25	0.25	0.55
η_{a_2}	0.25	0.25	0.25	0.55
ξ	60%	64%	63%	54%

(ξ) is determined by the extent to which the lowermost n states in the conduction band and uppermost m states in the valence band are *not* on the NC surface. A measure of this could be the position of the energy levels with respect to the band gap. However a more stringent test yielding a more quantitative estimate is obtained by integrating the wave functions squared across the interior of each test structure.

We selected the four sets yielding the best passivation according to this criterion and calculated the single-particle gap. The plot of energy gap as a function of effective radius for a series of InAs spherical quantum dots is shown in Fig. 2.4. It can be seen that the band gaps of all sets decrease with increasing radius. This is due to quantum size effect. From the Fig. 2.4, the passivants parameter set 1, 2 and 3 give a very small difference in bandgap for all the sizes considered. This is due to the fact that the first three sets have the same distance for anions (η_{a_1} and η_{a_2}). On the top of that, the amplitudes of the Gaussian potential (w) are not significantly different. In contrast, the parameter set 4 gives a different trend of band gap. Its band gap is fluctuant and it is likely to convert to

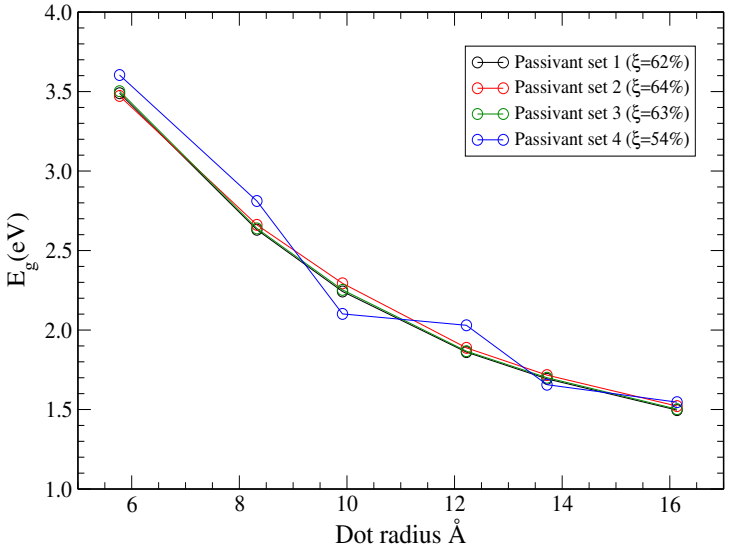

FIGURE 2.4: Bandgap versus effective radius of InAs quantum dot with different sets of passivant parameters. The quality factor (ξ) represents the average percentage of the VBM and CBM wave functions contained in the core of the five test structures.

the bandgaps obtained from set 1, 2 and 3. According to Fig. 2.4, the difference in the results between set 1, 2 and 3 was found to be negligible, showing the independence of the calculated values on the choice of the passivation parameters. We therefore selected the passivant parameters set 2 which gives highest quality factor ($\xi = 64\%$) (see Table 2.2). Having constructed the surface-passivated nanocrystal structures, the following step as schematically shown in Fig. 2.1 is to calculate the crystal potential.

2.5 Pseudopotentials and their construction

The prevailing *continuous models* such as effective-mass approximation and its **k·p** generalization, which are mentioned earlier in Sec. 2.2, are very successful models which have allowed many fundamental physics to be explained. Nonetheless, these available methods are either insufficient or impossibly complicated as they miss the atomistic nature of semiconductor nanostructures. It is therefore worthwhile considering a more complex model to see if they can offer more insights. Particularly, given the approximations that the single band effective mass and envelope function models made to the crystal potential, an obvious improvement would be to consider the potentials of the atoms individually.

The ensuing complexity of such a methodology is illustrated by the form of the complete Hamiltonian ($\hat{H}$):

$$\hat{H} = \hat{H}_{electrons} + \hat{H}_{nuclei} + \hat{H}_{electrons-nuclei} \tag{2.7}$$

where

$$\hat{H}_{electrons} = \sum_{\mu} \left(-\frac{\hbar^2}{2m_0} \bigtriangledown_{\mu}^2 + \sum_{\lambda<\mu} \frac{e^2}{|\mathbf{r}_\lambda - \mathbf{r}_\mu|} \right). \tag{2.8}$$

Note that $\mathbf{r}_\mu$ and m_0 are, respectively, the positions of the electrons and the electron mass. Additionally,

$$\hat{H}_{nuclei} = \sum_{\nu} \left(-\frac{\hbar^2}{2M_\nu} \bigtriangledown_\nu^2 + \sum_{\lambda<\nu} \frac{Z_\lambda Z_\nu e^2}{|\mathbf{R}_\lambda - \mathbf{R}_\nu|} \right) \tag{2.9}$$

where $\mathbf{R}_\nu$ are the positions, Z_μ the atomic numbers and M_ν the masses of the nuclei. Lastly :

$$\hat{H}_{electrons-nuclei} = \sum_{\mu,\nu} \frac{Z_\nu e^2}{|\mathbf{R}_\nu - \mathbf{r}_\mu|} \tag{2.10}$$

However, as a typical macroscopic sample of semiconducting crystal composes of a large number of electrons, the aforementioned problem is therefore insolvable.

To simplify Eq. 2.7 to be a more manageable problem, the *frozen core* approximation has been introduced. It is assumed that the electrons are split into core and valence electrons. The inner-shell localised core electrons are tightly bound to the nucleus and assumed to be unperturbed by their environment. For the non-localised valence electrons, they occupy the outer shells and interact with the potentials of neighbouring atoms. They are responsible for the interatomic binding. Based on this approximation, the number of particles that have to be solved with the Schrödinger equation is therefore reduced as we only need to deal with the valence electrons. On the top of that, the localised core electrons screen the outer valence electrons from the central of the nuclear charge resulting smoothed potentials. Thinking ahead slightly, the smoother the potential then the less terms may be required to construct the wave functions from Fourier series. The *frozen core approximation* is thus the founding of *pseudopotential theory.*

Next, we will consider the formal justification of pseudopotentials. Following the Pauli principle the valence wave functions need to be orthogonal to the core wave functions. This makes the valence wave functions to be fast oscillating in the core region with

high kinetic energy. Here, $|\psi\rangle$ represents the valence wave functions. $|\chi_n\rangle$ and $\{E_n\}$ are, respectively, the core wave functions and their eigenvalues. In order to construct a node-free pseudo-wavefunction $|\phi\rangle$, we assume that

$$|\psi\rangle = |\phi\rangle + \sum_n c_n |\chi_n\rangle. \tag{2.11}$$

Due to the orthogonality relation we obtain

$$\langle\chi_n|\psi\rangle = 0 = \langle\chi_n|\phi\rangle + c_n \rightarrow c_n = -\langle\chi_n|\phi\rangle \tag{2.12}$$

and

$$|\psi\rangle = |\phi\rangle - \sum_n |\chi_n\rangle\langle\chi_n|\phi\rangle. \tag{2.13}$$

Thus the Schrödinger equation for the valence wave functions is $\hat{H}|\psi\rangle = E|\psi\rangle$,

$$\hat{H}|\psi\rangle = \hat{H}|\phi\rangle - \sum_n \hat{H}|\chi_n\rangle\langle\chi_n|\phi\rangle \tag{2.14}$$

$$= \hat{H}|\phi\rangle - \sum_n E_n|\chi_n\rangle\langle\chi_n|\phi\rangle = E|\psi\rangle \tag{2.15}$$

$$= E|\phi\rangle - \sum_n E|\chi_n\rangle\langle\chi_n|\phi\rangle \tag{2.16}$$

and the terms are rearranged :

$$\hat{H}|\phi\rangle + \sum_n (E - E_n)|\chi_n\rangle\langle\chi_n|\phi\rangle = E|\phi\rangle \tag{2.17}$$

At this point, $\hat{H}$ has been split into kinetic $\hat{T}$ and potential $\hat{V}$ terms. With an additional

energy-dependent non-local pseudopotential $\hat{V}_{nl}$, we then obtain the node-free pseudo-wavefunctions that fulfil a Schrödinger equation :

$$\hat{T}|\phi\rangle + \Big\{\hat{V} + \underbrace{\sum_{n}(E - E_n)|\chi_n\rangle\langle\chi_n|}_{\text{non-local pseudopotential}}\Big\}|\phi\rangle = E|\phi\rangle. \tag{2.18}$$

The terms in curly brackets are the *pseudopotentials*, composed of a positive attractive part $\hat{V}$ and a negative repulsive part $\hat{V}_{nl}$. These terms represent the crystal potentials that are not only the interaction between the electrons and nuclei of atoms constituting the lattice, but also the interaction between electrons themselves. The Schrödinger equation for the Eq. 2.17 can be rewritten as

$$\langle\psi|\hat{H}|\phi\rangle + \sum_{n}(E - E_n)\langle\psi|\chi_n\rangle\langle\chi_n|\phi\rangle = E\langle\psi|\phi\rangle. \tag{2.19}$$

It is noticed that the eigenvalues of the real and the pseudopotential are identical as $\langle\psi|\chi_n\rangle = 0$ due to the orthogonality of the core and valence states as mentioned in the Pauli principle. At this point, we have given a formal derivation of *pseudopotentials*. We next explain the construction of empirical pseudopotentials and follow by semiempirical pseudopotentials which are mainly used in the thesis.

The empirical pseudopotential method (EPM) has been developed since 1960s to describe the bulk band structure of semiconductors. In this methodology, a superposition of non-self-consistent screened pseudopotentials is used to represent the total potential of the system. It involves a fit of the reciprocal space pseudopotential $V(G)$ to experimentally known quantities such as certain points of band structure, experimental band gap and effective masses of bulk semiconductor, etc. In this approach, it is assumed that the total screened pseudopotential of the crystal $V(\mathbf{r})$ can be written as a superposition

of atomically screened potentials $v_\alpha(\mathbf{r})$ at sites R_n for atom type α :

$$V(\mathbf{r}) = \sum_{\alpha,j,n} v_\alpha(\mathbf{r} - \mathbf{R}_n - \mathbf{r}_{\alpha,j}), \tag{2.20}$$

where n is the index for the primitive unit cells and $\mathrm{r}_{\alpha,j}$ is the basis vector for atom j in unit cell n. The potential of a crystal with only one type of atoms, for example, in reciprocal space can be written as

$$V(\mathbf{r}) = \sum_{\mathbf{G}} v(\mathbf{G}) S(\mathbf{G}) e^{i\mathbf{G}\mathbf{r}}, \tag{2.21}$$

where

$$S(\mathbf{G}) = \frac{1}{n} \sum_{j} e^{-i\mathbf{G}\mathbf{r}_j}, \tag{2.22}$$

and n is the number of basis atoms. $S(\mathbf{G})$ is called the *structure factor* which only depends on the geometry. The reciprocal space functional form of the pseudopotential $v(\mathrm{G})$ can be represented by a function [122]

$$v_\alpha(q) = a_{1\alpha} \frac{(q^2 - a_{1\alpha})}{a_{3\alpha} e^{a_{4\alpha} q^2} - 1}, \tag{2.23}$$

where $a_{1\alpha}, a_{2\alpha}, a_{3\alpha}, a_{4\alpha}$ are adjustable parameters. At this point, the parameters from Eq. 2.23 are fitted to reproduce known experimental quantities such as the bulk band structure at the high symmetry points, the effective masses for different bands at different k-points and along different reciprocal space directions, the deformation potentials, and the surface work function. Early applications for this procedure were applied for Si and Ge [95, 96], and then were successfully extended to 14 different semiconductors [97] with surprisingly accurate results.

The semiempirical pseudopotential method or SEPM, basically used in this thesis, was

in recent developed in 1995 by Lin-Wang Wang and Alex Zunger [98]. They improved the conventional EPM by a two-step process. First, a set of self-consistently screened local-density-approximation (LDA) potentials is inverted for a range of bulk crystal structures and unit cell volumes. Therefore, spherically-symmetric and structurally averaged atomic potentials (SLDA) were determined. It was found that these potentials can be used to reproduce the LDA band energies and wave functions extremely well for most common structure of that material. Second, small adjustments to the potentials are made so as to fit the bulk band structure to the experimentally measured excitation energies. The adjustment represents a reasonably small perturbation over the SLDA potential, while the ensuing wave function preserves a large overlap with the original LDA values. These semiempirical pseudopotentials therefore combine LDA quality wave functions with experimentally consistent excitation energies, effective masses, and deformation potentials.

It is worth comparing the SEPM with the well-known empirical pseudopotential method (EPM). Without check, the conventional EPM sometimes gives inaccurate wave functions. On the one hand, the SEPM can produce a large overlap with the LDA wave functions and also reproduce experimental excitation energies. On the other hand, in the traditional EPM, $v^{(\alpha)}(r)$ was adjusted to fit the single-particle excitation spectra regardless of the quality of the associated wave functions and charge densities. Moreover, while the EPM is suitable for a particular crystal structure and lattice constant, the state-of-art SEPM can be used for different structures and volumes with good transferability. Taking into account of all these factors, this SEPM can provide a systematic procedure and information on the transferability of the effective potentials.

2.6 Solution of the single particle problem

2.6.1 Single particle Schrödinger equation

Having constructed the crystal potential, the next step in the calculation of the excitonic structure of a nanocrystal is the solution of the single-particle problem. In the semiempirical pseudopotential approach the single-particle Schrödinger equation is given by

$$\left(-\frac{\hbar^2}{2m_0}\nabla^2 + V_{\rm ps}^{\rm SEPM}(\mathbf{r}) + \hat{V}_{\rm nl}\right)\psi_{\rm i}(\mathbf{r}) = \epsilon_{\rm i}\psi_{\rm i}(\mathbf{r}), \tag{2.24}$$

where $V_{\rm ps}^{\rm SEPM}(\mathbf{r})$ is the microscopic pseudopotential of the system (dot plus surrounding material), and $\hat{V}_{\rm nl}$ is a short-range operator that accounts for the nonlocal part of the potential (including spin-orbit coupling). $V_{\rm ps}^{\rm SEPM}(\mathbf{r})$ is calculated from the superposition of the screened atomic potentials in Eq. 2.20. Our primary goal is to achieve interior eigenvalues on either side of the bandgap, which determines most of the properties related to excitations.

2.6.2 Folded spectrum method (FSM)

The conventional variational method to solve Hamiltonian in Eq. 2.24 is to minimise the energy $\langle\psi|\hat{H}|\psi\rangle$ by varying the expansion coefficients of ψ. Once the first ψ with the lowest energy of $\hat{H}$ is obtained, one needs to orthogonalize ψ to all energy below it in order to calculate higher states. To accomplish this orthogonalization the calculation scales as N^3 where N is the number of atoms in the system. Consequently, this conventional methodology can only deal with a small system ($N \leq 1,000$ atoms) in spite of the fact that parallel in computing has increased the size of systems amenable to treatment via Eq. 2.24.

Due to the aforementioned problem, folded spectrum method (FSM) was therefore introduced in 1983 by L. W. Wang and A. Zunger. After that, this approach has been serving as the main engine for large scale non-selfconsistent calculations. In this methodology, we calculate eigen-solutions around an interesting energy without having to calculate any of the wave functions below it. The calculation scales linearly with the system's size; hence, we are able to calculate the eigen-solutions around the band-edge and the properties in microscopic systems could be addressed. The basic idea of this method is that the solutions are identical to those of Eq. 2.24 and also satisfy

$$\left(-\frac{\hbar^2}{2m_0}\nabla^2 + V_{\rm ps}^{\rm SEPM}(\mathbf{r}) + \hat{V}_{\rm nl} - \epsilon_{\rm ref}\right)^2 \psi_{\rm i}(\mathbf{r}) = (\epsilon_{\rm i} - \epsilon_{\rm ref})^2 \psi_{\rm i}(\mathbf{r}), \tag{2.25}$$

where $\epsilon_{\rm ref}$ is an *arbitrary* reference energy. In order to obtain the identical solution, the spectrum of $\epsilon_{\rm i}$ of $\hat{H}$ has been folded at the reference point of $\epsilon_{\rm ref}$ into spectrum

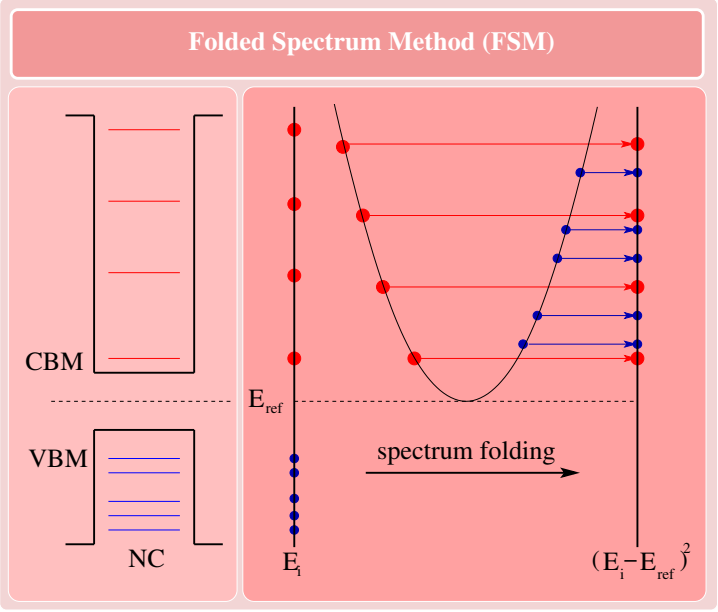

FIGURE 2.5: The schematic view of the folded spectrum method (FSM). The spectrum at the left is the original spectrum of $\hat{H}$. The spectrum at the right is the folded spectrum of $(\hat{H} - \epsilon_{\rm ref})^2$. Notice that, the CBM or VBM state is the lowest energy in the folded spectrum.

$(\epsilon_{\rm i} - \epsilon_{\rm ref})^2$ of $(\hat{H} - \epsilon_{\rm ref})^2$. As illustrated in Fig. 2.5, the lowest solution of Eq. 2.25 is the eigenstate with $\epsilon_{\rm i}$ closest to $\epsilon_{\rm ref}$. Hence, by placing $\epsilon_{\rm ref}$ in the interesting range, such as in the bandgap, one transforms an arbitrarily high eigen-solution into the lowest one, regardless of the orthogonalisation of the function $A[\psi] = \langle\psi|(\hat{H} - \epsilon_{\rm ref})^2|\psi\rangle$. This will enable us to find either the CBM or VBM, depending on which is closer to $\epsilon_{\rm ref}$. Changing $\epsilon_{\rm ref}$ within the gap region then assures that both the CBM and VBM are found.

2.7 The calculation of many-body effects

Once the single-particle problem has been calculated, the next step for the calculation of an an optical absorption spectrum requires a solution for the *two-body* electron-hole problem. Formally, the correlated exciton wavefunctions can be constructed from a set of single-substitution Slater determinant $\Phi_{\rm v,c}$ by promoting an electron from the occupied valence state $\psi_{\rm v}$ of energy $\epsilon_{\rm v}$ to the unoccupied conduction state $\psi_{\rm c}$ of the energy $\epsilon_{\rm c}$:

$$\Phi_0(\mathbf{r}_1, \sigma_1, ..., \mathbf{r}_{\rm N}, \sigma_{\rm N}) = \xi[\psi_1(\mathbf{r}_1, \sigma_1) \cdots \psi_{\rm v}(\mathbf{r}_{\rm v}, \sigma_{\rm v}) \cdots \psi_{\rm N}(\mathbf{r}_{\rm N}, \sigma_{\rm N})] \tag{2.26}$$

$$\Phi_{\rm v,c}(\mathbf{r}_1, \sigma_1, ..., \mathbf{r}_{\rm N}, \sigma_{\rm N}) = \xi[\psi_1(\mathbf{r}_1, \sigma_1) \cdots \psi_{\rm c}(\mathbf{r}_{\rm v}, \sigma_{\rm v}) \cdots \psi_{\rm N}(\mathbf{r}_{\rm N}, \sigma_{\rm N})] \tag{2.27}$$

where the spin variables are represented by $\sigma = \uparrow, \downarrow$, N is the total number of electrons in the system, and ξ is the antisymmetrizing operator. It is worth noticing that the single-particle valence state $\psi_{\rm v_1}$ and $\psi_{\rm v_2}$, as well as the single-particle conduction states $\psi_{\rm c_1}$ and $\psi_{\rm c_2}$ are *degenerate* if two Slater determinants $\Phi_{\rm v_1,c_1}$ and $\Phi_{\rm v_2,c_2}$ belong to the same configuration. That is, $\epsilon_{\rm v_1} = \epsilon_{\rm v_2}$ and $\epsilon_{\rm c_1} = \epsilon_{\rm c_2}$. In other words, each exciton configuration has a minimum dimension of four. Thus the exciton wave function Ψ^{α} can

be expanded in term of the basis set,

$$\Psi^{\alpha} = \sum_{\mathrm{v}=1}^{\mathrm{N_v}} \sum_{\mathrm{c}=1}^{\mathrm{N_c}} C_{\mathrm{v,c}}^{\mathrm{N_c}} \Phi_{\mathrm{v,c}}, \tag{2.28}$$

where N_v and N_c denote the number of valence and conduction states included in the expansion of the exciton wave functions. Inclusion of multi-substitution Slater determinants will introduce additional multi-exciton levels at higher energy.

The Slater rule allows us to express the matrix elements between Slater determinants in term of

$$\hat{H}_{\mathrm{vc,v'c'}} = \langle \Phi_{\mathrm{v,c}} | \hat{H} | \Phi_{\mathrm{v',c'}} \rangle = (\epsilon_{\mathrm{c}} - \epsilon_{\mathrm{v}}) \delta_{\mathrm{v,v'}} \delta_{\mathrm{c,c'}} - J_{\mathrm{vc,v'c'}} + K_{\mathrm{vc,v'c'}}, \tag{2.29}$$

where J and K are the Coulomb and exchange integrals, respectively.

When electrons are introduced in the conduction band (or holes in the valence band), the electrons which are fermions interact strongly with each other. Electron-electron interaction results on a downward shift in the conduction band edge. This shift is caused by electron exchange energy which evolves from the Pauli exclusion principle. When the electron concentration in the semiconductor becomes sufficiently large, their wavefunctions begin to overlap. Consequently, the Pauli exclusion principle becomes operative, and the electrons spread in their momenta in such a way that the overlapping of the individual electron wavefunctions is avoided. The Bloch states are thus modified by the presence of the other electrons. In general, the electron-electron interaction can be represented by the usual Coulombic interaction and the exchange interaction. The latter comes about due to the constraint of the Pauli exclusion principle which forces any multiparticle electronic wavefunction to be antisymmetric in the exchange of two electrons. The exchange term, which keeps the electrons away from each other, then lowers the energy of the system.

Here the electron-hole Coulomb energy, $J_{\mathrm{vc,v'c'}}$, between each of the possible electron-hole pairs can be calculated by direct integral of the single -particle wavefunctions as

$$J_{\mathrm{vc,v'c'}} = e^2 \sum_{\sigma_1,\sigma_2} \int\int \frac{\psi^*_{\mathrm{v'}}(\mathbf{r}_1,\sigma_1)\psi^*_{\mathrm{c}}(\mathbf{r}_2,\sigma_2)\psi_{\mathrm{v}}(\mathbf{r}_1,\sigma_1)\psi_{\mathrm{c'}}(\mathbf{r}_2,\sigma_2)\mathrm{d}\mathbf{r}_1\mathrm{d}\mathbf{r}_2}{\bar{\epsilon}(\mathbf{r}_1,\mathbf{r}_2)|\mathbf{r}_1-\mathbf{r}_2|} \tag{2.30}$$

and the exchange integral, $K_{\mathrm{vc,v'c'}}$, is calculated by

$$K_{\mathrm{vc,v'c'}} = e^2 \sum_{\sigma_1,\sigma_2} \int\int \frac{\psi^*_{\mathrm{v'}}(\mathbf{r}_1,\sigma_1)\psi^*_{\mathrm{c}}(\mathbf{r}_2,\sigma_2)\psi_{\mathrm{c'}}(\mathbf{r}_1,\sigma_1)\psi_{\mathrm{v}}(\mathbf{r}_2,\sigma_2)\mathrm{d}\mathbf{r}_1\mathrm{d}\mathbf{r}_2}{\bar{\epsilon}(\mathbf{r}_1,\mathbf{r}_2)|\mathbf{r}_1-\mathbf{r}_2|}. \tag{2.31}$$

Next we will perform configuration interaction (CI). The calculation of configuration interaction in quantum chemistry is often treated at the level of triples, quadruplets, which exactly solves the electronic Schrödinger equation based on the one-particle basis set. In such a calculation, the Coulomb integrals are computationally unscreened. In contrast, for excitations in a nanostructure, such a procedure is not possible and it has to limit itself in the one-particle basis set to the investigation of only a few states close to the bandgap and to single excitation only. In order to study the electronic excitations in nanostructures, ignoring of the coupling of singles to higher excitations is a poor approximation. However, it has been found that the effect of higher-order excitations can be folded back onto the considered subspace of single excitations [99]. The effect of this procedure is to *screen* (renormalize) the Coulomb and exchange interactions, as shown earlier in Eq. 2.30 and 2.31. Here, a position-dependent dielectric constant is used to screen the Coulomb and exchange interaction in quantum dots according to the electron-hole separation. The screened Coulomb potential of Eq. 2.30 and 2.31 can be generally written as

$$g(\mathbf{r}_e,\mathbf{r}_h) = e^2 \int \epsilon^{-1}(\mathbf{r}_e,\mathbf{r})|\mathbf{r}-\mathbf{r}_h|^{-1}\mathrm{d}\mathbf{r} \tag{2.32}$$

with the inverse dielectric function ϵ^{-1}. Assuming that $\epsilon^{-1}(\mathbf{r}_1, \mathbf{r}_2) \approx \epsilon^{-1}(\mathbf{r}_1 - \mathbf{r})$, the Fourier transform of the screened Coulomb potential is

$$g(k) = \epsilon^{-1}(k)\frac{4\pi e^2}{k^2} \tag{2.33}$$

where $\epsilon^{-1}(k)$ is the Fourier transform of $\epsilon^{-1}(\mathbf{r}_1 - \mathbf{r})$. For the electronic screening of the exciton we used the model proposed by Haken in which the inverse dielectric constant constant $\epsilon^{-1} = \epsilon_{\text{el}}^{-1} + \epsilon_{\text{ion}}^{-1}$ consists of an electric (high-frequency) contribution $\epsilon_{\text{el}}^{-1}$ and an ionic (low-frequency) contribution $\epsilon_{\text{ion}}^{-1}$. The approximation of both the electronic and iconic parts are based on the Thomas-Fermi model. Both terms are generally defined as

$$\epsilon_{\text{el}}^{-1} = \frac{k^2 + q^2 \sin(k\rho_\infty)/(\epsilon_\infty^{\text{dot}} k\rho_\infty)}{k^2 + q^2} \tag{2.34}$$

$$\epsilon_{\text{ion}}^{-1}(k) = \left(\frac{1}{\epsilon_0^{\text{dot}}} - \frac{1}{\epsilon_\infty^{\text{dot}}}\right)\left(\frac{1/2}{1 + \rho_{\text{h}}^2 k^2} + \frac{1/2}{1 + \rho_{\text{e}}^2 k^2}\right) \tag{2.35}$$

where q is the Thomas-Fermi wavevector and it is defined as $q = 2\pi^{-\frac{1}{2}}(3\pi^2 n_0)^{\frac{1}{3}}$, n_0 is the electron density and ρ_∞ is the solution of $\sinh(q\rho_\infty)/(q\rho_\infty) = \epsilon_\infty^{\text{dot}}$. Here $\rho_{\text{h,e}} = (\hbar/2m_{\text{h,e}}^* \omega_{\text{LO}})^{\frac{1}{2}}$, with $m_{\text{h,e}}^*$ are the electron and hole effective mass and ω_{LO} is the bulk LO-phonon frequency.

For small colloidal nanocrystals, it is not appropriate to use the approximation of bulk screening due to an increasing role of the interface effect. We used a modified screening function where the radius of colloidal quantum dots is taken into account. In this approximation we replace the high-frequency bulk dielectric constant ϵ_∞ in Eq. 2.32 with a constant ϵ_∞^{dot} obtained from a modified Penn model. The size dependence is introduced to the equation through the value of the optical bandgap of the dot. The low frequency dielectric constant of the dot ϵ_0^{dot} was obtained by assuming that the dot

interior is bulk-like so $\epsilon_0^{\rm dot} - \epsilon_\infty^{\rm dot}$ can be approximated from the bulk,

$$\epsilon_0^{\rm dot} - \epsilon_\infty^{\rm dot} = \epsilon_0^{\rm bulk} - \epsilon_\infty^{\rm bulk} = \Delta\epsilon_{\rm ion}^{\rm bulk}. \tag{2.36}$$

In this approximation, the dielectric function remains dependent on the distance $|\mathbf{r} - \mathbf{r}'|$ but is independent of the position of $\mathbf{r}$. As a result, screening is typically reduced throughout the nanostructures. $\epsilon_\infty^{\rm dot}$ is obtained from the Penn model and it is generally defined as

$$\epsilon_\infty^{\rm dot} = 1 + (\epsilon_\infty^{\rm bulk} - 1)\frac{(E_{\rm gap}^{\rm bulk} + \Delta)^2}{(E_{\rm gap}^{\rm dot}(R) + \Delta)^2} \tag{2.37}$$

where $\Delta = E_2 - E_{\rm gap}^{\rm bulk}$. E_2 is the second strong peak from the experimental emission spectra. Unlike the dielectric constants in the effective mass and tight-binding calculations, the dielectric function used in our framework depends both on the electron-hole separation and the quantum dot size. Besides, in the effective mass and tight-binding calculations the electron-hole exchange interaction was either unscreened or screened by the *bulk* distance-dependent dielectric constant.

In the case of a spherical NC, for example, we use the uppermost 60 states in the valence band and lowermost 8 states in the conduction band for this expansion, yielding a total of 480 excitonic configurations. The exciton states of the quantum dot are obtained by solving the secular equation

$$\sum_{\rm v'=1}^{\rm N_v}\sum_{\rm c'=1}^{\rm N_c} H_{\rm vc,v'c'} C_{\rm v',c'}^{(\alpha)} = E^{(\alpha)} C_{\rm v,c}^{(\alpha)}. \tag{2.38}$$

The single-particle and excitonic pictures are shown in Fig. 2.6. The single-particle levels are labelled as p_n, where $p = e, h$ is the charge carrier and n is the order of the level (increasing from 1 starting from the CBM upwards for e and from the VBM

downwards for h). $\times d$ indicates the degeneracy (including spin). The zero of the energy is set arbitrarily at the position of the VBM. Single-exciton levels $|1h, 1e\rangle$ are labelled according to the SP states from which they originate as (h_n, e_m). The zero of the energy is at the ground state $|0h, 0e\rangle$ (i.e, the state with 0 electrons and 0 holes). In the case of InAs spherical NCs, the lowermost exciton manifold $(h_{1,2}, e_1)$ originates from the SP states $h_{1,2}$ (VBM) and e_1 (CBM) and has therefore a total degeneracy of $4 \times 2 = 8$. However exchange interaction splits it into a lower 3-fold degenerate multiplet, a middle 2-fold and a higher 3-fold degenerate multiplets, separated by energy gaps of the order of hundreds of μeV (not shown). We find very little configuration mixing in our InAs spherical NCs, with most excitons receiving a contribution $\geq 99\%$ from a single electron-hole pair (h_n, e_m).

The configuration-interaction (CI) spectrum is obtained by diagonalizing of the Hamiltonian matrix in Eq. 2.38. Fig. 2.7 illustrates the convergence of the configuration-interaction expansion in term of the size of the determinantal basis set. This figure

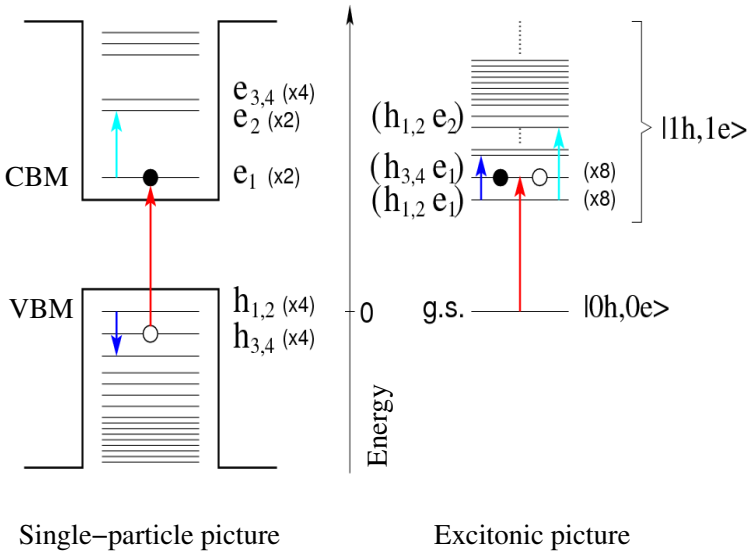

FIGURE 2.6: Schematics of energy levels and degeneracies in the single-particle (left-hand side) and excitonic (right-hand side) pictures. The arrows indicate intra-band (blue and cyan) and inter-band (red) absorption processes.

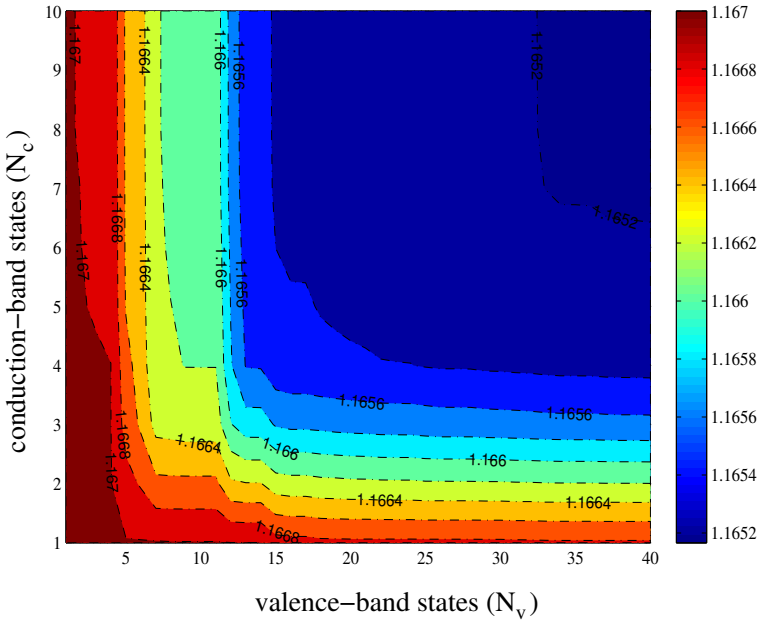

FIGURE 2.7: Convergence of the lowest exciton energy in InAs NC (R=20 Å) with the number of valence-band states (N_v) and conduction-band states (N_c) included in the expansion of Eq. 2.38.

shows a 2-D plot of the lowest exciton energy of an InAs NC (R=20 Å) as a function of the number of valence states (N_v) and conduction states (N_c) included in the many-body expansion of Eq. 2.38. As we can see from Fig. 2.7, the convergence of the exciton energy levels is relatively fast. The difference in the single-particle energy between e_4 and e_5 is about 300meV. Therefore, expanding the exciton states using 30 valence states and 4 conduction states, corresponding to a CI basis set of 480 configurations, is sufficient for the investigation in the bandage optical properties.

Once the exciton wave functions have been obtained by diagonalizing the CI Hamiltonian, the dipole matrix elements for the optical interband absorption are calculated as:

$$M^{(\mathrm{a})} = \sum_{\mathrm{v,c}} A^{(\mathrm{a})}_{\mathrm{v,c}} \langle \psi_\mathrm{v} | \mathbf{r} | \psi_\mathrm{c} \rangle \tag{2.39}$$

where the coefficients $A^{(\mathrm{a})}_{\mathrm{v,c}}$ are the eigenstates of the CI Hamiltonian. Having calculated

the dipole matrix elements, next we will be able to calculate observables through the use of post-processor tools as illustrated in the final step of the flowchart in Fig. 2.1

2.8 Optical properties

2.8.1 Absorption and emission spectrum

The optical absorption spectrum is calculated by

$$I(E) = \frac{1}{V} \sum_{a} |M^{(a)}|^2 \; e^{-\left(\frac{E - E^{(a)}}{\Gamma}\right)^2} \tag{2.40}$$

where $E^{(a)}$ is the exciton energy and Γ represents an experimental line broadening. All absorption spectra (i.e., those relative to both intra- and inter-band transitions) in this work are calculated using excitonic states. However, as the single-particle picture is often more intuitive, and given that the exciton states are found to be contributed to almost exclusively ($\geq$99%) by a single configuration, all absorption spectra presented in the following Chapters are accompanied by the relevant calculated SP spectra illustrating the transitions between the single-particle states from which the different excitons involved originate. Intra- and inter-band transitions are represented schematically by colored arrows in Fig. 2.6.

2.8.2 Stokes shift

When a semiconductor nanocrystal absorbs a photon, it gains energy and enters an excited state. The nanostructure can then relax via two possible mechanisms. One way for the system to relax would be the loss of heat energy, and another feasible relaxation process is to emit a photon. In the emission process if the emitted photon has less

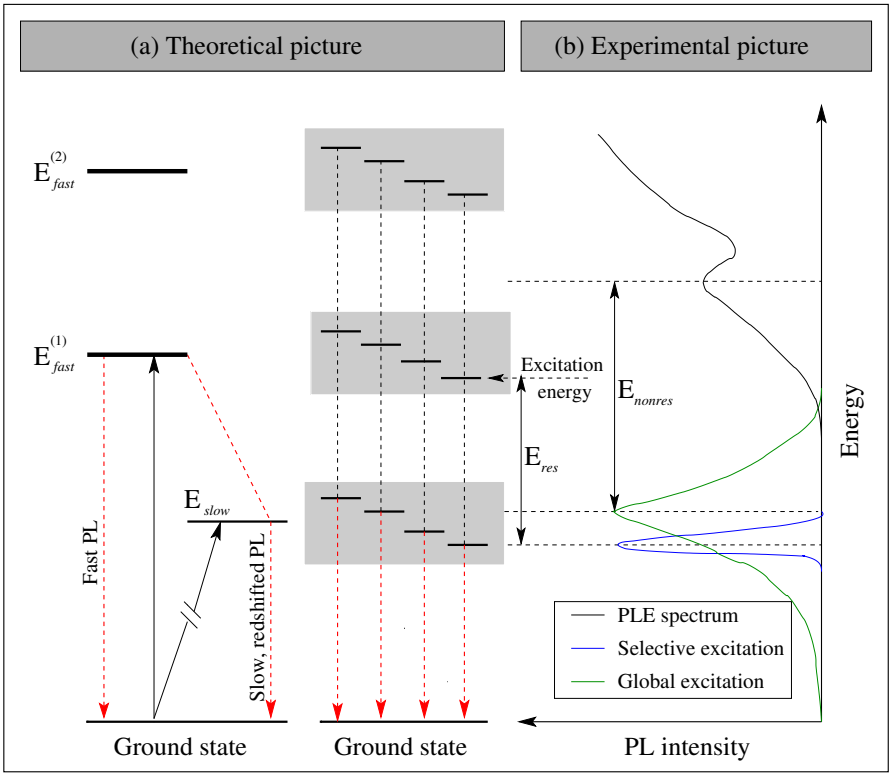

FIGURE 2.8: Schematic illustration of the "*resonant*" and "*nonresonant*" Stokes shift from both theoretical and experimental point of view. (a) (Left) The absorption and emission are represented by black and red dashed arrows, respectively. The transition from ground state to E_{slow} state is forbidden, indicating by the broken solid arrow. (a) (Right) The excited energy levels of the dots present in a given sample form groups. In each group, there are many states reflecting the variation of dot sizes. (b) The black solid line indicates "photoluminescence excitation" (PLE) spectroscopy showing the absorption spectra of all optically allowed states. The green solid line represents the "global excitation spectroscopy" in which all sizes in the sample are excited and the emission is monitored at all energy. The blue solid line indicates "selective excitation spectroscopy" or "fluorescence line narrowing" (FLN) in which the larger dots are selectively excited. The emission is therefore narrowed and reflect an intrinsic redshift of a given dot size.

energy than the absorbed photon, the difference in energy is the so-called Stokes shift. In general, Stokes shift is typically defined as the energy difference (either in wavelength or frequency units) between positions of the absorption and emission spectra of the same electronic transition.

Stokes shift is one of the almost universal features in semiconductor nanostructures. It has been seen in quantum dots of Si [100–102], CdSe [41, 42, 103–108], InP [109], CdS

[110] and InGaAs [111]. There are various causes for the Stokes shift. One obvious reason for the redshift is the existence of large size variation in experimental samples. Due to the size-dependent confinement effect, the larger dots in a sample have lower bandege energies, as illustrated in horizontal lines in Fig. 2.8. Thus, if one excites a sample with sufficiently-high-energy photons above the band edge of the smallest dot, the emission will be redshifted because it results from the de-excitation of band edges of *all* the dots in the sample. The difference between the lowest-energy peak in the emission peak and absorption spectra is called "*nonresonant Stokes shift*" (E_{nonres})

Though it is possible to eliminate the effect of size distribution by exciting selectively only the largest dots in a sample by using the fluorescence line narrowing (FLN), it still gives the difference between excitation line and the FLN emission peak (the "*resonant Stokes shift*" E_{res}), reflecting an intrinsic redshift of a given dot. It has been found that the larger the size of the dot, the smaller the resonant Stokes shift. These findings can be explained in term of a schematic energy-level diagram shown in Fig. 2.8, where E_{fast} and E_{slow} denote, respectively, the fast, high-energy, *allowed* state and the slow, redshifted *forbidden* state. A large volume of studies have aimed at identifying the origin and nature of the excited states E_{fast} and E_{slow}. One possible reason is the *intrinsic, spin-forbidden state*. In this model, it is assumed that in the small nanostructures the electron-hole exchange interaction is sufficiently enhanced so as to split the electron-hole state into a lower energy, *spin-forbidden* component E_{slow} and a higher energy, *spin-allowed* component E_{fast}. Therefore, the observed emission versus absorption redshift is the exchange splitting. In addition, the observed long lifetime of the emission from E_{slow} to the ground state is due to the spin-forbidden character of E_{slow} with respect to the ground state. Another possibility consists of the electron and hole having different spatial envelope function symmetries. When the highest hole state (VBM) and the lowest electron state (CBM) have different envelope function symmetry, the dipole transition

element between both states is zero. The transition from E_{slow} to ground state will be both red shifted and slow.

2.8.3 Degree of linear polarisation

Due to the geometrical anisotropy and the resulting deconfinement along one direction, in NRs the absorption/emission intensity $I_{\parallel}$ of light polarised parallel to the long axis can be different from that ($I_{\perp}$) of light polarised perpendicular to it. The ensuing polarization anisotropy is typically defined in terms of the polarisation ratio [112] (also called the degree of linear polarisation)

$$\beta = \frac{I_{\parallel} - I_{\perp}}{I_{\parallel} + I_{\perp}}. \tag{2.41}$$

2.8.4 Radiative lifetime

The thermally averaged lifetime $\tau_{\mathrm{R}}(T)$ is calculated in the framework of time-dependent perturbation theory [113–115] as:

$$\frac{1}{\tau_{\mathrm{R}}(T)} = \frac{\sum_{\gamma}(1/\tau_{\gamma})e^{-(E_{\gamma}-E_0)/k_{\mathrm{B}}T}}{\sum_{\gamma} e^{-(E_{\gamma}-E_0)/k_{\mathrm{B}}T}} \tag{2.42}$$

where the intrinsic lifetime τ_{γ} is defined as

$$\frac{1}{\tau_{\gamma}} = \frac{4nF^2\alpha\omega_{\gamma}^3}{3c^2}|M_{i\to j}|^2. \tag{2.43}$$

Here α is the fine structure constant, $\hbar\omega_{\gamma}$ is the transition energy, c is the speed of light in vacuum, $M_{i\to j}$ is the CI dipole matrix element [88], n is the refractive index of

the medium surrounding the NC, $F = 3\varepsilon/(\varepsilon_{\text{dot}} + 2\varepsilon)$ is the screening factor ($\varepsilon = n^2$), and ε_{dot} is the dielectric constant of the NC calculated by a modified Penn model [43]. For the dielectric constant of the surrounding matrix three different values were chosen, representative of different NC environments: (i) $\varepsilon_{\text{out}} = 2.5$ consistent with the presence of a common solvent (such as toluene) around the NCs; (ii) $\varepsilon_{\text{out}} = 4.5$ an estimate obtained in Ref. [5] as the best fit of their theoretical data to the experimental results (this *effective* dielectric constant was used here in an attempt to account for the presence of organic ligands on the NC surface as well); and (iii) ε_{out}=6.0 consistent with the presence of a CdSe shell around the NC (in InAs/CdSe core/shell structures).

In the following Chapters, the atomistic pseudopotential method discussed in this Chapter will be used to investigate the electronic and optical properties in InAs nanostructures with different shapes, starting from spherical quantum dots in Chapter 3, slightly elongated dots in Chapter 4, and nanorods in Chapter 5.

Chapter 3

Spherical InAs Nanocrystals

In this chapter the atomistic pseudopotential approach discussed in the previous chapter is used to investigate the electronic and optical properties of spherical InAs nanocrystals (NCs). Starting from the review of the recent theoretical and experimental investigations, we found that the complex structure of valence and conduction band in this quantum-confined structure is still a controversial issue leading to disparate interpretations of the experimentally observed features. Here we present our accurate pseudopotential calculation of interband and intraband transitions in InAs nanocrystal quantum dots. We start our calculation from the single-particle picture before the excitonic picture is subsequently considered. Throughout this chapter, our methodology can present itself as a suitable tool to reproduce a large volume of experimental results and this is a promising start for the study in a wide variety of quantum-confined structures in the following chapters.

3.1 Recent investigations of spherical InAs NCs

The evolution of the electronic structure of semiconductor nanocrystals as a function of size manifests itself as the transition from the molecular to the solid state regime. To

date, a number of observations of atomic-like electronic states in semiconductor NCs have been reported [2, 59]. In particular, InAs quantum dots have been the subject of a large volume of experimental [2, 4, 116, 116] and theoretical [5, 90, 117–122] work, as they provide a typical example of quantum confined systems in the technologically important group of narrow-gap materials, and exhibit a spectrum of interesting properties that can find a wide range of applications.

Experimentally it is possible to resolve up to about 9 peaks in the interband absorption spectra of colloidal InAs dots [4]. However, despite the extensive investigations conducted over the past decade, the origin of some of the optical transitions is still unclear. There is therefore scope for the application of a more accurate theoretical treatment to try to improve our understanding of such features.

One of the most widely used theoretical approaches is the continuum-like $\mathbf{k}\cdot\mathbf{p}$ method [117]. Banin *et al.* [4] used an eight-band $\mathbf{k}\cdot\mathbf{p}$ approach to study the size dependence of the optical transitions in InAs nanocrystals. As illustrated in Fig. 3.1 (a) , they found that the energy of the observed ground state transition, identified as the optically allowed transition between the valence band maximum (VBM, $1S_{3/2}$) and the conduction band minimum (CBM, $1S_{1/2}$), deviated substantially from the prediction of their model when the radius of the NCs was less than 20 Å. Furthermore the multi-band effective mass model used in Ref.[4] entirely missed the second optical transition and achieved a good agreement with experiment only for the observed *strong* transitions, whereas the agreement for the weaker peaks was less satisfactory. The authors speculated that the discrepancy found for the ground state energy could have been due to an underestimate of the electron wave function penetration into the barrier or to the over simplified calculation of electron-hole Coulomb interaction in the smallest crystals, in which the dielectric constant was taken as the static dielectric constant of bulk.

Using a different parametrization for the eight-band effective mass Hamiltonian, Zhu and co-workers [118] found instead that the envelope function of the ground hole state (VBM) in InAs spherical dots has p symmetry and that therefore the transition from this level to the CBM ($1S_{1/2}$) is optically forbidden. Their calculated absorption spectrum, however, misses completely the sixth experimental peak and adds one extra unseen transition between the observed fourth and fifth peaks.

Another broadly used method is the atomistic tight-binding model (TB) [5, 90, 119, 120]. The advantage of this method is that it allows to study large systems easily as the atomistic detail is limited to a small basis set. Furthermore, the TB model provides a

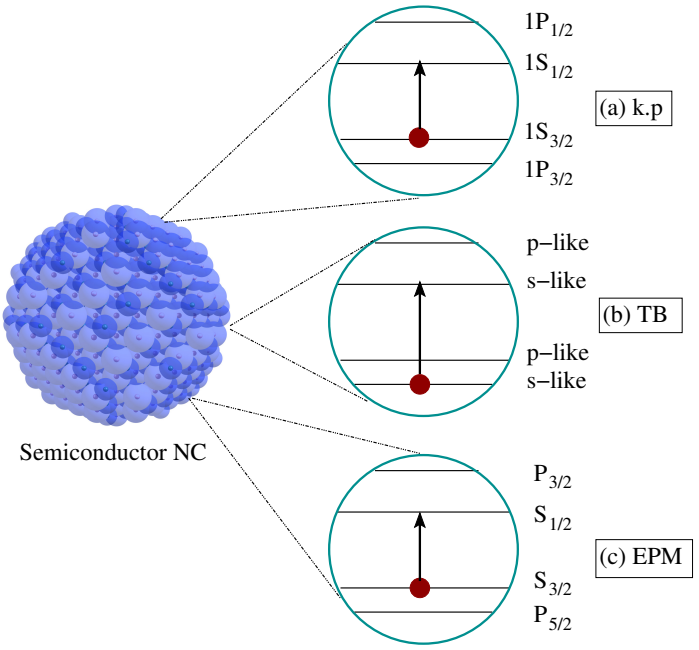

FIGURE 3.1: InAs semiconductor nanocrystal provides a typical example of quantum-confined systems having discrete atomic-like states and NC dependent energy gap. Many accurate theoretical treatments have been used to investigate the electronic and optical properties of spherical InAs quantum dots. (a) Based on the continuum-like **k·p** method, it was found that the observed ground state transition is identified as the optically allowed transition between VBM and CBM. (b) Instead, the TB model has proved that the transition from VBM to CBM is optically forbidden due to the different symmetry of the wave function. (c) EPM was previously applied by Williamson and Zunger [122] and they found an inversion of the order of the upper-most valence band states compared with the present study.

simple physical picture in terms of the atomic orbitals and it has proved to be highly successful. However, the correct fitting of the band structure sometimes proved difficult in the past for the TB approach [123], which also lacks detailed information about the atomic features of the wave functions. Niquet *et al.* [119] applied this model to study single-particle tunnelling in InAs NCs. Their calculated band-gap energy and the splitting between the two lowermost conduction band states were in good agreement with the scanning tunnelling microscopy (STM) data of Ref.[2]. However, the calculated splittings between the two uppermost valence band levels were much lower than the experimental values obtained for negative bias and assigned [2] to the transition between VBM and VBM-1. The authors [119] attributed this disagreement to the complexity of the structure of the STM charging peaks and questioned the simple interpretation given in Ref.[2] in terms of pure single-hole tunnelling, pointing out that the model used by Banin and co-workers [2] could not account for the multiplicity and splitting of the negative bias peaks.

By using a different TB parametrisation Lee *et al.* [5] found a better agreement between their calculated hole addition energy spacings and the STM measurements. However the agreement between their calculated position for the three strongest absorption peaks as a function of NC size and the experimental data was less than ideal, especially for $R < 20$ Å.

No theoretical work has so far been published on the analysis and interpretation of the recent photoinduced absorption (PIA) measurements carried out by Krapf *et al.* [116].

In this chapter we apply the semiempirical pseudopotential method (EPM) [98], to study intra- and inter-band optical transitions in InAs NCs with radii ranging from 15 to 30 Å. This approach, which uses a superposition of non-self-consistent screened atomic

pseudopotentials to represent the total potential of a system, is ideally suited for a comprehensive microscopic description of a nanostructure. It provides a detailed description of the carrier wave functions on the atomic scale, but may require a larger set of basis states compared to the TB method. This method was previously applied by Williamson and Zunger [122] to investigate the electron-hole excitations in InAs NCs. However, unlike in the present chapter where pseudo-hydrogen atoms [93] (ligand potentials) are used to saturate the dangling bonds on the NC surface with an "atom by atom" passivation procedure as discussed earlier in chapter 2, in Ref.[122] an "effective medium" passivation was used, where the NCs were embedded in two different artificial barrier materials, one for valence band calculations and one for the conduction band. This choice resulted in an inversion of the order of the uppermost valence band states compared with the present study and in overestimates of the strength of some high-energy transitions, compared with experiment. Furthermore the calculations of Ref.[122] found no counterpart for the weakly observed fourth peak and their agreement with experiment was generally not as good as it is found here. Compared to Ref.[122] , moreover, we use a slightly improved InAs pseudopotential [124]. We obtain a good agreement with the observed absorption spectra in both inter- and intra-band transitions. Our results confirm the suitability of our method for describing the origin of the optical transitions in a wide range of nanocrystal sizes, from very small NCs, where $\mathbf{k}\cdot\mathbf{p}$ and TB methods break down, to large systems.

This chapter is organised as follows. In Sec. 3.1, we give a brief review of the experimental and theoretical investigations of electronic and optical features in InAs NCs. In Sec. 3.2, the single-particle states are presented. In Sec. 3.3, the interpretation of the optical transitions in InAs nanocrystals is discussed. Our calculated results are compared with three complementary experiments : (i) scanning tunnelling microscopic (STM); (ii)

photoinduced absorption (PIA), and (iii) photoluminescence excitation (PLE). Sec. 3.4 contains a summary of this chapter.

3.2 Electronic structure

3.2.1 Single-particle states

Using the Hamiltonian described in the previous chapter, the electron and hole energy levels and wavefunctions were calculated for InAs spherical dots with the effective radii R = 14.6, 20, 21.7, 24.1, 25.8, 27.7 and 30 Å. In Fig. 3.2 we show the density of states (DOS) for the uppermost 40 states in the valence band and lowermost 10 states in the conduction band calculated for 3 representative NC sizes (the energies are relative to the VBM). The single-particle band gap exhibits the expected confinement-induced size dependence. Figure 3.3 shows the cross-sectional contour plots of the wave functions squared of the four uppermost (lowermost) valence (conduction) states on a (001) cut-plane across the centre of the spherical quantum dot with R =14.6 Å together with those relative to an elongated dot (rod) with the same small radius and an aspect ratio of length over diameter L/D =1.4. The single particle levels in the conduction and valence bands are labelled as p_n, where $p = e, h$ is the charge carrier and n is the order of the level (increasing from 1 starting from CBM upwards for e and from the VBM downwards for h). We find that for spherical quantum dots, the envelope functions of the first four electron states e_1-e_4 have mostly s, p, p and p angular momentum component, respectively, whereas the first two degenerate hole states h_1 and h_2, which have previously been identified as having prevalently s-symmetry on the basis of $\mathbf{k}\cdot\mathbf{p}$ calculations [2] , have mostly p-like character and the next two degenerate states h_3 and h_4 s-like character, in agreement with TB results [5]. In Ref. [2] the lowest CB level

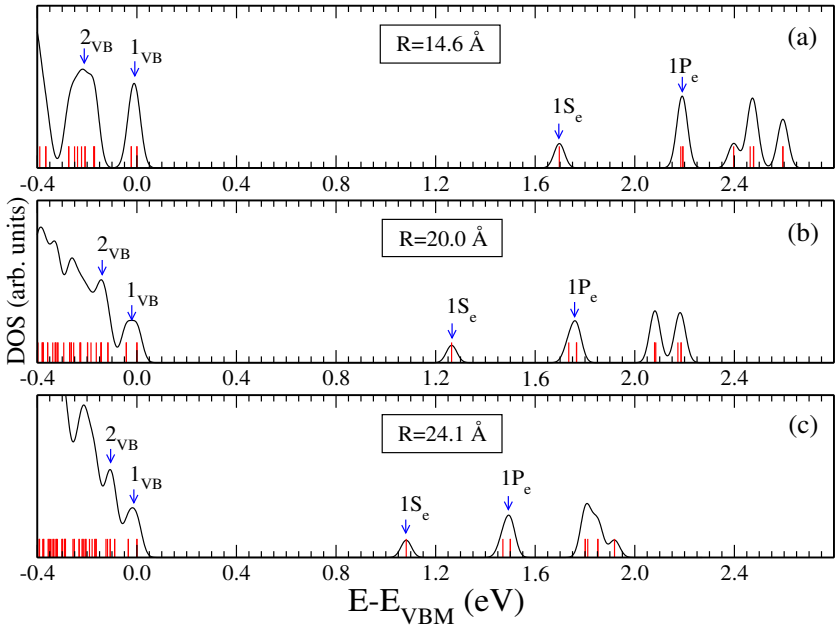

FIGURE 3.2: Density of states (DOS) calculated for three InAs NCs with R =14.6, 20 and 24.1 Å using a broadening of 30 meV. The 40 (10) uppermost (lowermost) states in the valence (conduction) band are included. The arrows indicate the positions of the DOS peaks which could correspond to the state assignment made in Ref. [2] (labels on the peaks).

$1S_e$ was found to be twofold degenerate and the next CB level $1P_e$ sixfold degenerate. According to our calculations, spin-orbit coupling splits the sixfold degenerate p-like state into one twofold (e_2) and one fourfold (e_3 and e_4) degenerate states (and the same is true for the higher Np states). Indeed, by setting $V_{SO} = 0$, we recover the sixfold degeneracy for all the p states. In the valence band, the two highest levels 1_{VB} (h_1, h_2) and 2_{VB} (h_3, h_4) are fourfold degenerate.

In contrast to the order of the envelope functions of the spherical dot just described, we find a switching of levels in the valence band of elongated dots, where the first two hole states h_1 and h_2 have mostly s-like character whereas both h_3 and h_4 have prevalently p-like character. This effect can be explained in terms of reduced confinement. The bulk exciton Bohr radius (a_0) is a useful ruler for distinguishing between different quantum confinement regimes [125, 126]. A strong confinement occurs once a critical dimension

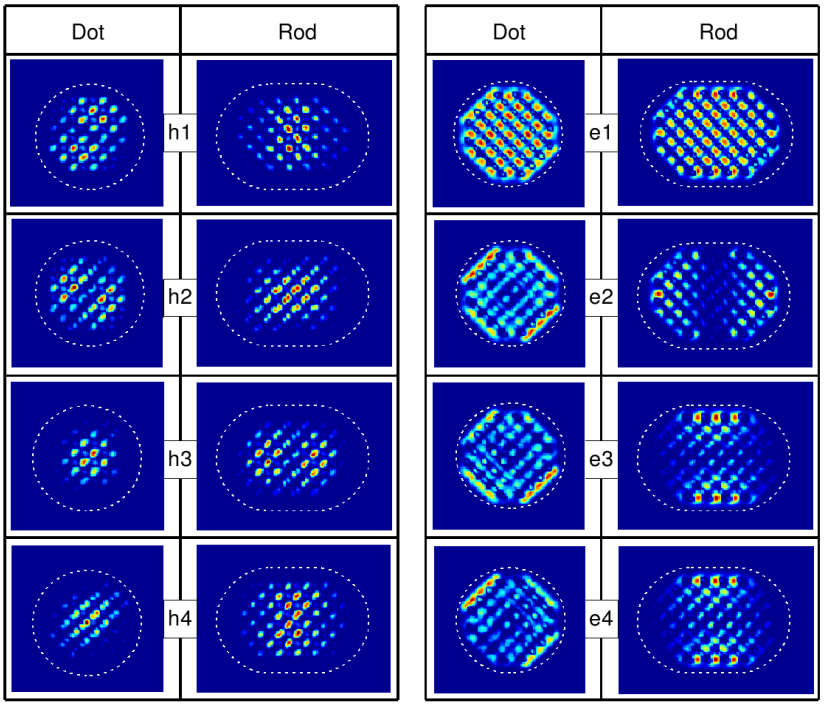

FIGURE 3.3: Comparison between the charge densities of the four uppermost (lowermost) states in the valence (conduction) band in InAs NCs with small radii of 14.6 Å and aspect ratio L/D =1 (Dot) and 1.4 (Rod).The cross-section contours are plotted on the (001) atomic plane with their intensity increasing from blue to red. The NC boundaries are represented by dashed lines.

(d) of a semiconductor nanostructure is smaller than a_0, whereas a weak confinement is defined for cases where $d \gg a_0$. Significant length dependent effects in slightly elongated dots are to be expected due to the large exciton Bohr radius in InAs nanocrystals (35 nm). We find [30] that the switching of the hole levels is both shape and size dependent, due to the interplay between quantum confinement and spin orbit coupling, as previously observed [5, 126, 127] : the value of the aspect ratio at which s- and p-like hole levels cross increases fast with NC size from 1.4 for R =14.6 Å almost doubling to about 2.6 for the next size considered, R =20 Å. Therefore, the size and shape distribution should be carefully considered in the interpretation of experimental data.

The first detailed investigation on the electronic states in InAs nanocrystals was performed by Banin *et al.* [2]. They used a colloidal technique to prepare InAs QDs that

were nearly spherically shaped with radii ranging from 10 to 40 Å and performed scanning tunnelling spectroscopy to identify the electronic states. Based on the correlation between the results of the latter and optical data [4], they concluded that: (i) the difference between the first two *groups* of STM peaks measured in the negative (positive) bias regime corresponded to the energy spacing between VBM and VBM-1 (CBM and CBM+1); (ii) the top-most valence band (1_{VB}) had mixed s and p character, with prevalent s symmetry. It was not clear at that time whether there was an intrinsic mixing or degeneracy between different states having s and p character [2] . Our results show that the mixing (ii) is intrinsic (also see below) and that the hole states with (prevalent) s-like symmetry (the degenerate h_3, h_4 levels) are well separated in energy from those with (prevalent) p symmetry (the degenerate h_1, h_2 levels). In principle, the different ordering of the hole levels assumed in Ref.[2] could, however, have been due to the shape distribution in the experiment. It is plausible that the shape of the actual synthesised samples might not have been an ideal sphere. As discussed earlier, a slight elongation would have resulted in the switching of hole energy levels near the valence band maximum for small NC sizes. The asymmetry associated with the underlying local Bloch states plays a significant role especially in small InAs structures, where it could yield a different type of energy sublevel hierarchy, particularly in the valence band, as previously found also in the $\mathbf{k}\cdot\mathbf{p}$ calculations of Efros and Rosen [117]. However our results show [30] that the absorption spectrum of a rod with $R > 14.6$ Å and with an aspect ratio large enough to exhibit an s-like VBM is substantially different from that of a dot and, most importantly, from the spectra measured experimentally in Ref. [4]. We can therefore reject the hypothesis of an elongation in the experimental sample of such an extent as to cause the assumed inversion of symmetry in the uppermost valence band states.

Previous pseudopotential calculations by Williamson and Zunger [122] also found a

strongly mixed character, in terms of the angular momentum components of the envelope functions, for the uppermost valence band states in spherical NCs, but with a different proportion of s and p contributions compared to our results, yielding a prevalently s-like VBM in the size range considered ($12 \lesssim R \lesssim 21$ Å). In what follows we discuss the possible reasons for this disagreement. The ordering of electron and hole levels in *spherical* NCs is affected by different factors: (a) the dot size, (b) the strength of the spin-orbit (and both inter- and intra-band) coupling, (c) the nature of the barrier that confines the carriers within the NC. In InAs NCs the level hierarchy has been shown [5, 122] to depend on the dot size (a), due to the interplay between spin-orbit coupling (b) and quantum confinement, and to the different size scaling of the latter for different states. Strong couplings between heavy-hole, light-hole and split-off bands, as well as between conduction and valence bands, have also been reported [5, 122] to contribute to the complexity of the single-particle level structure, particularly in the valence band, in InAs NCs. The effect of different choices for the value of the confining potentials (infinite vs finite band offsets) has been well investigated in the literature [128] and has been shown to result, among other consequences, in large energy shifts and level crossings between single-particle states with different symmetries. As discussed by Reboredo and Zunger [129] however, the physical nature of the barrier can influence the symmetry of the dot levels as well, without appreciably altering the excitonic transition energy. Furthermore, Singh and Kumar [130] recently showed that the mismatch of the value of the effective masses between barrier and dot material can have large effects on the NC energy levels, as a consequence of the BenDaniel-Duke boundary conditions [131]. The main difference between the calculations of Ref.[122] and the present chapter is precisely in the nature of the potential barrier (c). To simulate the effect of the organic ligands employed in experimental samples, here we use an "atom-by-atom" passivation, achieved with hydrogenic-like potentials. In contrast, in Ref.[122] the same effect was

obtained by passivating the NC surface using an "effective medium", i.e., an artificial barrier material represented by an atomic pseudopotential fitted to have (1) a larger band gap than InAs and (2) which produced a type I band alignment between dot and barrier. Such a barrier material however had also a set of effective masses associated with it, which was different from that of the dot. We believe that the value of this mass mismatch and the choice of the potential offset, combined with the small energy separation between the p and s hole states (of the order of few tens of meV), played the main role in determining the different valence band level hierarchy found in Ref.[122]. It is important to stress that the two approaches model different *physical* barrier materials: for a realistic choice of the effective masses in the artificial barrier the approach used in Ref.[122] is perhaps better suited for core/shell structures (where the dot is surrounded by a another semiconductor material), whereas the method used here is also applicable to organic-ligands-terminated NCs.

As mentioned above, the simple interpretation (i) of Ref.[2], in terms of pure single-hole tunnelling in the attribution of the STM peaks for negative bias, has been previously questioned by Niquet *et al.* [119] , who found a significative disagreement between their calculated energy spacing between the topmost two VB levels and the experimental data, and at the same time a good agreement for the same quantities in the CB (for $R > 20$ Å). A similar disagreement is found here, with the VBM-(VBM-1) spacing ranging from 20 to 40 meV for the NC sizes considered here. However, if we assume that quasi-particle polarisation self-energies are similar for different electron states [132] , we can compare the STM data with the spacings between our calculated DOS peaks. As it can be seen from Fig. 3.2, such spacings do not correspond to those between the two uppermost VB states but involve deeper hole levels. Our calculated DOS peak spacings are compared with those measured by STM in Fig. 3.4. From the fairly good agreement between theory and experiment, we conclude that (i) considering level-independent polarisation

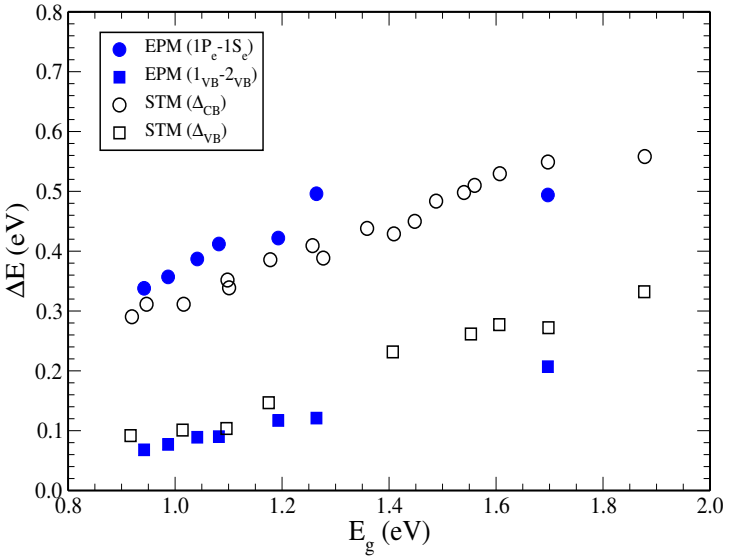

FIGURE 3.4: Comparison of the energy spacings between our calculated DOS peaks (blue solid symbols - for labelling see Fig. 4.2) and the measured STM (groups of) peaks (empty symbols, digitally extracted from Fig. 3b in Ref.[2]), as a function of the single-particle energy gap.

self-energies is a reasonable approximation in InAs NCs, and (ii) the STM data relative to negative bias measurements cannot be simply explained in terms of the energy separation between the two uppermost VB levels.

Motivated by the close agreement between STM, PLE and PIA experimental data found in Ref.[3] we therefore carried out a study of inter- and intra-band optical transitions in InAs NCs.

3.3 Optical properties

3.3.1 Intraband transitions

Figures 3.5 (a) and (c) show, respectively, our calculated conduction and valence band (single-particle) energy levels for a 24.12-Å-radius dot. The corresponding (excitonic)

intraband absorption spectrum at room temperature, broadened with a Gaussian of widths $\Gamma = 5$ and 50 meV, is shown in Fig. 3.5 (b).

The small broadening allows all the transitions to be resolved, however, as such a resolution is not yet accessible experimentally, we also use a larger value for Γ (estimated from the spectra reported in Ref.[3] for the same dot size), for a direct comparison with the observed features in the PIA spectra. The spectrum calculated with the largest broadening displays two well-defined absorption peaks: β (at 0.12 eV) and α (at 0.42 eV), each of which contains a group of smaller peaks that represent its "fine structure". These high-resolution peaks provide useful information for the interpretation of the observed temperature behaviour. We have identified one group (β) to be related to

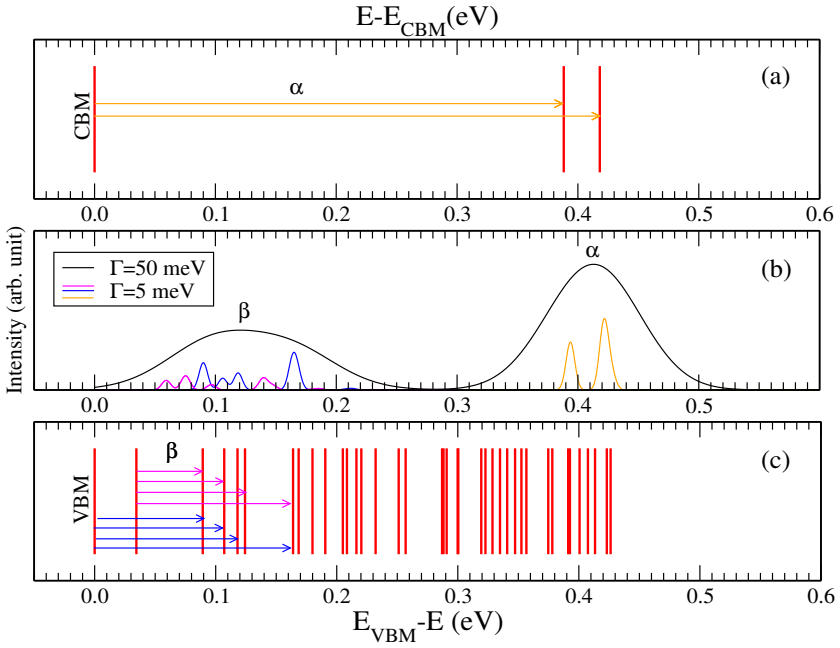

FIGURE 3.5: Calculated intraband transitions for InAs NCs with R =24.1 Å. (a) and (c) illustrate the intraband conduction-to-conduction (C-C) and valence-to-valence (V-V) single-particle transitions, respectively; (b) the calculated intraband (excitonic) absorption spectrum at room temperature with two different broadening lines (Γ=5 and 50 meV). For Γ=5 meV, the group of peaks β is decomposed into the different contributions from the two uppermost valence band states: the features relative to transitions originating from the VBM (VBM-1) are marked with a blue (magenta) line in (b), according to the colour code of the corresponding arrows in panel (c).

inter-valence transitions while the other (α) is related to inter-conduction transitions. This feature agrees very well with the experimental results from photoinduced absorption spectroscopy [3] . However, although we agree with the assignment of the high energy feature proposed by Krapf *et al.* [3], our interpretation of the origins of the intra-valence transitions differs from that suggested in Ref.[3].

The PIA measurements performed by Krapf *et al.* [3] have evidenced two groups of intersublevel (ISL) transitions in colloidal InAs QDs. The first group, relative to conduction ISL (CISL) transitions, persists at all temperatures while the second group, relative to valence ISL (VISL) transitions, is thermally activated and appears at temperature above 100 K. The CISL feature was assigned to the $1S^e_{1/2} \rightarrow 1P^e_{3/2}$ ISL transition, between the ground sublevel for the conduction electron, and the first electron excited state. Our results confirm this level assignment, with the difference that, as mentioned before, in our calculations the $1p$ electron level is not sixfold degenerate but split by spin-orbit coupling into a lowermost 2-fold degenerate state e_2 and an uppermost 4-fold degenerate state e_3, both of which contribute to the ISL absorption from the electron ground state.

Krapf *et al.* [3] interpreted the observed VISL peak using a simple three-level system model with $|1h\rangle$, $|2h\rangle$ and $|3h\rangle$ denoting the ground, first and second excited hole states, respectively. They concluded that the observed VISL transition was related to the $|2h\rangle \rightarrow |3h\rangle$ transition, corresponding to $1P^h_{3/2} \rightarrow 2S^h_{3/2}$, in $\mathbf{k}\cdot\mathbf{p}$ language. The transition $|1h\rangle \rightarrow |2h\rangle$ was explained in terms of thermal population, whereas the direct $|1h\rangle \rightarrow |3h\rangle$ transition was considered to be optically forbidden, corresponding to $1S^h_{3/2} \rightarrow 2S^h_{3/2}$.

In contrast to this simple picture, we find that the first feature (β) is composed of two overlapping groups of intraband absorption peaks (marked with blue and magenta lines in Fig. 3.5(b)), each arising from transitions originating from one of the two topmost 4-fold degenerate levels in the VB (VBM and VBM-1). Most importantly, both groups

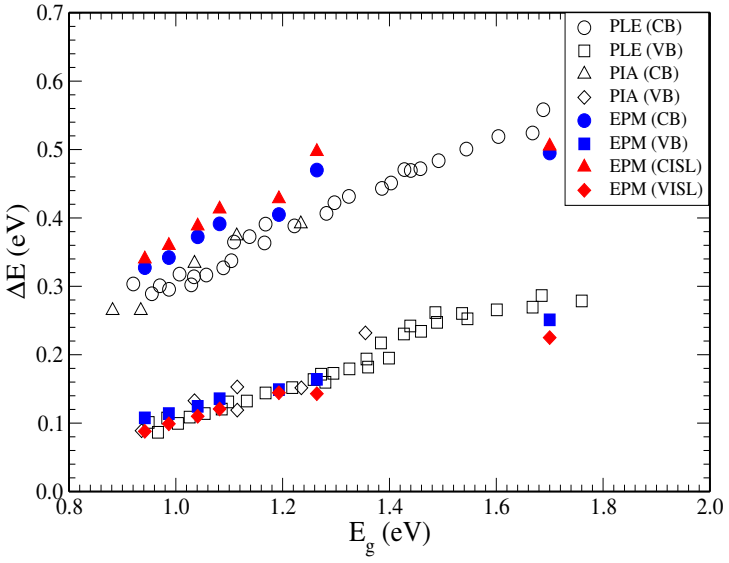

FIGURE 3.6: Comparison of our calculated intraband transition energies (red solid symbols) and interband E5-E1 and E3-E1 energy spacings (blue solid symbols) with the valence and conduction inter-sublevel transition energies measured by PIA (empty diamonds and triangles, digitally extracted from Fig. 2 in Ref.[3]) and PLE (empty circles and squares, digitally extracted from Fig. 3b in Ref.[2]) , see text, plotted as a function of the single-particle energy gap E_g (the same as in Fig. 3.4). The energies E1, E3 and E5 refer to the positions of the strongest peaks measured in absorption and are defined in Fig. 3.7 (and relative text) in the next section.

of peaks would be visible at low temperature, albeit with different intensities. (As a matter of fact, as shown in Fig. 3.5 (c), the spectral features relative to transitions from the VBM are stronger than those arising from transitions originating from the VBM-1 state). Furthermore, as illustrated by the arrows in Fig. 3.5 (c), the VISL transitions do not simply connect these two states to a single higher-energy hole state ($|3h\rangle$ in Ref.[3]), but involve multiple higher excited hole levels. The fact that we predict transitions that originate from levels with different *prevalent* character (p and s for VBM and VBM-1 respectively) and end on the same final state (VBM-2, for example) is due to the intrinsic mixing of the envelope functions in terms of their angular momentum components: as it can be clearly seen from Fig. 3.5 (c), the transition VBM $\rightarrow$ VBM-2 is much stronger than VBM-1 $\rightarrow$ VBM-2, due to the similarity of the symmetry between the VBM and VBM-2 states.

Our calculated VISL transition energies are compared with PIA (and PLE) data in Fig. 3.6. From the excellent agreement obtained we draw the following conclusions: (i) the three-levels model used in Ref.[3] , is inadequate to capture the complexity of intra-band absorption in InAs NCs; (ii) the thermal activation effect observed experimentally, where the lowest energy PIA feature (attributed to VISL transitions) appeared above a temperature of 100K, cannot be explained in terms of the thermal population of the VBM-1 ($|2h\rangle$) from a VBM state ($|1h\rangle$) optically inaccessible from the VBM-2 ($|3h\rangle$) level.

(i) Our model provides a more satisfactory interpretation of the PIA data because it is able to accurately describe the complex structure of the valence band of bulk InAs [124] , including the highly anisotropic heavy-hole effective masses and the strong spin-orbit coupling. In the light of our results, the alternative hypothesis of a thermally-activated VISL transition due to the presence of a shallow surface-localised state (as opposed to a thermal population process between dot-interior states), advanced in Ref.[3], seems a more likely explanation of the temperature dependence (ii) observed in the PIA experiments.

To obtain further confirmation of our interpretation of the observed optical features we next calculated the interband absorption spectra.

3.3.2 Interband transitions

Figure 3.7 displays our calculated interband V-C absorption spectrum relative to a 24 Å-radius NC and the corresponding transitions between single-particle energy levels, which represent the main contribution ($\geq 99\%$) to the different excitonic peaks. Using a line broadening of Γ =10 meV, we resolve several peaks each of which is associated with transitions having large oscillator strengths. To compare with PLE experiments [4] , we

employ a line broadening of Γ=30 meV, whose effect is to wash out some of the weaker peaks, such as the β peak (peak E2 in the PLE experiment) and to merge other peaks, such as κ and λ into one single, broader feature (peak E4 in the PLE experiment). We therefore resolve three strong peaks α, γ and π (corresponding to E1, E3, E5 in Ref.[4]), with weaker features in between, in agreement with what observed experimentally [4].

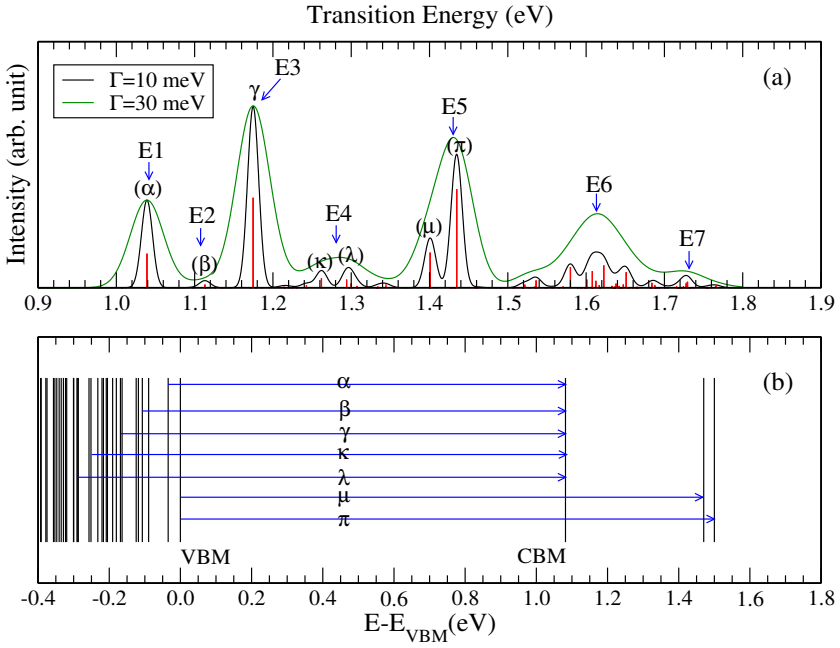

FIGURE 3.7: (a) Interband valence-to-conduction (V-C) absorption spectrum for an InAs nanocrystal with R =24.1 Å calculated with linewidths Γ=0 (red line), 10 (black line) and 30 meV (green line). The corresponding transitions between single-particle energy levels are shown in (b), with arrows. The lowest allowed transition (α) is the transition from VBM-1 to CBM.

A careful analysis of our results shows that :

(a) **Peak E1** corresponds to a transition with a strong intensity. In our calculation, the initial valence state associated with this transition is the second hole state (h_2 =VBM-1) with mostly s-like character and the final conduction state is the electron ground state which has s-like character (see also Table 3.1). It is interesting to note that our calculated transition between the ground hole state (h_1 =VBM) and the ground electron state ($h_1 \rightarrow e_1$) has an oscillator strength which is typically about 2 orders of magnitude

smaller than that between h_2 and e_1 and therefore cannot be observed. This finding is in accordance with the results of tight-binding calculations [5, 90] but not with the **k·p** approach of Ref.[4].

(b) **Peak E2** relates to a transition with such a weak intensity that it cannot be observed for all dot sizes in the PLE experiment. In our calculation this peak corresponds to the transition $h_4 \rightarrow e_1$ (a weak peak β in Figure 3.7). Interestingly this feature was not predicted in the **k·p** approach of Ref.[4].

(c) **Peak E3** has a strong intensity. The initial valence state associated with this peak is a 4-fold degenerate hole state (h_7) and the final conduction state is the doubly degenerate, lowest energy electron state (e_1). In the **k·p** calculation, this is the $2S_{3/2} \rightarrow 1S_{1/2}$ transition and the $h_5 \rightarrow e_1$ (B2) transition in the tight-binding method.

(d) **Peak E4** results from the merging of peak κ and λ in Figure 3.7 and has a weak intensity in good agreement with the weakly observed E4 in the PLE measurement. The initial single-particle states of these transitions are in the deeper levels in the valence band and the final state is the ground electron state (e_1). This corresponds to the $h_{16} \rightarrow e_1$ and $h_{19} \rightarrow e_1$ transitions in our calculation. This peak found no counterpart in either the **k·p** calculation of Ref.[4] or the EPM method of Ref.[122].

(e) **Peak E5** is a very intense peak that is observed in all dot sizes. It relates to the transitions μ and π corresponding to $h_1 \rightarrow e_2$ and $h_1 \rightarrow e_3$. The initial state is the same for both transitions and has prevalently p-like character and both final states have mostly p-like character. In the **k·p** approach, these transitions are closest to the transitions $1P_{3/2} \rightarrow 1P_{3/2}$ and $1P_{3/2} \rightarrow 1P_{1/2}$. In the tight-binding method, this peak is assigned to the $h_1 \rightarrow e_2$ (B3) transition, where e_2 is sixfold degenerate.

TABLE 3.1: Comparison of the assignment of the first 5 peaks in the PLE measurement [4] according to the current empirical pseudopotential method (EPM), the tight-binding and the **k·p** approaches. For the EPM calculation, the subscripts denote the order of different single particle electron and hole energy levels (excluding degeneracy), whereas the numbers in the upper parenthesis denote the order of single-particle energy states including degeneracy (i.e., the first 2-fold degenerate hole level is $h_1^{(1,2)}$, the next $h_2^{(3,4)}$, and so on). In the tight-binding method, the level e_1 and e_2 are the first (twofold) and the second (sixfold) lowest electron levels, whereas the level h_1 and h_2 are the first (fourfold) and the second (fourfold) lowest hole levels. The degeneracy mentioned in the T-B approach includes spin as well. The first three strongest bright excitons in the tight-binding method are labelled as B1, B2 and B3. However, although other weaker peaks have been predicted to occur in Ref.[5] , they have not been assigned to specific transitions. The notation for the electron and hole states in **k·p** method is nQ_F, where n is the main quantum number, Q=S,P,D, ..., denotes the lowest angular momentum (L) in the envelope function and F is its total angular momentum. The second and fourth peak have not been predicted in the approach of Ref [4].

Peak	EPM	Tight-binding	**k·p**
E1	$h_2^{(3,4)} \rightarrow e_1^{(1)}$	$h_2 \rightarrow e_1$ (B1)	$1S_{3/2} \rightarrow 1S_{1/2}$
E2	$h_4^{(7,8)} \rightarrow e_1^{(1)}$	Not assigned	Not predicted
E3	$h_7^{(11,12)} \rightarrow e_1^{(1)}$	$h_5 \rightarrow e_1$ (B2)	$2S_{3/2} \rightarrow 1S_{1/2}$
E4	$h_{16}^{(25,26)} \rightarrow e_1^{(1)}$, $h_{19}^{(30)} \rightarrow e_1^{(1)}$	Not assigned	Not predicted
E5	$h_1^{(1,2)} \rightarrow e_2^{(2)}$, $h_1^{(1,2)} \rightarrow e_3^{(3,4)}$	$h_1 \rightarrow e_2$ (B3)	$1P_{3/2} \rightarrow 1P_{3/2}$, $1P_{3/2} \rightarrow 1P_{1/2}$

By using 80 states in the valence band and 8 in the conduction band, we calculate more than 7 absorption peaks. However, as it can be seen from the multiple features below peak E6 in Fig. 3.7, the assignment of the highest of them in terms of single particle transitions becomes increasingly complicated due to the large number of states involved. We compare our results with the experimental data [4] in Fig. 3.8.

Due to the fact that precise experimental size determinations are relatively difficult, a more compelling comparison with the PLE data emerges when the energies of higher transitions are plotted relative to the first bright-exciton energy (E1). However, as often the determination of the position of a peak and/or its experimental "visibility" are not

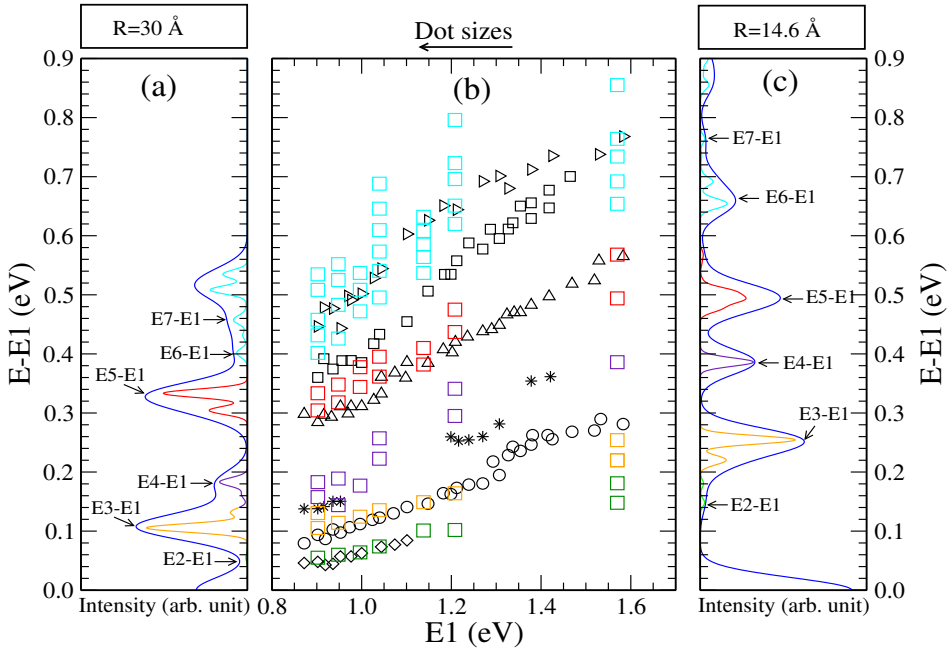

FIGURE 3.8: Calculated positions of the optical absorption features, relative to the first strong absorption peak (E1), in InAs NCs with radii ranging from 14.6 to 30 Å. Panels (a) and (c) display the absorption spectra relative to E1 for the largest and smallest NCs, respectively, with linewidths Γ of 10 (ideal, coloured line) and 30 meV (experimental-like, blue line): peaks with Γ=10 meV contributing to the same broad peak with Γ=30 meV have the same colour. (b) Positions of all the absorption peaks calculated with Γ=10 meV (squares) relative to the first bright exciton (E1) versus E1 for InAs quantum dots with effective radii of 14.6, 20, 21.7, 24.1, 25.8, 27.7 and 30 Å, compared with PLE data (black symbols, digitally extracted from Fig. 4 in Ref.[4]). The colour coding corresponds to that used in panels (a) and (c).

trivial, we decided to show in Fig. 3.8 (b) all peaks resolved using the smaller line broadening (Γ=10 meV), colour coded corresponding to the broader peaks (Γ=30 meV) they contribute to. As a guide to the reader, the absorption peaks corresponding to the largest and smallest NC size studied in this chapter (using both a large, experimental-like broadening and a small, ideal broadening) are also illustrated in Fig. 3.8 (a) and (c), and colour coded to identify the corresponding features in (b).

We find very good agreement with experiment for the spacings between the first four peaks and the band edge exciton (E2-E1, E3-E1 and E4-E1) down to the smallest NC size (14.6 Å radius). This result is especially remarkable considering that some of these

transitions are either not predicted at all [4, 122] or have not been assigned [5] in previous theoretical studies. Since, as described above (see also Fig. 3.7), peaks 1 to 4 originate from transitions between different hole states and the electron ground state e_1, these results, together with the good agreement already found with the observed VISL transitions [3], confirm the suitability of our model for the description of the valence band structure and the band gap energy in InAs NCs within a wide size range. The agreement obtained with the position of the fifth and sixth peaks is less ideal and reflects the slight overestimate of the level spacing in the conduction band we found for CISL transitions. The position of peak 7 is again in good agreement with observation.

Figure 3.9 shows the comparison of the exciton energies of the first three strongest absorption peaks, relative to the energy of the band edge exciton, between the present

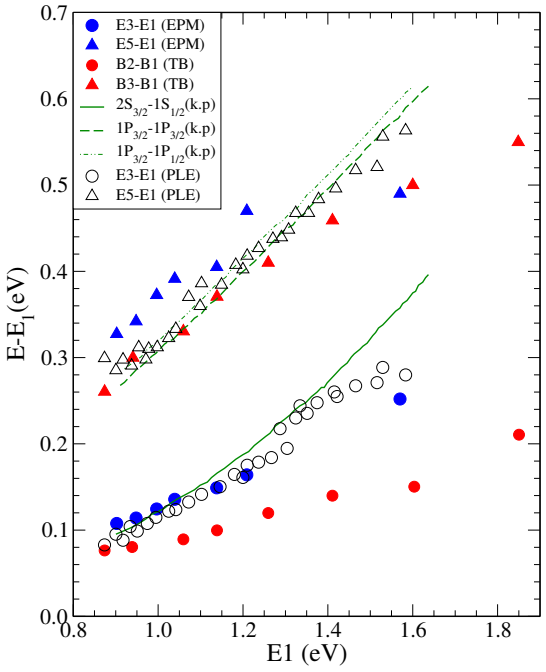

FIGURE 3.9: First three strong-exciton energies relative to the lowest bright-exciton energy plotted with respect to the lowest bright exciton position. In addition to the comparison with PLE data (digitally extracted from Fig. 4 in Ref.[4]) , our results are compared with the results of the tight-binding method [5] as well as the multiband effective mass model [4].

model and the other theoretical frameworks (**k·p** calculations [4] and the tight-binding method [5]). A comparison of their assignment in terms of single-particle transitions according to our empirical pseudopotential calculation and the other theoretical methods is shown in Table 3.1.

The energy spacing E3-E1 calculated with our approach shows a better agreement with experiment than the results of both **k·p** [4] and tight-binding [5] calculations. This supports our claim that our model provides an accurate description of the complex structure of the valence band, correctly accounting for the anisotropy of the heavy-hole effective masses [124] and the strong coupling among heavy-hole, light-hole and spin-split bands, which play an important role in determining the overall single-particle level spectrum. Surprisingly, however, the **k·p** and tight-binding methods provide a better description of the electron levels in the less complex conduction band, as illustrated by the comparison with the PLE data for the energy spacing E5-E1 reported in Fig. 3.9. A possible reason for this can be found in the "fine structure" of our calculated peaks: as shown in Fig. 3.7 our fifth peak is actually composed of two peaks μ and π, relative to transitions from the VBM to the two spin-orbit split p-like electronic states e_2 and e_3, respectively. In our calculations the second of those peaks (π) is the strongest and therefore the position of E5 is blue-shifted towards it. If peak μ were the strongest, the position of E5 could shift to the red by as much as the e_2-e_3 splitting, which is of the order of a few meV for the smallest NC considered here, increasing to a few tens of meV depending on the NC size. This would bring our results in closer agreement with experiment, as it is the case for the 14.6 Å-radius NC, where such splitting is small. A similar argument applies to our calculated PIA spectra. In contrast, in neither **k·p** nor tight-binding approaches the p-like electron state is split and therefore their calculated E5-E1 energy separation is not affected by the magnitude of this splitting.

Another explanation could be provided by the shape of the experimental samples: elongated NCs exhibit substantially smaller spacings between s and p levels in the conduction band without showing significant decreases in the separation between the same states in the valence band, compared to spherical structures [30]. We previously excluded elongation as an explanation for the different level ordering at the top of the valence band assumed in Ref. [2], on the basis that the crossover between s and p states would require too large values of the aspect ratio, which would result in large morphological changes in the absorption spectra, incompatible with observation. However, slight elongations in the NCs resulting in aspect ratios small enough not to change appreciably the shape of the absorption spectra (nor the level hierarchy in the valence band) could account for the deviation from experiment of all our results involving the spacing between conduction band states.

3.4 Conclusions

We applied the pseudopotential method to investigate the optical properties of InAs NCs with $14.6 < R < 30$ Å. Our accurate description of the complex structure of the valence band allows us to successfully explain the low energy features observed in recent PIA measurements. Based on this result we rejected the simplistic interpretation of such features in terms of a 3-level model and the hypothesis of a thermal population process between hole states delocalized in the dot-interior advanced in Ref.[3] to explain the experimentally observed temperature dependence of the low-energy PIA feature. We also questioned, as previously done by Niquet *et al.* based on the results of TB calculations, the explanation of the results of STM experiments in the negative bias regime in terms of the energy separation between the two uppermost valence band levels

VBM and VBM-1, suggesting instead an interpretation based on the separation between the peaks in our calculated density of states.

Our calculated interband absorption spectral features reproduce those observed experimentally, showing three strong peaks (labelled as E1, E3 and E5) separated by weaker features. We achieve a good agreement for the energy position of the first 4 peaks and the seventh, down to NCs with R =14.6 Å. This result is especially remarkable considering that: (i) some of these transitions were either not predicted at all [4, 122] or were not assigned [5] in previous theoretical studies; (ii) the size range considered here includes very small NCs, i.e., a confinement regime where all other theoretical approaches break down. The agreement with the position of peaks 5 and 6 (and the, closely related, position of our calculated CISL peaks) is less ideal but still reasonable. We attribute this result either to a "fine structure" effect in the conduction band, where strong spin-orbit coupling induces a sizeable splitting in the otherwise 6-fold degenerate first excited state or to a slight elongation in the experimental samples, which would result in a decreased spacing between conduction band energy levels.

In summary, the pseudopotential method provides an accurate description of the complex energy level structure (especially in the valence band) of InAs NCs and presents itself as a suitable approach to explain many experimental features observed in both intra- and inter-band optical absorption spectra.

Motivated by the discovery of energy level crossing in the slightly elongated dot together with the precise description in the spherical structure, we next applied the same methodology to investigate the optical signature in a quasi-two-dimensional confinement structure, i.e., a slightly elongated structure, in the next chapter.

Chapter 4

Slightly Elongated Dots

In the preceding chapter, we applied the atomistic pseudopotential method to investigate the electronic and optical properties of spherical InAs nanocrystals. Our accurate description of the complex structure of the valence band successfully explains the optical feature observed in the recent PIA measurement [3] leading to a more satisfactory interpretation of the temperature dependence observed experimentally. Despite a precise description of the complex structure of the valence band, the description of the energy levels in the less complex conduction band is less satisfactory. A plausible explanation for this could be provided by the shape distribution of the experimental samples. We previously suggested in the chapter 3 that the slight elongations in the NCs with a small aspect ratio could account for the deviation from the experiment of all our calculated results involving the spacing between conduction-band states. In light of this suggestion, we will therefore extend our knowledge to investigate the effect of small elongations on the electronic and optical signatures in InAs nanocrystal quantum dots [30]. The evolution of intra- and inter-band optical absorption spectra as the NC becomes progressively elongated will also be discussed in this chapter.

4.1 Introduction

The identification of the rich absorption features observed in optical spectroscopy on nanocrystal (NC) ensembles, in terms of specific excitonic state components, is a complex issue. Many different factors contribute to the uncertainty of their assignment, size and shape distributions being the most significative. In fact, although experimentalists nowadays have always access to microscopic information (usually in the form of transmission electron microscopy (TEM) or its high-resolution version), often complemented by X-ray scattering, these methods are not completely reliable and may underestimate the actual dimensions, being insensitive to non-periodic layers at the NC surface [133]. Furthermore the TEM images only show *cross sections* on a specific plane, from which little information can be extracted on the perpendicular direction, as shown in Fig. 4.1. There is therefore always some degree of ambiguity on both size and shape of the NCs even when micrographs are supplied.

The empirical pseudopotential method (EPM) has proved highly successful in the past in interpreting the optical properties of spherical nanostructures made of different materials such as CdSe [43, 93, 114, 115], InP [43, 128, 134], PbSe [113, 135], and InAs [88, 122]. However, so far it had been applied to the investigation of *elongated* NCs made of CdSe [136–139] and InP [140] only. Here we investigate the effects of small elongations on the spectroscopic features in InAs NCs. These particles have attracted great interest as their optical properties can be tuned with size to cover the technologically important energy window between the visible and the near infrared [141], making them potentially ideally suited for applications in biology [142], electro-optics [143] and telecommunications [144]. Furthermore due to the large difference between the electron and hole effective masses in InAs, they are expected to exhibit highly efficient carrier multiplication. This process, where multiple excitons are generated upon absorption of

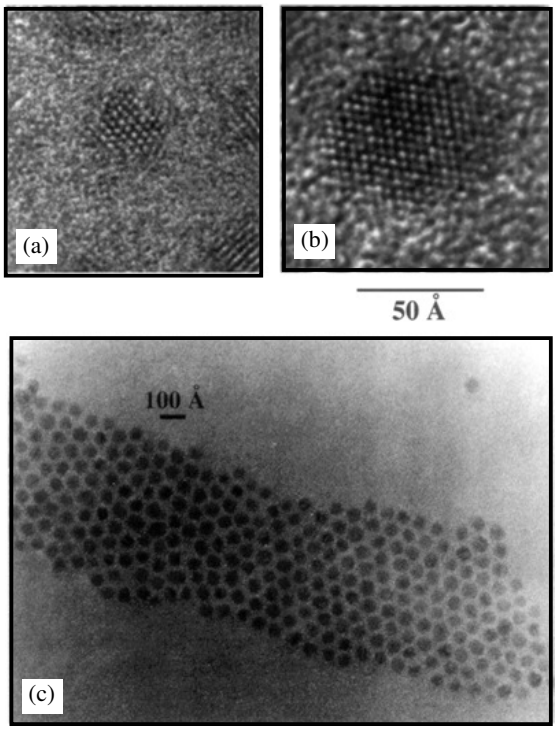

FIGURE 4.1: (a)-(b) High resolution transmission electron microscope (HRTEM) images of the "nominally" spherical InAs nanocrystals in a specific plane which are digitally copied from Ref. [6] : (a) 22 and (b) 50 Å in diameter. (c) Lower resolution of InAs nanocrystals.

a single photon [46], has important implications for the application of NCs in photovoltaics [51], as it can greatly increase the photocurrent output of the device. From this point of view, the knowledge of the NC shape is very important, as it may affect the efficiency of both carrier multiplication and carrier collection (i.e. how efficiently electrons and holes travel to the electrodes after they have been separated to generate a photocurrent).

In this chapter we show that the intra- and inter-band optical absorption spectra calculated for spherical NCs, although qualitatively similar to those relative to slightly elongated structures either with the same radius, or containing the same total number of constituent atoms, exhibit specific quantitative signatures which allow one to distinguish between the two shapes. Elongated structures are found to exhibit large red

shifts in the position of the peak associated with the intra-band transition between the two lowermost levels in the conduction band and in the energy separation between the first and the fifth peak in inter-band absorption spectra. Shifts of the same order of magnitude (hundreds of meV) are also predicted in the spacings between STM peaks measured in the positive bias regime. This information can be valuable in determining the substantial presence of even slightly elongated structures in experimental samples of nominally spherical NCs.

In the next section we will discuss the evolution of the electronic signatures from nanocrystal quantum dots to slightly elongated dots starting from the single particle density of states.

4.2 Single-particle density of states

Using the Hamiltonian described in the chapter 3, we calculated the electronic structure of InAs QDs with effective radii $R_{QD} = 14.6$, 20 (1207), 21.7 (1547) and 24.1 (2115) and 25.8 (2590) Å (where the quantities in brackets are the number of constituent atoms N_a for each NC) and QRs with radii $R_{QR} = 14.6$ and 20 Å and aspect ratios $\sigma = L/2R_{QR}$ ranging from 1 to 1.5 (with corresponding values of $1207 < N_a < 2200$ for the 20 Å rod). In Fig. 4.2 we show the density of states (DOS) for the uppermost 40 states in the valence band and lowermost 10 states in the conduction band calculated for four NCs with R =20 Å and σ =1, 1.1, 1.2 and 1.5 (the energies are relative to the valence band maximum, VBM). We see that the elongation has two main effects: (i) as σ increases, the density of states in both conduction and valence bands increases and (ii) the single-particle band gap E_g shifts to the red.

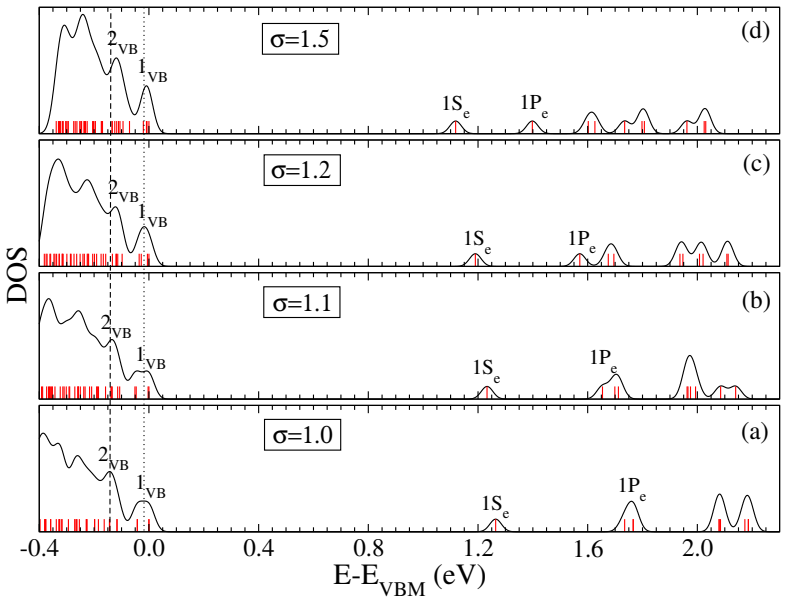

FIGURE 4.2: Calculated single particle density of states (DOS) for four InAs nanocrystals with R =20 Å and σ =1 (a), 1.1 (b), 1.2 (c) and 1.5 (d) using a broadening line allowing the comparison with the state assignment made in the STM spectra of Ref. [2] (Γ = 30 meV) . Red vertical lines represent the 40 uppermost and 10 lowermost states in the valence and conduction band, respectively.

We have questioned in the past [88] the simple interpretation of the STM peaks measured by Banin *et al.* [2] for negative bias, in terms of tunnelling between single hole states. We found, as in the case of previous tight binding calculations [119], that the spacing between the two uppermost valence band states (ranging from 20 to 40 meV for the NC sizes considered here) was too small compared to the experimental data. Based on the assumption of state-independent quasi-particle polarisation self-energies, we proposed an alternative interpretation of the STM results in terms of the spacing between the DOS peaks we calculated for InAs dots [88]. In this approximation, therefore, the calculated DOS for elongated structures shown in Fig. 4.2 could provide some insight into the nature of the experimental samples. From Fig. 4.2 we see that the spacing Δ_{CB} between the peaks labeled $1S_e$ and $1P_e$ decreases significantly with increasing σ, implying smaller values for the STM peak separations measured on elongated samples. The shift in the position of the VB peaks 1_{VB} and 2_{VB} is less dramatic (with magnitudes of the order

of 10% or less of the calculated peak spacing for a spherical NC), and is non-monotonic, their separation Δ_{VB} decreasing for $1 < \sigma \leq 1.2$ and then increasing again for more elongated structures. The expected energy shifts are 74, 114 and 216 meV (11, 15 and 11 meV) for the spacings obtained in the positive (negative) bias range with NC with σ =1.1, 1.2 and 1.5, respectively, when compared with those relative to spherical structures ($\sigma = 1$) for NCs with R =20 Å. We find a similar qualitative behaviour in the case of smaller NCs (R =14.6 Å). However in this case Δ_{CB} is almost constant up to $\sigma = 1.2$ and decreases by 120 meV for $\sigma = 1.5$, whereas the decrease of Δ_{VB} is larger (50 meV) for $\sigma = 1.2$. Our calculated values for Δ_{VB} and Δ_{CB} are compared with the STM data in Fig. 4.3. Although the agreement with the experimental data obtained in the negative bias regime (low energy curve) is good for all values of $1 \leq \sigma \leq 1.5$, the

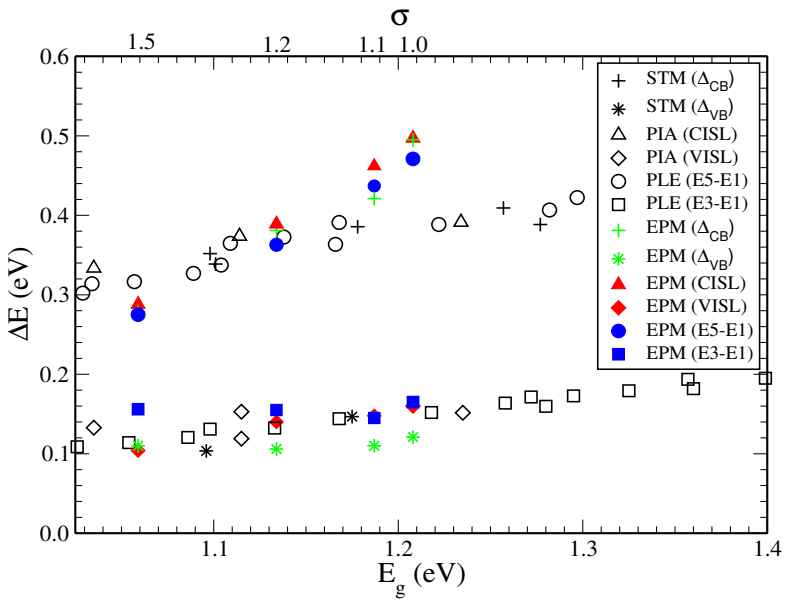

FIGURE 4.3: Comparison of the spacings between DOS peaks (green symbols), intra-band transition energies (red solid symbols) and inter-band E5-E1 and E3-E1 energy spacings (blue solid symbols) calculated with the EPM approach and the experimental STM peak separations (black crosses and stars, digitally extracted from Fig. 3b in Ref. [2]), the valence and conduction inter-sublevel transition energies measured by PIA (empty diamonds and triangles, digitally extracted from Fig. 2 in Ref. [3]) and the E5-E1 and E3-E1 separations between the measured PLE peaks (empty circles and squares, digitally extracted from Fig. 3b in Ref. [2]), see text.

comparison with the peaks spacings in the CB seems to suggest a slight elongation (with $\sigma \leq 1.2$) in the experimental samples.

4.3 Optical bandgap for quantum dots and slightly elongated dots

To further investigate this hypothesis we calculated the evolution of the energy gap from a spherical dot with R =20 Å and $\sigma = 1$ (total number of In and As atoms N_a =1207), to NC structures with N_a ∼2200, obtained by increasing either R up to 24 Å and keeping σ fixed (dots) or by increasing σ up to 1.5 and keeping R constant (rods). The results are shown in Fig. 4.4. We choose to plot E_g as a function of the total number of atoms in the NC since this quantity can often be controlled in the experiment, based on the chemistry of the synthetic process, although, as discussed above, the information on how the atoms are distributed in the NC may be more difficult to obtain. We find that rods exhibit a stronger confinement-induced effect compared with dots with the same value of N_a, as expected. This shows that the confinement in the direction perpendicular to the long axis (i.e., the smaller dimension) provides the dominant contribution to the energy shift, as it is the case in epitaxially-grown InAs islands. The value of E_g for QRs with such small aspect ratios is, however, very close to that calculated for spherical NCs with the same number of atoms, their difference remaining ≤ 20 meV for $\sigma \leq 1.5$. For small values of σ, therefore, the knowledge of E_g alone would be insufficient to determine the NC shape, even in the presence of microscopic information. With the resolution available with TEM, in fact, dots would probably be indistinguishable from rods with small aspect ratios, (especially if the latter were visualized perpendicularly to the long axis), and the radii of the dots with similar E_g ($20 < R_{QD} \lesssim 23$ Å) would be within 15%

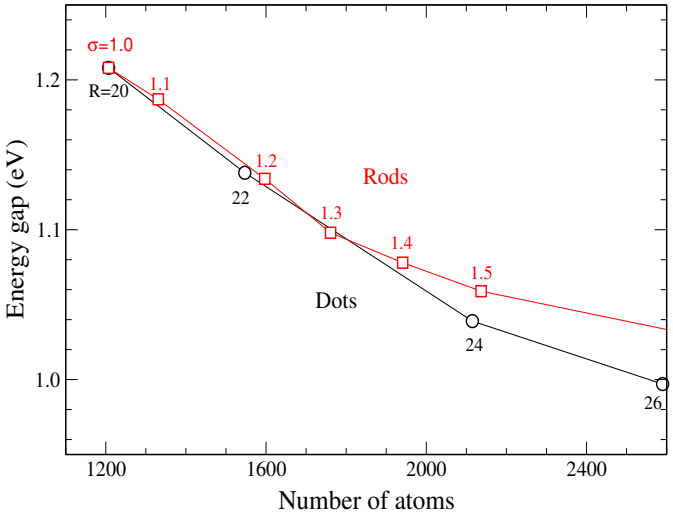

FIGURE 4.4: Comparison between the room temperature optical energy gaps calculated for spherical (black symbols) and elongated structures (red symbols) as a function of the number of atoms in the NC.

or less of those of the rods (R_{QR} =20 Å), the standard size distribution in experiments being of about 13%.

4.4 Intraband transitions

The increase in the single-particle DOS with elongation as discussed in Sec. 4.2 is also expected to affect the position of the peaks associated with inter-sublevel (ISL) transitions in the NCs. The two well separated features found by Krapf *et al.* [3] in their photoinduced absorption (PIA) spectra of InAs colloidal QDs have in fact been associated with ISL transitions between the two lowermost states in the conduction band (CISL, the high energy peak), and between the two uppermost valence states (VISL, the low energy peak). We therefore predict a similar red shift for these two PIA peaks in elongated NCs, as expected for the STM peak spacings discussed above. Our calculated intra-band absorption spectra relative to NCs with $R = 20$ Å and $1 \leq \sigma \leq 1.5$ are shown in Fig. 4.5. As σ increases both peaks exhibit progressive red shifts, as expected.

It is particularly interesting to note the shape evolution of the high energy peak where, for $\sigma = 1.2$, a broad shoulder appears on the low energy side. This feature further develops into a separate peak for larger elongations. Careful examination of the data reported in Ref.[3] reveals the presence of this shoulder also in the experimental spectra obtained for NCs with $R \leq 24$ Å. As no shoulder is found in our spectra for spherical NCs of any size, its presence could be interpreted as an indication of the substantial presence of slightly elongated structures (with $\sigma \leq 1.2$) in the experimental samples, in agreement with our earlier conclusion based on the comparison with STM data. That this might indeed be the case is also suggested by the results of the comparison between the calculated and the observed [3] position of the two intra-band absorption features, shown in Fig. 4.3. The values calculated for slightly elongated structures with $1 < \sigma \leq 1.2$ show a better agreement with experiment than those obtained for spherical NCs ($\sigma = 1$), in the case of CISL transitions. The presence of elongated NCs would therefore explain the poorer agreement with experiment found in the pseudopotential calculations for spherical NCs of Ref.[88] for all quantities related to transitions involving the first excited electron state $1P_e$ (such as the position of the CISL transition peak and the energy separation between the first and fifth peak in the interband absorption spectra), if compared to the very good agreement achieved for intra- and inter-band transitions involving all VB states up to the 1S state in the CB, whereas it would not provide more insight into the observed [3] temperature dependence of the VISL peak, as the contributions from both VBM (thin blue line in Fig.) and VBM-1 (red dashed line) would still be present at low temperature for all values of σ considered.

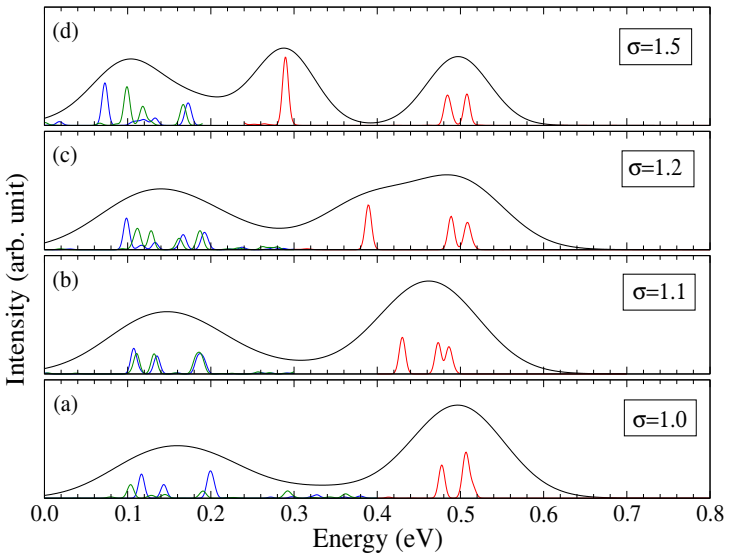

FIGURE 4.5: Optical intra-band absorption spectra calculated for InAs NCs with R =20 Å and σ =1.0 (a), 1.1 (b), 1.2 (c) and 1.5 (d) using a broadening of 75 meV (black line) and 10 meV.

4.5 Interband transitions

As shown in Sec.4.4 the specific intra-band absorption spectra might be used as an indication of the substantial presence of slightly elongated structures in the experimental samples. We therefore calculated the full inter-band absorption spectrum, looking for shape-specific signatures. Figure 4.6 shows the evolution of the optical features as the NC becomes either progressively elongated (as σ increases), keeping R constant(=20 Å), or progressively larger (as R increases), keeping σ constant (=1). We see that in all the spectra for $\sigma < 1.5$ three strong peaks can be distinguished, separated by weaker peaks, in qualitative agreement with the experimental findings of Ref. [4], whereas the spectrum calculated for a rod with $\sigma = 1.5$ presents substantial differences from that of less elongated structures. We compare the energy separation between the peaks labeled E5 and E1 and E3 and E1 in the absorption spectra of Fig. 4.6 with the corresponding quantities obtained from the experimental size selected PLE spectra measured by Banin *et al.* [4] in Fig. 4.3. Once more, in the case of transitions involving the first excited

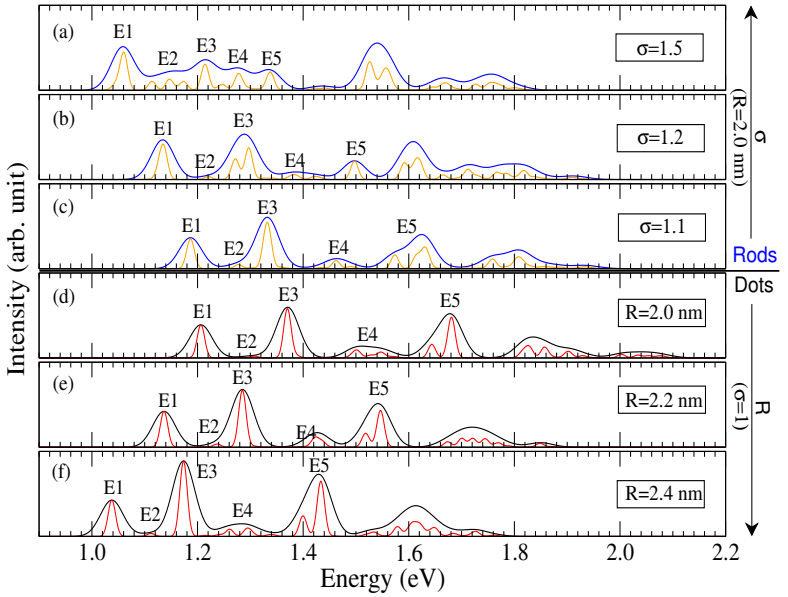

FIGURE 4.6: Optical absorption spectra calculated for InAs NCs with R =20 Å and σ =1.5 (a), 1.2 (b), 1.1 (c) and 1.0 (d) and dots (σ =1) with R =21.7 (e) and 24.1 Å(f), using a broadening of 30 meV (black and blue lines) and 10 meV (red and orange lines).

state in the conduction band, a better agreement with experiment is achieved with data calculated for elongated NCs. Taking into account of all the results presented here we can therefore draw a conclusion that the experimental samples in Ref.[2] contained a majority of slightly elongated particles, with $\sigma \leq 1.2$.

4.6 Conclusions

Using a semiempirical pseudopotential approach, we have calculated the effect of small elongations on the electronic and optical features of InAs colloidal dots. We found that although NCs with aspect ratios of length over diameter ≤ 1.2 show qualitatively similar optical spectra, spherical structures can be distinguished from elongated ones based on spectral features related to the energy separation between 1S and 1P levels in the CB, such as the shape and position of the high energy peak in PIA experiments,

the spacing between the first and the fifth peak observed in PLE measurements or the spacing between STM peaks measured in the positive bias regime. Based on the comparison of our results with STM, PIA and PLE data we concluded that the nominally spherical samples used in many experiments contained a significant fraction of slightly elongated particles. The substantial presence of the latter explains the poor agreement with experiment found in previous pseudopotential calculations, for the position of the peaks relative to CISL transitions in PIA spectra and for the magnitude of the E5-E1 separation in PLE spectra.

In this chapter we found that the small elongations play an important role in the evolution of optical signatures in InAs nanocrystal quantum dots. In the following chapter, we will use the same approach to further investigate the evolution of the optical properties, such as optical bandgap, Stoke shift, degree of linear polarisation and the radiative lifetime, in the transition from three- to quasi-two dimensional quantum confinement in InAs nanorods.

Chapter 5

InAs Nanorods

In Chapter 4 the effect of small elongation on the electronic and optical signatures was described. Here we consider those of InAs quantum rods (QRs) as a function of increasing length-to-diameter ratio. We show that, as the aspect ratio increases, energy levels cross in both conduction and valence bands. It is also found that the crossover between highest occupied molecular orbitals is found to be size-dependent and the level crossings at the top of the valence band are essential to explain the evolution with elongation of all optical properties in these systems. Their transformation from zero- to quasi-one-dimensional structures is characterised by a common monotonic behaviour of band gap, Stokes shift, degree of linear polarisation, and the radiative lifetime, closely linked to the variation with aspect ratio of the electronic structure of nanocrystal band edge.

5.1 The importance of nanorods

Semiconductor nanocrystals (NCs) have been the subject of intensive experimental and theoretical studies during the past decade because of the variety of quantum-confinement-induced effects they exhibit [145]. The development of cheap and accurate

synthetic methods for their production [2] have made spherical quantum dots (QDs) in particular an ideal system for the study of size-related properties [2, 145]. The effect of shape, on the other hand, has only just started to be addressed because of the technological challenges presented by the controllable and reproducible variation of the NC shape during growth which were overcome only recently [8, 14, 125, 145]. As a result, theoretical and experimental investigations of nanorods are still in their early stages [7, 125, 126, 138, 140, 146].

In terms of applications, semiconductor NRs have already demonstrated considerable advantages over their spherical counterparts in various fields. Compared to QDs, CdSe NRs show improved performance in photovoltaic cells due to better charge transport properties [147, 148]. Furthermore, it was observed that the use of elongated NCs allows a reduction of non-radiative carrier losses arising from Auger recombination compared to spherical NC emitting at the same wavelength [127, 149]. This reduction leads to an increased optical-gain lifetime and an extended gain spectral range. Also, linearly polarised emission from elongated CdSe [136, 150] and InP [140] NCs has been reported. The latter discovery predicts a very promising future for colloidal NRs because linearly polarised emission has a wide range of applications, ranging from biological labelling [60, 61] to optoelectronic devices [44].

The unique properties of CdSe quantum rods, such as a non-monotonic change of the global Stokes shift [136, 150], the polarisation ratio [136, 150] and the radiative lifetime [150] with increasing aspect ratio are just beginning to show the important role of shape in these systems. Detailed theoretical studies of InAs NRs are, however, still not available despite extensive experimental investigations conducted recently [7, 125]. After the success of our pseudopotential study on the optical properties of spherical [88] and slightly elongated [30] InAs nanocrystals discussed in Chapter 3 and 4, respectively,

we will therefore extend here our investigation to the transformation of the electronic and optical structure from three- to quasi two-dimensional quantum confinement.

This chapter is organised as follows. In Sec. 5.2 we discuss the evolution with elongation of the electronic structure of InAs nanostructures with particular emphasis on the envelope functions of the single particle states in both valence and conduction bands. In Sec. 5.3 we present our calculated optical spectra for structures with different aspect ratios of long to short axis, which we use as a starting point to discuss the shape dependence of (i) the optical band gap, (ii) the global Stokes shift, (iii) the polarisation anisotropy and (iv) the radiative lifetime in these systems. Good agreement is found with the available experimental data. Section 5.4 summarises our results.

5.2 Electronic structure

We investigate the evolution of the electronic structure in InAs nanocrystals with a diameter of 4.0 nm and different aspect ratios (ρ), covering the length regime at the transition from spherical to wire-like structures. The single-particle levels in both conduction (CB) and valence (VB) bands are calculated for structures with aspect ratios ranging from 1.0 (spherical dots) to 4.0, containing $\sim$1200 to $\sim$7000 atoms, respectively.

Figure 5.1 shows the evolution of the carrier density distribution in both conduction and valence bands, where the single particle energy levels are labelled as e_i and h_i, respectively, with i=1, 2,..., n increasing from the VBM (h_1) to lower energy levels and from the CBM (e_1) to higher energy levels. The cross-section contours are plotted on the (001) and (010) atomic planes with their intensity increasing from blue to red.

From Fig. 5.1 it is evident that, unlike in spherical structures, in NRs there are two types of envelope functions (π-like and σ-like), depending on the symmetry of the wave

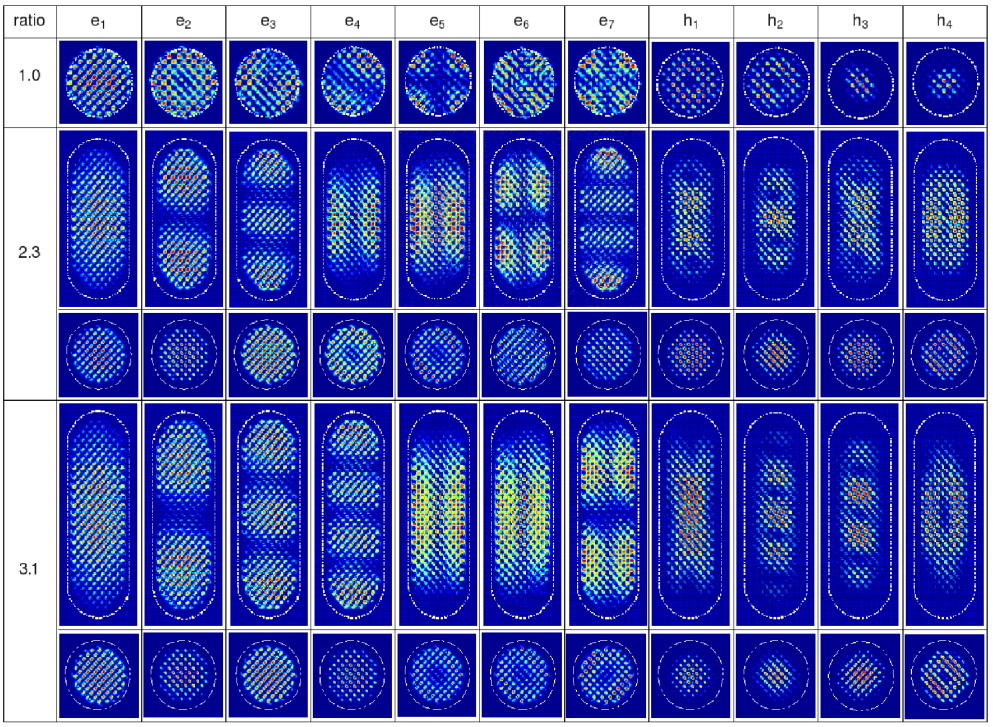

FIGURE 5.1: Envelope functions for the four uppermost (seven lowermost) states in the valence (conduction) band in InAs NCs with aspect ratios L/D=1, 2.3 and 3.1, and a diameter D = 4.0 nm. The cross-section contours are plotted on the (001) atomic plane (and also on the (010) plane for ρ=2.3 and 3.1) with the intensity increasing from blue to red. For the nanorods with the aspect ratio 2.3, the envelope functions of e_1-e_3 and e_7 are σ-type in the xy-plane and contain 0-3 nodes along the z-axis, while the envelope functions of e_4-e_6 are π-type with 0-1 node. The envelope functions in the valence band h_1-h_3 are σ-type containing 1, 2 and 0 nodes, respectively, whereas h_4 is π-type. When the nanorod length is increased and the ratio changes from 2.3 to 3.1, energy crossings occur in both conduction and valence bands. (see text)

functions in the xy-plane. A π-like wave function is symmetrical with respect to rotations about the elongated direction whereas a σ-like envelope function is symmetrical on a plane perpendicular to the rod length. Figure 5.1 shows, however, that, as in the case of spherical NCs, the character of the VB states in elongated structures displays some degree of mixing (especially evident when compared to the purer nature of the states in the CB), due to the close proximity in energy of the different levels and the large spin-orbit coupling. States with the same symmetry are further characterised according to the number of nodes along a given direction (see also Fig. 5.2). In NRs with ratio 2.3,

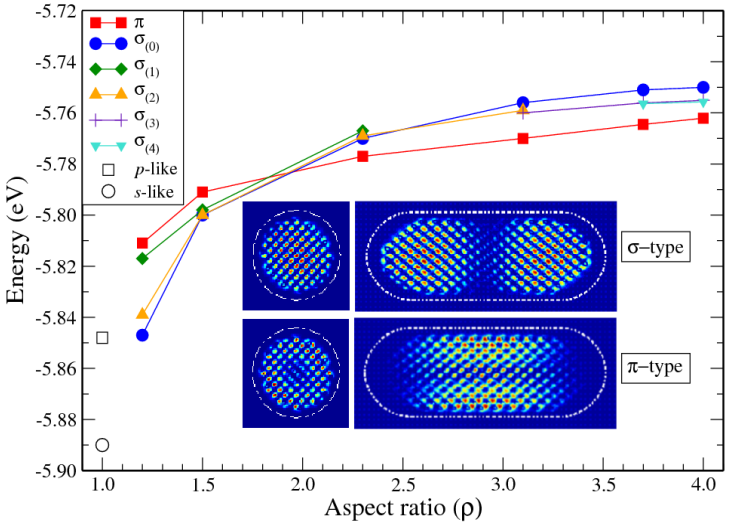

FIGURE 5.2: The evolution of the energy levels of the highest occupied molecular orbitals versus aspect ratio for 4.0-nm-diameter quantum rods. The solid lines are a guide to the eye. Black empty symbols indicate the energies of the *p*- (square) and *s*-like (circle) uppermost VB states in a spherical dot. Red squares denote π-type levels whereas levels with $\sigma_{(i)}$-type envelope function in the *xy*-plane are denoted by solid blue circles, green diamonds, orange triangles, purple crosses and cyan triangles for $i = 0, \ldots, 4$ respectively. The subscript i denotes the number of nodes along the growth direction. The inset shows σ-type and π-type envelope functions along the *xy* and *xz* planes with the white dashed line marking the boundary of the quantum rod. The VBM energy levels cross at a ratio $1.5 < \rho < 2.3$.

for example, the envelope functions of e_1-e_3 and e_7 are of type σ in the (001) plane and contain 0-3 nodes along the [001] direction, whereas the envelope functions of e_4-e_6 have π symmetry and contain 0 and 1 node along the [001] direction. The envelope functions in the valence band h_1-h_3 are σ-type containing 1, 2 and 0 nodes, respectively, whereas h_4 is π-type. As the aspect ratio increases, crossings of π and σ states occur in both the valence and conduction bands. In particular, the VBM symmetry changes from π to σ at a ratio $1.5 < \rho < 2.3$, as shown in more detail in Fig. 5.2. It is also important to notice that the VBM is σ-type with 1 node for $\rho = 2.3$, and σ-type with 0 nodes at a ratio of 3.1 (see also Fig. 5.2). These features will have important consequences for the optical properties of NRs discussed in the following sections.

Figure 5.2 illustrates in greater detail the evolution of the energy levels in the VB as

a function of the aspect ratio (levels with the same symmetry are connected with solid lines). The energies of the electronic states decrease with increasing length due to the quantum confinement effect. As elongation only reduces confinement along one direction (the z-axis), it has a greater effect on those levels more sensitive to confinement in that direction. This leads to level crossings as some energy levels depend on length much more than others.

The level crossing between the two highest VB levels is particularly important because generally it is the relaxation of the electron from the CBM to the VBM that is associated with photoluminescence (PL). This level crossing is therefore also closely related to the mechanism behind the evolution of the Stokes shift (i.e., the energy separation between emission and absorption), which is commonly observed in semiconductor quantum dots and is one of the most important quantities that determine the optical properties of NCs. Figure 5.2 clearly shows that this crossing occurs between the aspect ratios of 1.5 and 2.3 for 4.0 nm wide quantum rods. For rods with $\rho \geq 2.3$, the highest molecular orbital has σ symmetry and for $\rho > 2.5$ the wave function has zero nodes along the [001] direction; therefore, it is expected that the lowest emission transition and the optical properties in general will change once the value of the rod aspect ratio exceeds that at the crossing point (this aspect will be discussed further in Sec. 5.3). This level crossing is found to occur for aspect ratios in the range $1.2 \leq \rho_c \leq 1.5$ in rods with a diameter of 2.8 nm (not shown). We therefore conclude that in InAs the value of the aspect ratio ρ_c at which the VBM level crossing occurs is size-dependent. This is in sharp contrast with the cases of both InP and CdSe, where, respectively, no crossing [140] and a (quasi-)size-independent ρ_c [136, 151] were found.

5.3 Optical properties

5.3.1 Optical gap

Figure 5.3 shows the effect of elongation on the optical gap: the positions of the first absorption peak calculated as a function of length for NCs with $D = 4.0$ nm (red triangles) are compared with the experimental data by Steiner *et al.* [7] (dark blue triangles), and Kan *et al.* [8] (orange triangles), measured at 300K in structures with diameters ranging between 3.5 and 4.1 nm and lengths up to 23 nm. The agreement between predicted and observed increase of the peak red-shift with NR length is excellent. We should mention, however, that, due to the large memory required for the calculation of the Coulomb integrals for the larger ratios, only 10 states in the valence band and 4 in the conduction band were included in our many-body calculations (note that the pseudopotential calculations reported in ref. [136, 152] only included a total of 8 states from the conduction and 4 from the valence band for structures with $D \geq 3.0$ nm). The inaccuracy introduced by the use of such a reduced set of VB states was estimated to be less than 3.4% for the case of a spherical NC by comparing the value reported in Fig. 5.3 with that calculated using 40 holes and 4 electrons [88]. This decrease of the band gap with increasing rod length is a signature of the gradual decrease of confinement along the long NC axis. Such a strong dependence on length was, however, not observed in CdSe NRs [153]. In fact, the Bohr radius of InAs (34 nm), is much larger than the longest quantum rod considered here (16 nm), which was not the case for CdSe [153], where the Bohr radius is only 5.6 nm. As a consequence strong quantum confinement should hold in all three dimensions for the quantum rods displayed in Fig. 5.3, whereas in the case of CdSe [153] the rod lengths were in the medium to weak confinement regime. It is worth noticing that strong confinement governs the physical properties associated with the radial dimension in both InAs and CdSe quantum rods.

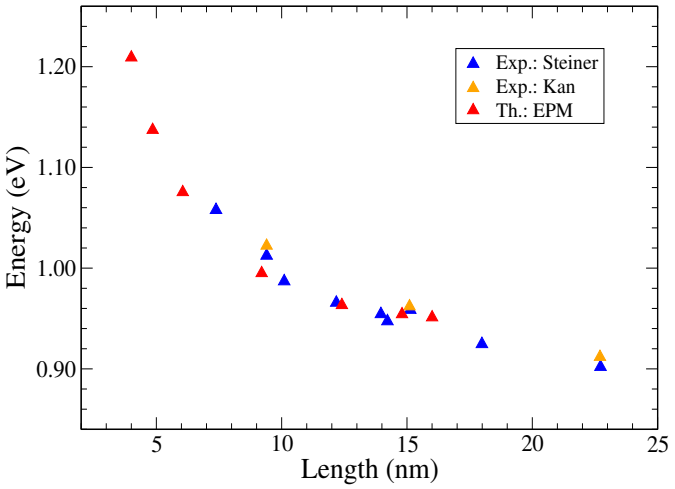

FIGURE 5.3: Optical band gap (first absorption peak) of InAs NRs as a function of the rod length: the gaps calculated for rods with $D = 4.0$ nm (red triangles) are compared with the experimental data from Steiner *et al.* [7] (blue triangles) and Kan *et al.* [8] (orange triangles), relative to rods with diameters between 3.5 and 4.1 nm.

Figure 5.4 shows the dependence on the length of the effective bandgap, defined as the increase in the energy of the first excitonic transition in a NC compared to the bulk bandgap ($\Delta E_g = E_g^{\mathrm{QD/QR/QWR}} - E_g^{\mathrm{bulk}}$, where E_g^{bulk}=0.354eV [155]), in InAs quantum dots, rods and wires. The upper (Dots) and lower (Wires) solid curves are least-squares fits to experimental [2, 9] and theoretical [154] values, respectively, relative to 0- and 1-dimensional structures. They mark the boundaries of the QR zone (gray area) allowing a theoretical determination of the transition length at which QRs are expected to exhibit the confinement behaviour of quantum wires. Our calculated values (red triangles) fall within the QR zone, extending from the upper boundary, for the shorter QRs, to the lower limits, where the ΔE_g values relative to our longer rods are very close to both the QWR curve and the experimental data of Kan et al. [8].

This demonstrates a gradual evolution from three-dimensional (3D) confinement (QDs) to a weaker two-dimensional (2D) confinement (QWRs) and seems to suggest that the longest QRs considered in this study are close to achieve the 2D-like confinement typical of QWRs. Surprisingly their length (∼16 nm) is considerably shorter than expected

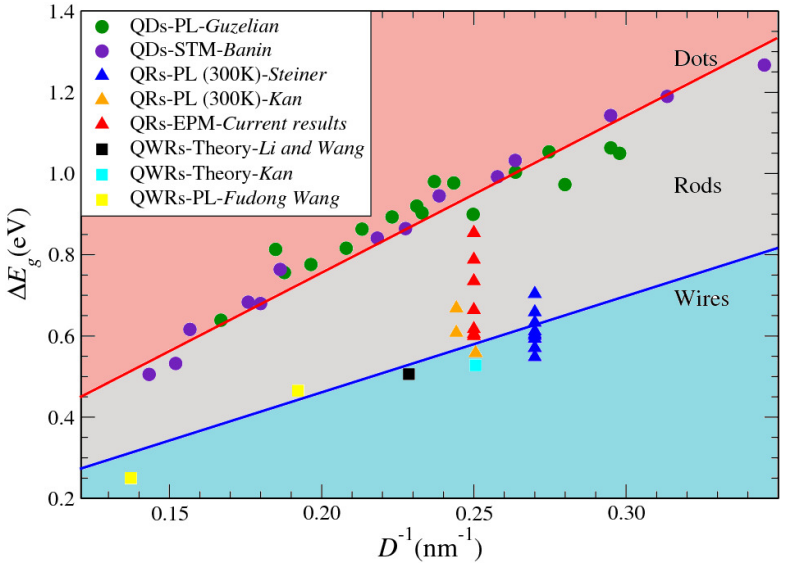

FIGURE 5.4: Effective bandgap ΔE_g versus the inverse diameter D^{-1} plotted for different InAs low dimensional structures: spherical quantum dots (dark green [9] and purple [2] circles display experimental data), NRs (orange [8] and blue [7] triangles are relative to experiment, whereas red triangles display the results of the present work), and quantum wires (black [154] and light cyan [8] squares represent theoretical results whereas yellow squares [155] display experimental data). The upper (lower) solid curve is a least-squares fit to the experimental (theoretical) values relative to quantum dots [2, 9] (quantum wires [154]). The fitting curves are digitally extracted from Ref. [155] and the fitting equations for quantum dots (red curve) and quantum wires (blue curve) are respectively ΔE_g=3.23$D^{-0.88}$ and ΔE_g=2.38$D^{-1.02}$. Although the lower curve was fitted with four theoretical data in the original work [154], only one point appears in the present diameter range. The ∼4 nm diameter QRs (orange triangles) and 3.7 nm diameter QRs (blue triangles) were taken from Ref. [8] and Ref. [7], respectively (see also Fig. 5.3). The red triangles reflect the evolution of the confinement from quantum dots to quantum wires according to our results.

by comparison to the bulk exciton Bohr radius for InAs (34 nm). Unfortunately calculating the energy gap for rods with lengths comparable with the bulk Bohr radius (corresponding to ρ=8.5 for structures with D = 4.0 nm) is highly impractical due to the prohibitively large number of atoms involved. To gain further insight into this aspect, and try to define more clearly the QR-QWR transition length in InAs, we calculated instead the evolution of other optical properties with increasing length for the same rod sizes shown in Fig. 5.4.

5.3.2 Stokes shift

The effect of elongation on the optical properties of InAs NCs is further illustrated in Fig. 5.5, where we compare the optical absorption and emission spectra calculated for NCs of different aspect ratios with experiment [8]. Despite a slight shift, that we attribute to the 15% and 20% size-distribution reported [8], respectively, for diameters and lengths in the experimental samples, there is good agreement between theory and experiment.

From Fig. 5.5 we can see that one effect of deconfinement is to bring the emission of long QRs into the technologically relevant telecommunication range (1.2-1.5μm). Another

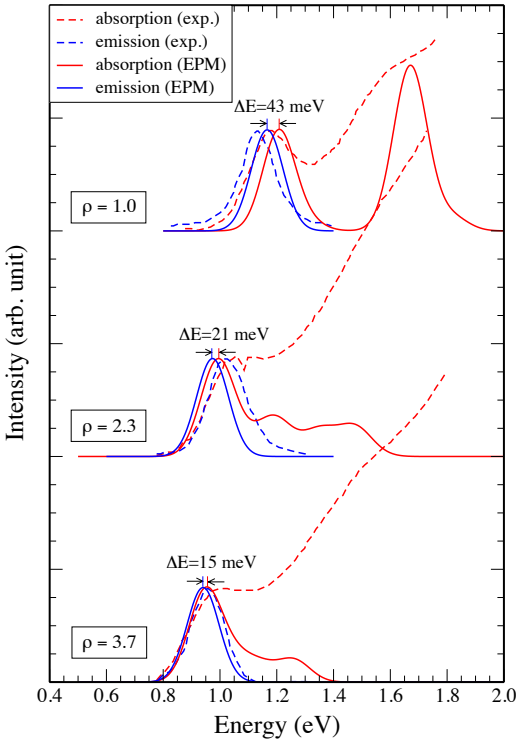

FIGURE 5.5: Absorption (red lines) and emission (blue lines) spectra of InAs NC with different aspect ratios: comparison between our theoretical results calculated for NCs with $D = 4.0$ nm (solid lines) and the experimental spectra (dashed lines) relative to samples with $D \simeq 4.0$ nm (digitally extracted from Ref. [8]). The theoretical PL intensities were normalised for clarity of presentation. A linewidth Γ=80 meV is used in all our spectra. The Stokes shift ΔE calculated for each structure is also shown.

consequence of elongation is the progressive reduction of the red-shift between absorption and emission (Stokes shift), which in Fig. 5.5 decreases from values of $43 - 50$ meV for spherical structures ($\rho = 1.0$) with D=4.0 nm, to about 15 meV for $\rho = 3.7$. A large Stokes shift of ∼50 meV was also recently observed by Schaller *et al.* [49] in 4.3-nm-diameter InAs core-only and InAs/CdSe core/shell spherical NCs.

According to our calculations, however, in elongated structures the position of the absorption peaks and therefore the size of the red shifts displayed in Fig. 5.5 is considerably affected by the magnitude of the experimental broadening (∼ 80 meV in Fig. 5.5). Indeed the Stokes shifts we obtain for the larger aspect ratios using a linewidth of 10 meV are one to two orders of magnitude smaller, reducing to ∼ 0 for the longest structure considered. The proximity of the two lowest-energy transitions, whose separation decreases with increasing rod length, due to the increase in the VB density of states [88], causes the absorption maximum to blue-shift for broadenings larger than the peak separation (thin solid lines). This leads to *apparent* Stokes shifts that are much larger than the separation between the lowermost excitonic states responsible for absorption and emission, which we call the *real* Stokes shift (henceforth referred to simply as Stokes shift, black line in Fig. 5.6).

A more detailed account of the length-dependent splitting between the band edge absorption and emission in InAs nanostructures calculated using broadenings of 80, 10 and 0 meV is presented in Fig. 5.6, where the upper x axis displays the number of atoms corresponding to the different aspect ratios, and the geometries relative to the NCs considered in Fig. 5.5 are also illustrated. The longest rod that we consider (ρ=4.0) has a long axis length $L = 16$ nm and contains ∼7000 atoms. As one can see from Fig. 5.6, the shifts calculated with $\Gamma = 80$ and 10 meV are close for small elongations, but deviate

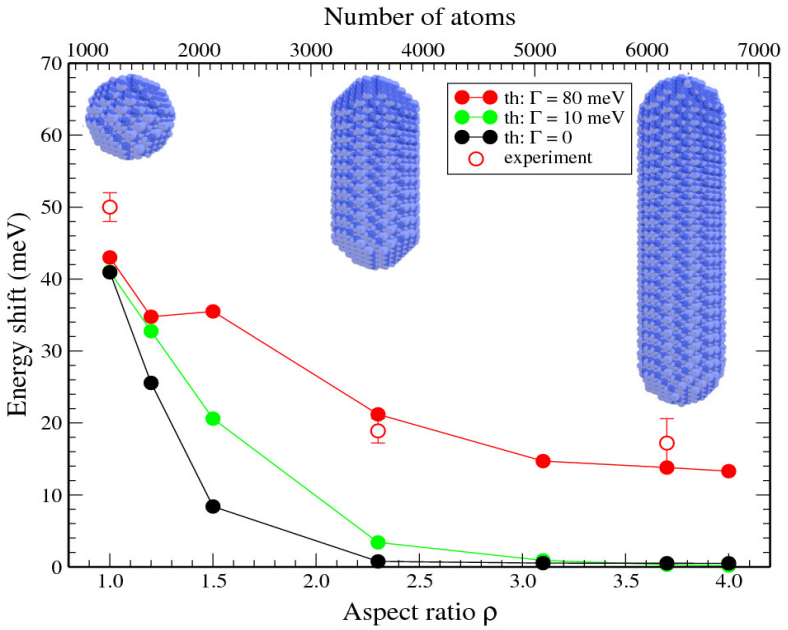

FIGURE 5.6: Calculated *real* (black solid line) and *apparent* (red and green solid lines) Stokes shift as a function of elongation in InAs nanocrystals with $D = 4.0$ nm, compared with experimental data from Kan *et al.* [8] (also shown in Fig. 5.5). The Stokes shift is defined as the difference in energy between the positions of the first absorption and emission peaks coming from the red. The nanocrystal atomistic geometries shown correspond to ρ=1.0, 2.3 and 4.0. The upper x-axis displays the number of atoms relative to each value of ρ.

substantially from each other as soon as the density of excitonic states near the absorption transition increases (at $\rho = 1.5$), with the shift for $\Gamma = 80$ meV converging to larger values. Similarly to the $\Gamma = 10$-meV-shift, the (*real*) Stokes shift ($\Gamma = 0$) decreases rapidly when the aspect ratio increases from 1.0 to 2.3, reaching a plateau where the shift reduces to ~ 500 μeV for $\rho = 4.0$. This is in sharp contrast with the case of CdSe quantum rods where the Stokes shift was found to exhibit a non-monotonic behaviour [136].

Although several investigations of the underlying mechanisms have been reported in the literature [42, 134, 156], the origin of the Stokes shift in InAs nanostructures is still unclear. Here, we suggest that its possible origins include (i) *excitonic exchange*

splitting and (ii) *orbitally forbidden valence states*. Our previous pseudopotential calculations [88] showed that in spherical NCs the lowest exciton manifold originates from the single particle states $h_{1,2}$ (VBM) and e_1 (CBM) (with a total degeneracy of 4×2=8, see Fig. 5.7d). We previously found that in *spherical* NCs the envelope function of the lowest electron state has s-like symmetry, while that of the highest hole state (VBM) has prevalently p-like symmetry (see Fig. 5.7g and Fig. 5.2). Therefore, the oscillator strength of the absorption from the ground state to $(h_{1,2}, e_1)$ is very small and the transition is formally optically forbidden. The next eightfold degenerate excitonic state is $(h_{3,4}, e_1)$. The exchange interaction splits it into a higher three-fold degenerate optically allowed "bright" multiplet, a middle threefold-, and a lower twofold-degenerate "dark" multiplets, as shown in Fig. 5.7 (d). We found [88] that the lowest absorption peak corresponds therefore to the first fully optically allowed transition from the exciton ground state to $(h_{3,4}, e_1)$ (red solid arrow in Fig. 5.7d), whereas the emission occurs from the lower (partially optically forbidden) dark exciton state (blue solid arrow in Fig. 5.7d) and is both red shifted and slow. The Stokes shift is thus given by the difference between the energies of these two transitions (blue and red arrows), which we calculate to be 41 meV in InAs spherical NCs with 4.0 nm in diameter. This value is almost unaffected even for a line broadening as large as 80 meV (typical in experiments [8]), because of the large separation between the lowest energy allowed transitions, for which we obtain an *apparent* Stokes shift of 43 meV (see Fig. 5.6).

Due to the lifting of the degeneracies and the crossings of the levels taking place in the valence band, however, this picture becomes more complex in elongated structures. Figures 5.7e and 5.7f show schematically the absorption and emission transitions at low temperature in InAs NRs with the same diameter (4.0 nm) but different aspect ratios (ρ=2.3 and 3.7). Our calculations show that the lowermost exciton manifold (h_1, e_1) originates from the single-particle states h_1 (VBM) and e_1 (CBM) which, including

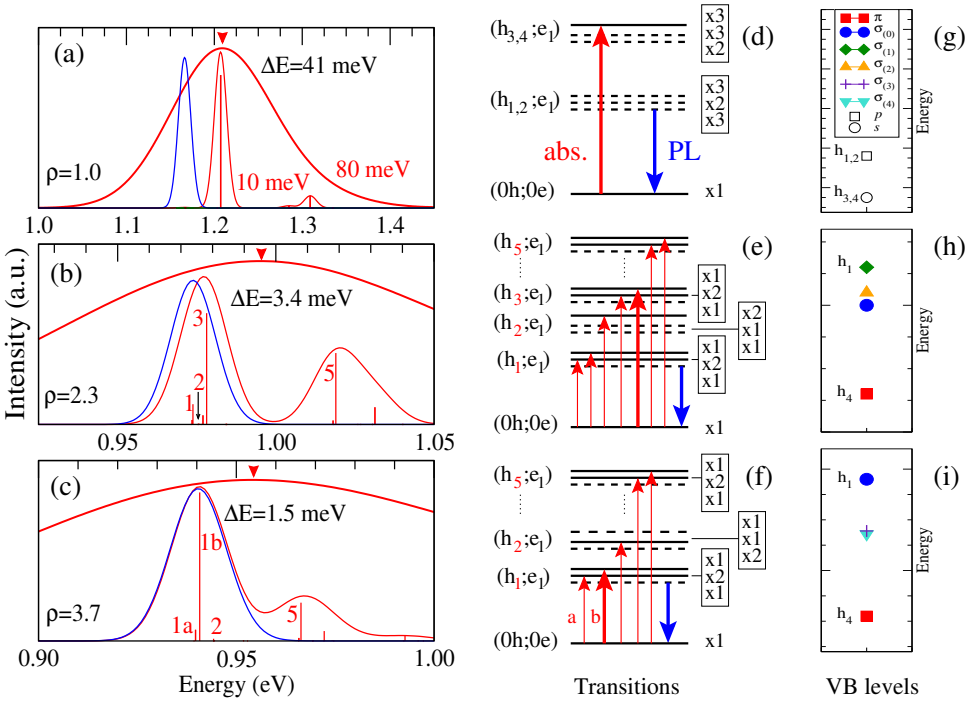

FIGURE 5.7: Effect of the line broadening on the Stokes shift: the left panels display our theoretical absorption (red lines) and emission (blue lines) spectra of InAs NC with $D = 4.0$ nm and different aspect ratios (1, panel (a); 2.3 panel (b) and 3.7, panel (c)). The absorption spectra displayed are calculated using two values (10 meV, thin lines; and 80 meV, thick lines) for the line broadening, whereas red vertical lines display the relative transition probabilities and are labelled according to the index i of the hole levels h_i involved in the transitions [marked in red in panels (e) and (f)]. The notation $(h_i,\ e_m)$ indicates that a specific exciton is derived mainly from the single-particle levels h_i and e_m. The degeneracy of the different states in a manifold is indicated by "(xn)". Solid (dashed) horizontal lines indicate bright (dark) excitons (i.e., states optically accessible from the ground state), whereas vertical arrows indicates transitions between levels. Red (blue) arrows indicate absorption (emission), whereas thick (thin) arrows indicate strong (weak) transitions. The right panels (g, h and i) are snapshots of Fig. 5.2 taken at $\rho = 1.0$, 2.3 and 3.7, and indicate the symmetry of the 4 topmost energy levels in the VB in these structures to aid the interpretation of the character (allowed/forbidden or strong/weak) of the transitions shown in the middle panels.

spin, yield $2 \times 2 = 4$ levels. This 4-fold degenerate exciton multiplet is split by exchange interaction into a higher singly-degenerate, a middle twofold-degenerate, and a lower singly-degenerate level, respectively. Above these lowest exciton states are three exciton manifolds derived from e_1 and h_2, h_3 and h_4. Due to the energy crossing in the valence band discussed in Sec. 5.2 (see Fig. 5.2), the symmetry of the different exciton states

varies, depending on elongation, and so does therefore also the character (allowed or forbidden) of the different transitions in which they are involved, as illustrated in Fig. 5.7e and 5.7f. In a NR with $\rho = 2.3$ for example, the strongest absorption transition, indicated by a thick solid red arrow in Fig. 5.7e, is from the exciton ground state to (h_3, e_1). This is due to the fact that, although h_1, h_2 and h_3 have all the same (σ-type) symmetry as e_1, h_3 has also the same number of nodes as e_1 (see Fig. 5.7h, Fig. 5.1, and Fig. 5.2). In contrast, the transitions from the ground state to (h_1, e_1) and (h_2, e_1) are weak on account of the different number of nodes along the growth direction between h_1, h_2 and e_1. It is interesting to note that for a quantum rod with aspect ratio of 3.7 and 4.0, the exciton manifold involved in both absorption and emission is the same (h_1, e_1). The Stokes shift in that case is thus the value of the exchange splitting between bright and dark states (0.506 meV and 0.494 meV for ρ=3.7 and 4.0, respectively, black symbols in Fig. 5.6). Due to the small exchange splitting, at room temperature a thermal population of the bright state occurs resulting in vanishingly small Stokes shifts. An allowed transition (weaker than the band edge one but stronger than those immediately above it) is found to take place, for all ratios, between the ground state and (h_5, e_1). The presence of this transition is responsible for the blue shift of the absorption for large inhomogeneous broadenings, which leads, in elongated structures, to large values of the *apparent* Stokes shift.

5.3.3 Degree of linear polarisation

Another key property that exhibits a distinct signature of the change in the optical properties with decreasing confinement along one direction is the PL polarisation. Figure 5.8 displays the calculated degree of polarisation as a function of NC elongation, for structures with $D = 4.0$ nm. It clearly shows that while the PL of a spherical dot is completely unpolarised, due to the symmetry of the structure, even slightly elongated

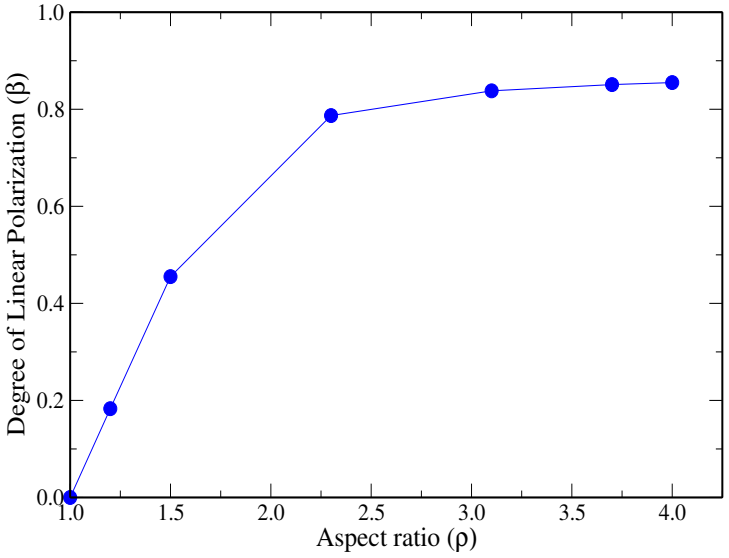

FIGURE 5.8: Degree of linear polarisation (β) as a function of NC aspect ratio, calculated at room temperature.

NCs exhibit some degree of PL polarisation along the long axis. The polarisation factor closely reproduces the behaviour of the Stokes shift (see also Fig. 5.6), exhibiting a steep change for small elongations ($1 < \rho < 2.3$), where it increases rapidly from zero to $\sim$ 80%, followed by a plateau where it remains approximately constant, converging to 85% for $\rho = 4.0$. This value is consistent with the linear polarisation predicted for an infinite InAs wire with the same diameter [112], and with the polarization anisotropy calculated [152] for and observed [136, 150] in elongated CdSe NCs. Elongated InAs nanostructures are therefore ideally suited for orientation-sensitive applications in the telecommunication range.

5.3.4 Radiative lifetime

The magnitude of the Stokes shift discussed in Sec. 5.3.2 represents a key parameter to understand another property of these structures: the lifetime of their emission.

TABLE 5.1: Comparison between experimental and theoretical radiative lifetime for InAs NCs. Our results are presented for three different values of the effective dielectric constant of the medium surrounding the NC (ϵ_{out} = 2.5[a], 4.5[b] and 6.0[c]) to account for the different materials (solvents, surfactants and semiconductor shells) used in the experiments.

	D (nm)	Lifetime (ns)		
Current calculation				
spherical dot	4.0	543.4[a]	206.0[b]	136.4[c]
slightly elongated dot (ρ=1.2)	4.0	404.0[a]	152.1[b]	100.4[c]
Experiments				
InAs/CdSe core/shell [49]	4.3		205	
InAs/CdSe/ZnSe core/shell/shell [157]	4.4		∼170-300	
InAs/CdSe/ZnSe core/shell/shell [158]	4.9		150	

In Table 5.1 we compare our results for spherical ($\rho = 1.0$) NCs with $D = 4.0$ nm with the available experimental data for spherical dots (unfortunately no lifetime data have been published so far for InAs rods). Results for slightly elongated NCs (with $\rho = 1.2$) were also included as our previous calculations [88] suggested that many "nominally" spherical experimental samples contained a large fraction of slightly elongated structures. Given that the experimental data are all relative to core/(multi-)shell structures it is perhaps not surprising that the lifetimes calculated using large values for the matrix dielectric constant ($4.5 \leq \varepsilon_{\rm out} \leq 6.0$) give the best agreement with experiment. That this is the case for both values of the aspect ratio ($\rho = 1.0$ and $\rho = 1.2$) indicates once again the difficulty to distinguish between spherical and slightly elongated structures based on spectroscopic data.

Figure 5.9 illustrates the evolution of the radiative lifetime ($\tau_{\rm R}$) calculated as a function

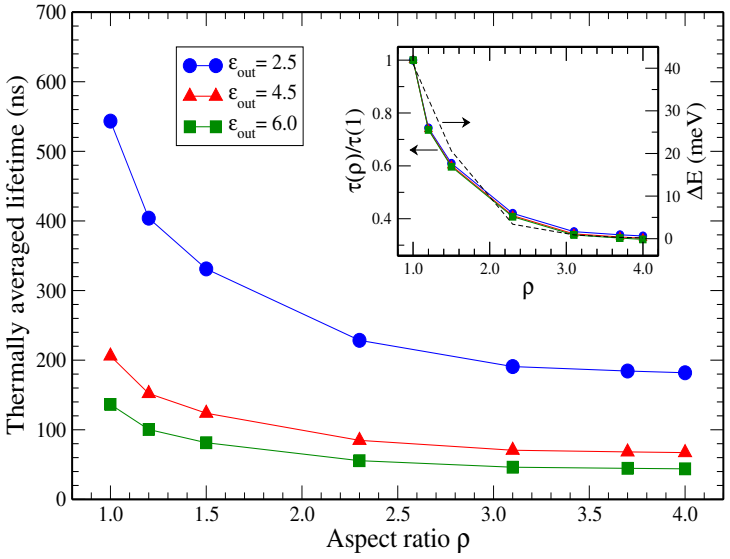

FIGURE 5.9: Thermally averaged radiative lifetime τ_R, calculated at room temperature as a function of the aspect ratio (ρ) for NCs with $D = 4.0$ nm. As in Table 5.1, the results are presented for different NC environments (i.e., different values of the effective dielectric constant ε_{out}). Inset: comparison between the curves in the main panel (left y-axis) and the energy shift from Fig. 5.6 calculated with a broadening of 10 meV (right y-axis); the lifetimes are normalised to their value in a spherical structure ($\tau(\rho = 1)$).

of NC elongation. The longer lifetime observed at room temperature in spherical structures compared to more elongated NCs is due to the larger Stokes shift between bright and dark states, in the former (see Fig. 5.6 and Fig. 5.7). After light absorption, de-excitation occurs and the exciton relaxes to its lowest energy state. Owing to the large Stokes shift, in spherical structures thermal population of the bright state is negligibly low and emission therefore takes place from the dark state with a relatively long lifetime. In the case of NRs, the energy gap between the dark and bright states decreases with length leading to an increased thermal population of the bright state, which results in faster decays. The close relationship between Stokes shift and NC lifetimes is illustrated in the inset of Fig. 5.9, where the evolution with elongation of the normalised lifetimes closely follows the energy shift curve.

A similar dependence on the aspect ratio of the thermally averaged radiative lifetime at room temperature was observed experimentally in CdSe nanorods [150]. However,

whilst in that case the radiative lifetime first decreased and subsequently increased with increasing aspect ratio with a turning point at about 10-12 nm (i.e., approximately twice the bulk Bohr radius in CdSe), our calculated results exhibit a monotonic behaviour, without a turning point. The increase in the radiative lifetime of CdSe rods was explained [150] as a property of a 1D quantum structure occurring when the rod length exceeded the Bohr exciton diameter. We propose here a different interpretation of our results, which is totally independent of the size of the Bohr radius. Wang *et al.* [150] have shown that the Stokes shifts, polarisation ratios and radiative lifetimes observed in CdSe rods as a function of the aspect ratio exhibit a common non-monotonic behaviour, with the same turning point. Such a similarity of behaviour among the different optical properties is consistent with the analysis presented above, linking the shape-dependence of these properties to that of the Stokes shift. The pseudopotential calculations performed in ref. [136] unequivocally associate the turning point of the Stokes shift with the level crossing occurring at the top of the VB in elongated structures which was found to take place essentially at the same value of the aspect ratio for all rod sizes. This size-independence of the crossing point excludes therefore any possible size dependence for the turning point of the Stokes shift (and therefore any link to the size of the Bohr radius). In our study the crossover at the top of the VB occurs for values of the aspect ratio in the lower end of the range considered, and is not accompanied by any increase in the Stokes shift. We therefore conclude that there is no reason to expect any non-monotonicity in the optical properties of InAs nanostructures even for large aspect ratios exceeding the Bohr exciton radius. The behaviour as a function of elongation of the optical properties presented in this chapter can therefore be considered as an indication that our longest rods may be close to the confinement regime of a 1D structure.

5.4 In summary

The semiempirical pseudopotential method was used to investigate the evolution with elongation of the electronic structure and optical properties of 4-nm-diameter InAs NCs with aspect ratios ranging between 1 and 4, corresponding to lateral size dimensions of up to 16 nm and containing up to ∼7000 atoms. Our results, summarised in Fig. 5.10, clearly show a common behaviour for the shape-dependence of all optical properties considered in this chapter (band gap, Stokes shift, degree of linear polarisation and radiative lifetimes) which can be traced back to the variation with aspect ratio of the

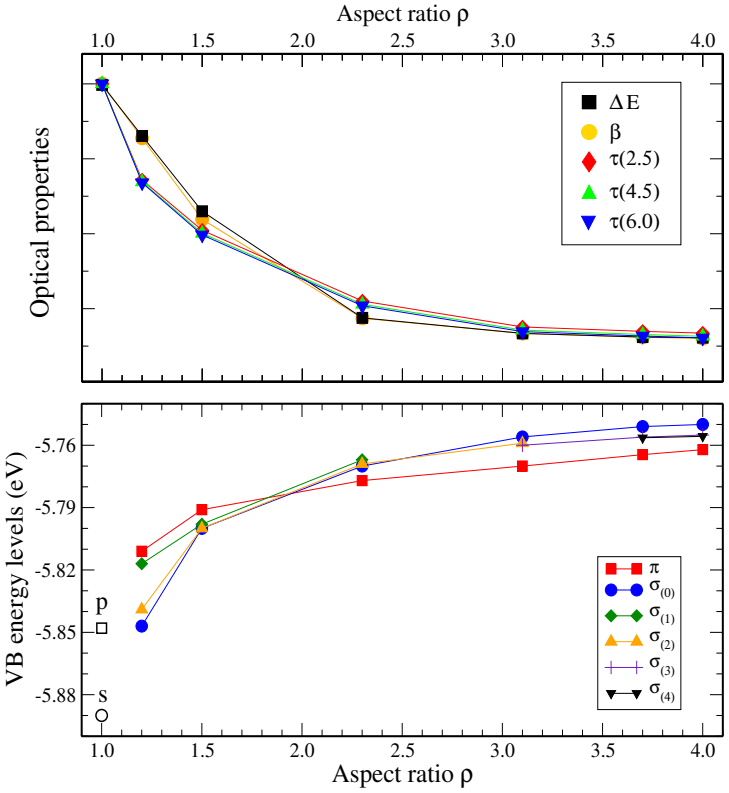

FIGURE 5.10: Summary of our results: the curves from Figs. 5.8 (with inverted y axis), 5.6 ($\Gamma = 10$ meV) and 5.9 (inset) are plotted in one graph (upper panel) directly above Fig. 5.2 (lower panel). We conclude that the evolution with elongation of all optical properties considered in this work can be traced back to the variation with aspect ratio of the electronic structure of the NC valence band. There are no labels or units on the y-axis in the upper panel as all data sets have different units and are plotted on different scales.

electronic structure of the NC valence band: a fast initial variation with increasing ρ, reflecting the crossover between π- and σ-like states at the top of the VB, is followed by a slower change accompanying a further smoother crossover between σ-like states with different (1, 2 and 0) numbers of nodes along the z direction. All curves then reach a plateau once the VBM becomes a $\sigma_{(0)}$ state, with the same symmetry as the CBM. Based on this analysis we conclude that, in contrast with the case of CdSe rods, these optical properties are not expected to show any non-monotonicity even once the excitonic Bohr radius is exceeded.

To a certain extent, our pseudopotential approach demonstrates that it can provide an accurate description of the electronic and optical properties of InAs NCs with distinct confinement systems, from three-dimensional confinement in quantum dots to quasi-two dimensional confinement in nanorods. It presents itself, in general, as a promising tool to deal with different semiconductor nanostructures. In the next chapter, we will summarise a series of our successful calculations and propose possible developments.

Chapter 6

Summary and Outlook

6.1 Concluding remarks

This thesis started out with introducing an overview of semiconductor nanocrystals. The objective of this introduction was to build a picture from their sizes to their practical realisations. In what followed, we gave an overview about physics of semiconductor NCs so as to make the contents of the thesis as self-contained as possible. The inclusion of a simple view of the physics and the associated terminologies, including quantum size effect, quantised energy spectrum, Coulomb interaction and direct carrier multiplication, was also given so that when the specific calculations or applications were discussed, the basic ideas was in context. We then gave concrete examples of the applications of semiconductor nanocrystals and the outline of this thesis in the subsequent section.

In Chapter 2, the conceptual steps required to describe the exciton states and optical properties of semiconductor NCs were explained. Basically, there were three main steps in the calculation of the optical properties in semiconductor NCs. First, three different geometries, including spherical quantum dots, slightly elongated dots and nanorods, were constructed. We then calculated the potential of the system using a superposition of screened atomic potentials. The next step was to solve the solution of the

single-particle Hamiltonian using the folded spectrum method (FSM) in which we were capable of calculating only a few eigenstates near the band gap. The final step was the calculation of the many-body effects. This task was accomplished by using the configuration interaction (CI) method. We eventually calculated many optical properties of the system.

Based on our atomistic pseudopotential approach presented in Chapter 2, we had obtained a series of success of the accurate pseudopotential study on the electronic and optical properties of spherical, slightly elongated and elongated InAs NCs. Many of the results presented in this thesis were of more general interest than the reproducibility of our calculation with the experimental features only. In what followed, additional emphasis will therefore be put into underlying the broader nature of the achievements presented.

In Chapter 3, we applied the pseudopotential method to investigate the optical properties of InAs NCs with $14.6 < R < 30$ Å. Our accurate description of the complex structure of the valence band allows us to successfully explain the low energy features observed in recent PIA measurements. Based on this result we rejected the simplistic interpretation of such features in terms of a 3-level model and suggested that the alternative hypothesis of a thermally activated surface state (as opposed to a thermal activation from a state delocalised in the dot-interior), advanced in Ref.[3], would provide a more likely explanation for the experimentally observed temperature dependence of the low-energy PIA feature. We also questioned, as previously done by Niquet *et al.* based on the results of TB calculations, the explanation of the results of STM experiments in the negative bias regime in terms of the energy separation between the two uppermost valence band levels VBM and VBM-1, suggesting instead an interpretation based on the separation between the peaks in our calculated density of states.

Our calculated interband absorption spectral features reproduced those observed experimentally, showing three strong peaks (1, 3 and 5) separated by weaker features. We achieved a good agreement for the energy position of the first 4 peaks and the seventh, down to NCs with R =14.6 Å. This result was especially remarkable considering that: (i) some of these transitions were either not predicted at all [4, 122] or were not assigned [5] in previous theoretical studies; (ii) the size range considered here includes very small NCs, i.e., a confinement regime where all other theoretical approaches break down. The agreement with the position of peaks 5 and 6 was less ideal but still reasonable. We attributed this result to a "fine structure" effect in the conduction band, where strong spin-orbit coupling induces a sizeable splitting in the otherwise 6-fold degenerate first excited state.

In Chapter 4, we calculated the effect of small elongations on the electronic and optical features of InAs colloidal dots. We found that although NCs with aspect ratios of length over diameter ≤ 1.2 showed qualitatively similar optical spectra, spherical structures can be distinguished from elongated ones based on spectral features related to the energy separation between 1S and 1P levels in the CB, such as the shape and position of the high energy peak in PIA experiments, the spacing between the first and the fifth peak observed in PLE measurements or the spacing between STM peaks measured in the positive bias regime. Based on the comparison of our results with STM, PIA and PLE data we concluded that the nominally spherical samples used in many experiments contained a significant fraction of slightly elongated particles. The substantial presence of the latter explained the poor agreement with experiment found in previous pseudopotential calculations, for the position of the peaks relative to CISL transitions in PIA spectra and for the magnitude of the E5-E1 separation in PLE spectra.

In Chapter 5, the semiempirical pseudopotential method was used to investigate the

evolution with elongation of the electronic structure and optical properties of 4-nm-diameter InAs NCs with aspect ratios ranging between 1 and 4, corresponding to lateral size dimensions of up to 16 nm and containing up to ∼7000 atoms. Our results clearly showed a common behaviour for the shape-dependence of all optical properties considered in this thesis (band gap, Stokes shift, degree of linear polarisation and radiative lifetimes) which can be traced back to the variation with aspect ratio of the electronic structure of the NC valence band: a fast initial variation with increasing ρ, reflecting the crossover between π- and σ-like states at the top of the VB, was followed by a slower change accompanying a further smoother crossover between σ-like states with different (1, 2 and 0) numbers of nodes along the z direction. All curves then reached a plateau once the VBM became a $\sigma_{(0)}$ state, with the same symmetry as the CBM. Based on this analysis we concluded that, in contrast with the case of CdSe rods, these optical properties were not expected to show any non-monotonicity even once the excitonic Bohr radius is exceeded.

In summary, our pseudopotential method provides an accurate description of the complex energy-level structure of InAs NCs and presents itself as a suitable approach to explain many experimental features and their optical properties.

6.2 Possible developments

The work presented in this thesis not only give a comprehensive theory of the electronic and optical properties of InAs semiconductor nanostructures, but also pave the way for further research directions in the view of applying it to the study of nanocrystals of selected shapes as well as different applications. Further research areas include :

- **The study of core/shell structure** Novel core/shell structures for colloidal semiconductor are made of two different semiconductor materials with different confining potentials. The concrete examples for this typical heterostructure are CdTe/CdSe, InAs/InP, CdSe/ZnSe, InAs/CdSe. The difference of confining potentials at the interface between core and shell material creates a step potential for confined carriers (electron and hole). Considering the alignment of a step potential, there are, in general, two typical topologies for the conduction- and valence-band confinement-potential alignments, as illustrated in Fig. 6.1, each of which follows by many intriguing physical properties.

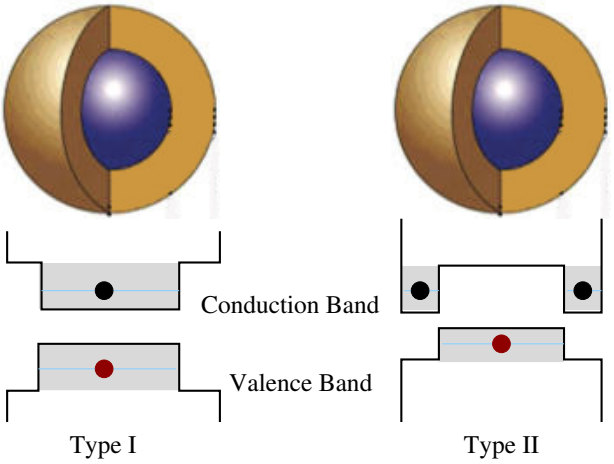

FIGURE 6.1: Cross section of core-shell nanostructures and two typical topologies for the conduction- and valence-band confinement potential alignments.

In type I core/shell structure, the extrema of both the conduction and valence band lie in the core; thus, we can achieve the localisation of the carriers in the narrow band-gap material. This, from a practical point of view, leads to the localisation of the carriers within the core region and the effect of surface traps can be therefore reduced. This is beneficial for photo-emitting and laser applications due to the enhancing of the emission efficiency. In contrast to type I, the electron and hole in type II core/shell structure are separated as a consequence of the

alignment of the conduction and valence bands extrema in the different region of the core/shell structure. The exciton lifetime of the well-separated carriers can be substantially increased because the non-radiative electron-hole recombination process is prohibited. Possible applications, from this theoretical point of view, can be developed for a building block of biological labelling, tunable lasers and photovoltaic cells. To provide guidelines for the experimental study and design of the core-shell heterostructures with desirable electronic and optical properties, a reliable tool for computing the carrier interaction needs to be developed.

- **The investigation of the potential use of single NCs and dots arrays for applications in photovoltaics** When semiconductor NCs are formed into an ordered 3-D array, minibands are formed owing to strong electronic coupling. This is a 3-D analog to a 1-D superlattice and it allows long-range electron transport. The minibands formed in an ordered array could be expected to slow the carrier cooling. Besides, they allow the transport and collection of hot carriers, thus enhancing photopotential in photovoltaic cells. In addition, the enhancement of impact ionisation is probably expected in the NC arrays leading to increased photocurrent. Nonetheless, it is emphasis that the practical realisation of this configuration is speculative and the theoretical and experimental study demonstrating actual enhanced conversion efficiencies of this system has not been fully exploited.

- **High performance single-absorbers** The engineering of high performance single-absorbers, with potential for photovoltaic application as solar cells, is another further research area. Solving the inverse problem of designing a material that optimises DCM and absorption rates in a specific energy ranges therefore yields high thermodynamic efficiency.

Appendix A

Atomic Generation

A.1 Crystal structure

The geometrical description of a crystal requires the specification of the primitive lattice vector (a_1, a_2, a_3) of the underlying Bravias lattice, as well as the specification of the atoms in the primitive cell. The content of a unit cell is described by means of an appropriate set of lattice vectors ($\mathbf{R}$), which individuates the equilibrium position of the nuclei of all the atoms in the unit cell. The aforementioned considerations can be summarised as follows :

$$\text{crystal structure} = \begin{cases} t_1, t_2, t_3, ... & \text{(primitive translation vector)} \\ \\ d_1, d_2, d_3, ... & \text{(basis of different atoms)} \end{cases}$$

The geometrical description of the crystal structure is therefore specified by the primitive vectors of the Bravias lattice and the vector forming the basis. A crystal with n atoms in the primitive unit cell is called a composite crystal. It can be described by the following

vectors :

$$R^1 = d_1 + n_1 t_1 + n_2 t_2 + n_3 t_3 + ... \tag{A.1}$$

$$R^2 = d_2 + n_1 t_1 + n_2 t_2 + n_3 t_3 + ... \tag{A.2}$$

$$R^3 = d_3 + n_1 t_1 + n_2 t_2 + n_3 t_3 + ... \tag{A.3}$$

$$R^n = d_n + n_1 t_1 + n_2 t_2 + n_3 t_3 + ... \tag{A.4}$$

A.2 InAs zinc-blende structure

InAs semiconductor has zinc-blende structure, as illustrated in Fig. A.1. It can be described as two interpenetrating face centred cubic (FCC) lattice displaced by $\frac{a}{4}(1,1,1)$ along the body of diagonal of the conventional cube. The underlying Bravias lattice is FCC having the coordination number four, i.e., each atom is surrounded by four atoms at distance $\frac{a}{4}\sqrt{3}$. a is the lattice constant (a=6.0584Å) of the material. Positions of each atom can be explained by the primitive translation vectors and the basis vectors :

$$t_1 = \frac{a}{2}(1,1,0) \tag{A.5}$$

$$t_2 = \frac{a}{2}(0,1,1) \tag{A.6}$$

$$t_3 = \frac{a}{2}(1,0,1) \tag{A.7}$$

$$d_1 = (0,0,0) \tag{A.8}$$

$$d_2 = \frac{a}{4}(1,1,1) \tag{A.9}$$

To *generate* or *span* the lattice of InAs nanocrystal, one needs to change a set of the integers n_1, n_2, n_3 in Eq. A.1 and A.2 (n=2 atoms in the primitive unit cell) until a specific radius or length is reached. To illustrate, spherical NCs can be constructed by

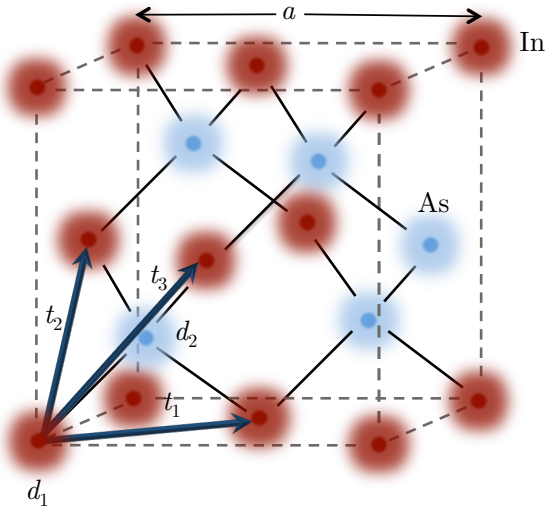

FIGURE A.1: Zinc-blende structure of InAs. The red and light blue circle represent, respectively, In and As atoms. a is the lattice constant for a material. The primitive translation vectors (t_1, t_2, t_3) are also presented with the blue arrows while d_1 and d_2 are the basis vectors of the structure.

moving n_1, n_2 and n_3 through all integral values[1] to add successive atomic layer until a specific cutoff radius r_{cut} are achieved. Similarly, elongated structures can be obtained by starting from a spherical dot with a desired diameter and subsequently insert a cylindrical segment along the growth direction. After we obtain the atomistic structure with a selected shape, some of the atoms on the NC surface need to be passivated in order to remove the surface effect. More details of surface passivation are previously given in Sec. 2.4.

[1]In the atomistic generation code, we continue with the convention that *integer* means a positive integer or zero, as well as a negative integer. When n is negative, n steps in a direction means n steps in the opposite direction. The point reached does not, of course, depend on the order in which the $n_1 + n_2 + n_3$ steps are taken.

Bibliography

[1] X. Wu, H. Liu, J. Liu, K. Haley, J. Treadway, J. Larson, N. Ge, F. Peale, and M. Bruchez, Nat. Biotechnol. **21**, 41 (2002).

[2] U. Banin, Y. Cao, D. Katz, and O. Millo, Nature **400**, 452 (1999).

[3] D. Krapf, S.-H. Kan, U. Banin, O. Millo, and A. Sa'ar, Phys. Rev. B **69**, 073301 (2004).

[4] U. Banin, C. J. Lee, A. A. Guzelian, A. V. Kadavanich, A. P. Alivisatos, W. Jaskolski, G. W. Bryant, A. L. Efros, and M. Rosen, J. Chem. Phys. **109**, 2306 (1998).

[5] S. Lee, J. Kim, L. Jonsson, and J. W. Wilkins, Phys. Rev. B **66**, 235307 (2002).

[6] U. Banin, J. Lee, A. Guzelian, A. Kadavanich, and A. Alivisatos, Superlattices Microstruct. **22**, 559 (1997).

[7] D. Steiner, D. Katz, O. Millo, A. Aharoni, S. H. Kan, T. Mokari, and U. Banin, Nano Lett. **4**, 1073 (2004).

[8] S. H. Kan, T. Mokari, E. Rothenberg, and U. Banin, Nat. Mater. **2**, 155 (2003).

[9] A. A. Guzelian, U. Banin, A. V. Kadavanich, X. Peng, and A. P. Alivisatos, Appl. Phys. Lett. **69**, 1432 (1996).

[10] Y. Yin and A. P. Alivisatos, Nature **437**, 664 (2004).

[11] A. B. Madrid, K. Hyeon-Deuk, B. F. Habenicht, and O. V. Prezhdo, ACS Nano **3**, 2487 (2009).

[12] C. B. Murray, D. J. Norris, and M. G. Bawendi, J. Am. Chem. Soc. **115**, 8706 (1993).

[13] L. Qu and X. Peng, J. Am. Chem. Soc. **124**, 2049 (2002).

[14] X. Peng, L. Manna, W. Yang, J. Wickham, E. Scher, A. Kadavanich, and A. P. Alivisatos, Nature **404**, 59 (2000).

[15] L. Manna, E. C. Scher, and A. P. Alivisatos, J. Am. Chem. Soc. **122**, 12700 (2000).

[16] M. A. Hines and P. Guyot-Sionnest, J. Phys. Chem. **100**, 468 (1996).

[17] B. C. Dabbousi, J. Rodriguez-Viejo, F. V. Mikulec, J. R. Heine, H. Mattoussi, R. Ober, K. F. Jensen, and M. G. Bawendi, J. Phys. Chem. B **101**, 9463 (1997).

[18] X. Peng, M. C. Schlamp, A. V. Kadavanich, and A. P. Alivisatos, J. Am. Chem. Soc. **119**, 7019 (1997).

[19] S. A. Ivanov, J. Nanda, A. Piryatinski, M. Achermann, L. P. Balet, I. V. Bezel, P. O. Anikeeva, S. Tretiak, and V. I. Klimov, J. Phys. Chem. B **108**, 10625 (2004).

[20] F. Schulte and H. Bross, J. Phys. C: Solid State Phys. **5**, L17 (1972).

[21] Z. Zhang, Q. Niu, and C. Shih, Phys. Review Lett. **80**, 5381 (1998).

[22] V. I. Klimov, J. Phys. Chem. B **110**, 16827 (2006).

[23] A. Ekimov, A. Efros, and A. Onushchenko, Solid State Commun. **88**, 947 (1993).

[24] A. Yoffe, Adv. Phys. **42**, 173 (1993).

[25] R. Heitz, O. Stier, I. Mukhametzhanov, A. Madhukar, and D. Bimberg, Phys. Rev. B **62**, 11017 (2000).

[26] V. I. Klimov, A. A. Mikhailovsky, D. W. McBranch, C. A. Leatherdale, and M. G. Bawendi, Science **287**, 1011 (2000).

[27] F. Wise, Acc. Chem. Res. **33**, 773 (2000).

[28] M. Kasfner, Phys. Today , 25 (1993).

[29] A. L. Efros, Sov. Phys. Sem. **16**, 772 (1982).

[30] T. Puangmali, M. Califano, and P. Harrison, J. Phys. Condens. Matter **21**, 144212 (2009).

[31] T. Puangmali, M. Califano, and P. Harrison, J. Phys. Chem. C **114**, 6901 (2010).

[32] P. Guyot-Sionnest and M. Hines, Appl. Phys. Lett. **72**, 686 (1998).

[33] V. Klimov, S. Ivanov, J. Nanda, M. Achermann, I. Bezel, J. McGuire, and A. Piryatinski, Nature **447**, 441 (2007).

[34] G. Beni and T. M. Rice, Phys. Rev. B **18**, 768 (1978).

[35] H. Shionoya, H. Saito, E. Hanamura, and O. Akimoto, Solid State Commun. **12**, 223 (1973).

[36] L. E. Brus, J. Chem. Phys. **80**, 4403 (1984).

[37] G. B. Grigoryan, A. V. Rodina, and A. L. Efros, Sov. Phys. Solid State **32**, 2037 (1990).

[38] K. I. Kang, A. D. Kepner, S. V. Gaponenko, S. W. Koch, Y. Z. Hu, and N. Peyghambarian, Phys. Rev. B **48**, 15449 (1993).

[39] V. Klimov, S. Hunsche, and H. Kurz, Phys. Rev. B **50**, 8110 (1994).

[40] M. Achermann, J. A. Hollingsworth, and V. I. Klimov, Phys. Rev. B **68**, 245302 (2003).

[41] M. Nirmal, D. J. Norris, M. Kuno, M. G. Bawendi, A. L. Efros, and M. Rosen, Phys. Rev. Lett. **75**, 3728 (1995).

[42] A. L. Efros, M. Rosen, M. Kuno, M. Nirmal, D. J. Norris, and M. Bawendi, Phys. Rev. B **54**, 4843 (1996).

[43] A. Franceschetti, H. Fu, L. W. Wang, and A. Zunger, Phys. Rev. B **60**, 1819 (1999).

[44] V. I. Klimov, A. A. Mikhailovsky, S. Xu, A. Malko, J. A. Hollingsworth, C. A. Leatherdale, H.-J. Eisler, and M. G. Bawendi, Science **290**, 314 (2000).

[45] A. A. Mikhailovsky, A. V. Malko, J. A. Hollingsworth, M. G. Bawendi, and V. I. Klimov, Appl. Phys. Lett. **80**, 2380 (2002).

[46] R. D. Schaller and V. I. Klimov, Phys. Rev. Lett. **92**, 186601 (2004).

[47] R. D. Schaller, M. A. Petruska, and V. I. Klimov, Appl. Phys. Lett. **87**, 253102 (2005).

[48] R. D. Schaller, M. Sykora, J. M. Pietryga, and V. I. Klimov, Nano Lett. **6**, 424 (2006).

[49] R. D. Schaller, J. M. Pietryga, , and V. I. Klimov, Nano Lett. **7**, 3469 (2007).

[50] V. I. Klimov, D. W. McBranch, C. A. Leatherdale, and M. G. Bawendi, Phys. Rev. B **60**, 13740 (2000).

[51] A. J. Nozik, Physica E **14**, 115 (2002).

[52] M. Califano, A. Zunger, and A. Franceschetti, Nano Letters **4**, 525 (2004).

[53] M. Califano, A. Zunger, and A. Franceschetti, Appl. Phys. Lett. **84**, 2409 (2004).

[54] V. M. Ustinov, *Quantum Dot Lasers*, Oxford University Press, USA (2003).

[55] H. Eisler, V. Sundar, M. Bawendi, M. Walsh, H. Smith, and V. Klimov, Appl. Phys. Lett. **80**, 4614 (2002).

[56] Y. Chan, J. Caruge, P. Snee, and M. Bawendi, Appl. Phys. Lett. **85**, 2460 (2004).

[57] Y. Chan, J. Steckel, P. Snee, J. Caruge, J. Hodgkiss, D. Nocera, and M. Bawendi, Appl. Phys. Lett. **86**, 073102 (2005).

[58] C. Seth, W. Wing-Keung, M. Bawendi, and B. Vladimir, Nature **420**, 800 (2002).

[59] A. P. Alivisatos, Science **271**, 933 (1996).

[60] M. Bruchez, M. Moronne, P. Gin, S. Weiss, and A. P. Alivisatos, Science **281**, 2013 (1998).

[61] W. C. W. Chan and S. Nie, Science **281**, 2016 (1998).

[62] H. Mattoussi, J. M. Mauro, E. R. Goldman, G. P. Anderson, V. C. Sundar, F. V. Mikulec, and M. G. Bawendi, J. Am. Chem. Soc. **122**, 12142 (2000).

[63] R. Mahtab, H. H. Harden, and C. J. Murphy, J. Am. Chem. Soc. **122**, 14 (2000).

[64] S. Baoquan, X. Wenzhang, Y. Guangshun, C. Depu, Z. Yuxiang, and C. Jing, J. Immunol. Methods **249**, 85 (2001).

[65] M. Han, X. Gao, J. Z. Su, and S. Nie, J. Immunol. Methods **249**, 271 (2001).

[66] M. Han, X. Gao, J. Z. Su, and S. Nie, Nat. Biotech. **19**, 472 (2001).

[67] E. Klarreich, Nature **413**, 450 (2001).

[68] P. Mitchell, Nat. Biotech. **19**, 1013 (2001).

[69] C. W. C. Warren, J. M. Dustin, G. Xiaohu, E. B. Robert, H. Mingyong, and N. Shuming, Curr. Opin. Biotechnol. **13**, 40 (2002).

[70] J. R. Petta, A. C. Johnson, J. M. Taylor, E. A. Laird, A. Yacoby, M. D. Lukin, C. M. Marcus, M. P. Hanson, and A. C. Gossard, Science **309**, 2180 (2005).

[71] D. DiVincenzo, Science **270**, 255 (1995).

[72] M. Nielsen, I. Chuang, and L. Grover, Am. J. Phys. **70**, 558 (2002).

[73] T. Fujisawa, D. Austing, Y. Tokura, Y. Hirayama, and S. Tarucha, Nature **419**, 278 (2002).

[74] J. Elzerman, R. Hanson, J. Greidanus, L. Willems van Beveren, S. De Franceschi, L. Vandersypen, S. Tarucha, and L. Kouwenhoven, Phys. Rev. B **67**, 161308 (2003).

[75] R. Hanson, B. Witkamp, L. Vandersypen, L. van Beveren, J. Elzerman, and L. Kouwenhoven, Phys. Rev. Lett. **91**, 196802 (2003).

[76] D. Loss and D. DiVincenzo, Phys. Rev. A **57**, 120 (1998).

[77] B. Kane, Nature **393**, 133 (1998).

[78] J. Sidles, J. Garbini, K. Bruland, D. Rugar, O. Zuger, S. Hoen, and C. Yannoni, Rev. Mod. Phys. **67**, 249 (1995).

[79] M. Barbic, J. Appl. Phys. **91**, 9987 (2002).

[80] H. Mamin, R. Budakian, B. Chui, and D. Rugar, Phys. Rev. Lett. **91**, 207604 (2003).

[81] R. De Sousa and S. Das Sarma, Phys. Rev. B **67**, 33301 (2003).

[82] W. Zurek, Rev. Mod. Phys. **75**, 715 (2003).

[83] J. N. Farahani, D. W. Pohl, H. Eisler, and B. Hecht, Phys. Rev. Lett. **95**, 17402 (2005).

[84] R. Scheibner, H. Buhmann, D. Reuter, M. Kiselev, and L. Molenkamp, Phys. Rev. Lett. **95**, 176602 (2005).

[85] J. H. Davies, *The Physics of Low-dimensional semiconductors*, Cambridge University Press (1998).

[86] J. Singh, *Semiconductor Devices*, Wiley (2001).

[87] J. Singh, *Electronic and Optoelectronic Properties of Semiconductor Structure*, Cambridge University Press (2003).

[88] T. Puangmali, M. Califano, and P. Harrison, Phys. Rev. B **78**, 245104 (2008).

[89] G. Bester, J. Phys. Condens. Matter **21**, 023202 (2009).

[90] S. Lee, L. Jönsson, J. W. Wilkins, G. W. Bryant, and G. Klimeck, Phys. Rev. B **63**, 195318 (2001).

[91] A. G. Peter, K. Kwiseon, B. J. Wesley, and L.-W. Wang, J. Comput. Phys. **224**, 824 (2007).

[92] D. R. Jones, C. D. Perttunen, and B. E. Stuckman, J. Optim. Theory Appl. **79**, 157 (1993).

[93] L.-W. Wang and A. Zunger, Phys. Rev. B **53**, 9579 (1996).

[94] H. Fu and A. Zunger, Phys. Rev. B **55**, 1642 (1997).

[95] D. Brust, M. L. Cohen, and J. C. Phillips, Phys. Rev. Lett. **9**, 389 (1962).

[96] D. Brust, J. C. Phillips, and F. Bassani, Phys. Rev. Lett. **9**, 94 (1962).

[97] M. L. Cohen and T. K. Bergstresser, Phys. Rev. **141**, 789 (1966).

[98] L.-W. Wang and A. Zunger, Phys. Rev. B **51**, 17398 (1995).

[99] L. X. Benedict, Phys. Rev. B **66**, 193105 (2002).

[100] P. D. J. Calcott, K. J. Nash, L. T. Canham, M. J. Kane, and D. Brumhead, J. Phys. C **5**, L91 (1993).

[101] V. Petrova Koch, T. Muschik, A. Kux, B. K. Meyer, F. Koch, and V. Lehmann, All. Phys. Lett. **61**, 943 (1992).

[102] Y. Kanemitsu, T. Futagi, T. Matsumoto, and H. Mimura, Phys. Rev. B **49**, 14732 (1994).

[103] M. G. Bawendi, W. L. Wilson, L. Rothberg, P. J. Carroll, T. M. Jedju, M. L. Steigerwald, and L. E. Brus, Phys. Rev. Lett. **65**, 1623 (1990).

[104] M. G. Bawendi, P. J. Carroll, W. L. Wilson, and L. E. Brus, J. Chem. Phys. **96**, 946 (1992).

[105] D. J. Norris, A. Sacra, C. B. Murray, and M. G. Bawendi, Phys. Rev. Lett. **72**, 2612 (1994).

[106] M. Nirmal, C. B. Murray, and M. G. Bawendi, Phys. Rev. B **50**, 2293 (1994).

[107] D. J. Norris and M. G. Bawendi, J. Chem. Phys. **103**, 5260 (1995).

[108] A. Hasselbarth, A. Eychmuller, and W. Weller, Chem. Phys. Lett. **203**, 271 (1993).

[109] O. I. Micic, J. Sprague, Z. Lu, and A. J. Nozik, Appl. Phys. Lett. **68**, 3150 (1996).

[110] D. O. Demchenko and L.-W. Wang, Phys. Rev. B **73**, 155326 (2006).

[111] S. Fafard, D. Leonard, J. L. Merz, and P. M. Petroff, Appl. Phys. Lett. **65**, 1388 (1994).

[112] M. Califano and A. Zunger, Phy. Rev. B **70**, 165317 (2004).

[113] J. M. An, A. Franceschetti, and A. Zunger, Nano Lett. **7**, 2129 (2007).

[114] M. Califano, A. Franceschetti, and A. Zunger, Nano Lett. **5**, 2360 (2005).

[115] M. Califano, A. Franceschetti, and A. Zunger, Phys. Rev. B **75**, 115401 (2007).

[116] U. Banin and O. Millo, Annu. Rev. Phys. Chem. **54**, 465 (2003).

[117] A. L. Efros and M. Rosen, Annu. Rev. Mater. Sci. **30**, 475 (2000).

[118] Y. H. Zhu, X. W. Zhang, and J. B. Xia, Phys. Rev. B **73**, 165326 (2006).

[119] Y. M. Niquet, C. Delerue, M. Lannoo, and G. Allan, Phys. Rev. B **64**, 113305 (2001).

[120] Y. M. Niquet, C. Delerue, G. Allan, and M. Lannoo, Phys. Rev. B **65**, 165334 (2002).

[121] A. Mizel and M. L. Cohen, Solid State Commun. **104**, 401 (1997).

[122] A. J. Williamson and A. Zunger, Phys. Rev. B **61**, 1978 (2000).

[123] G. Allan and C. Delerue, Phys. Rev. B **70**, 245321 (2004).

[124] R. Magri and A. Zunger, Phys. Rev. B **65**, 165302 (2002).

[125] S. H. Kan, A. Aharoni, T. Mokari, and U. Banin, Faraday Discuss **125**, 23 (2004).

[126] O. Millo, D. Steiner, D. Katz, A. Aharoni, S. H. Kan, T. Mokari, and U. Banin, Physica E **26**, 1 (2005).

[127] H. Htoon, J. A. Hollingsworth, R. Dickerson, and V. I. Klimov, Phys. Rev. Lett. **91**, 227401 (2003).

[128] H. Fu and A. Zunger, Phys. Rev. B **57**, R15064 (1998).

[129] F. A. Reboredo and A. Zunger, Phys. Rev. B **63**, 235314 (2001).

[130] V. A. S. Singh and L. Kumar, Am. J. Phys. **74**, 412 (2006).

[131] D. J. BenDaniel and C. B. Duke, Phys. Rev. **152**, 683 (1966).

[132] A. Franceschetti and A. Zunger, Phys. Rev. B **62**, 2614 (2000).

[133] C. B. Murray, Ph.D. Thesis, Chemistry Dept., MIT, Cambridge MA , 933 (1995).

[134] H. Fu and A. Zunger, Phys. Rev. B **56**, 1496 (1997).

[135] J. M. An, A. Franceschetti, and A. Zunger, Phys. Rev. B **76**, 161310 (2007).

[136] J. Hu, L.-S. Li, W. Yang, L. Manna, L.-W. Wang, and A. P. Alivisatos, Science **292**, 2060 (2001).

[137] J. Li and L.-W. Wang, Nano Lett. **3**, 101 (2003).

[138] M. Califano, G. Bester, and A. Zunger, Nano Lett. **3**, 1197 (2003).

[139] Q. Zhao, P. A. Graf, W. B. Jones, A. Franceschetti, J. Li, Wang, and K. Kim, Nano Lett. **7**, 3274.

[140] J. Li and L.-W. Wang, Nano Lett. **4**, 29 (2004).

[141] A. Aharoni, T. Mokari, I. Popov, and U. Banin, J. Am. Chem. Soc. **128**, 257 (2006).

[142] X. Michalet, F. F. Pinaud, L. A. Bentolila, J. M. Tsay, S. Doose, J. J. Li, G. Sundaresan, A. M. Wu, S. S. Gambhir, and S. Weiss, Science **307**, 538 (2005).

[143] Y. K. Olsson, G. Chen, R. Rapaport, D. T. Fuchs, V. C. Sundar, J. S. Steckel, M. G. Bawendi, A. Aharoni, and U. Banin, Appl. Phys. Lett. **85**, 4469 (2004).

[144] N. Tessler, V. Medvedev, M. Kazes, S. Kan, and U. Banin, Science **295**, 1506 (2002).

[145] H. Yu, J. Li, R. A. Loomis, L.-W. Wang, and W. E. Buhro, Nat. Mater. **2**, 517 (2003).

[146] A. Shabaev and A. L. Efros, Nano Lett. **4**, 1821 (2004).

[147] W. U. Huynh, J. J. Dittmer, and A. P. Alivisatos, Science **295**, 2425 (2002).

[148] B. Sun and N. C. Greenham, Phy. Chem. Chem. Phys. **8**, 3557 (2006).

[149] H. Htoon, J. A. Hollingsworth, A. V. Malko, R. Dickerson, and V. I. Klimov, Appl. Phys. Lett. **82**, 4776 (2003).

[150] X.-Y. Wang, J.-Y. Zhang, A. Nazzal, M. Darragh, and M. Xiao, Appl. Phys. Lett. **81**, 4829 (2002).

[151] L. C. L. Y. Voon, R. Melnik, B. Lassen, and M. Willatzen, Nano Lett. **4**, 289 (2004).

[152] J. Hu, L.-W. Wang, L.-S. Li, W. Yang, and A. P. Alivisatos, J. Phys. Chem. B **106**, 2447 (2002).

[153] D. Katz, T. Wizansky, O. Millo, E. Rothenberg, T. Mokari, and U. Banin, Phys. Rev. Lett. **89**, 086801 (2002).

[154] J. Li and L.-W. Wang, Phys. Rev. B **72**, 125325 (2005).

[155] F. Wang, H. Yu, S. Jeong, J. M. Pietryga, J. A. Hollingsworth, P. C. Gibbons, and W. E. Buhro, ACS Nano **2**, 1903 (2008).

[156] A. Bagga, P. K. Chattopadhyay, and S. Ghosh, Phys. Rev. B **74**, 035341 (2006).

[157] J. J. H. Pijpers, E. Hendry, M. T. W. Milder, R. Fanciulli, J. Savolainen, J. L. Herek, D. Vanmaekelbergh, S. Ruhman, D. Mocatta, D. Oron, A. Aharoni, U. Banin, and M. Bonn, J. Phys. Chem. C **111**, 4146 (2007).

[158] A. Aharoni, D. Oron, U. Banin, E. Rabani, and J. Jortner, Phys. Rev. Lett. **100**, 057404 (2008).

Index